

Alkaline dissolution of aluminum: surface chemistry and subsurface interfacial phenomena

by

Saikat Adhikari

A dissertation submitted to the graduate faculty
in partial fulfillment of the requirements for the degree of
DOCTOR OF PHILOSOPHY

Major: Chemical Engineering

Program of Study Committee:
Kurt. R. Hebert, Major Professor
Andrew. C. Hillier
Monica. H. Lamm
Scott Chumbley
Pranav Shrotriya

Iowa State University

Ames, Iowa

2008

Copyright © Saikat Adhikari, 2008. All rights reserved.

UMI Number: 3316184

INFORMATION TO USERS

The quality of this reproduction is dependent upon the quality of the copy submitted. Broken or indistinct print, colored or poor quality illustrations and photographs, print bleed-through, substandard margins, and improper alignment can adversely affect reproduction.

In the unlikely event that the author did not send a complete manuscript and there are missing pages, these will be noted. Also, if unauthorized copyright material had to be removed, a note will indicate the deletion.

UMI[®]

UMI Microform 3316184
Copyright 2008 by ProQuest LLC
All rights reserved. This microform edition is protected against
unauthorized copying under Title 17, United States Code.

ProQuest LLC
789 East Eisenhower Parkway
P.O. Box 1346
Ann Arbor, MI 48106-1346

TABLE OF CONTENTS

LIST OF FIGURES	V
1. INTRODUCTION	1
1.1 Literature Review	2
<i>1.1.1 Surface chemistry of aluminum in alkaline solutions</i>	4
<i>1.1.2 Interfacial Voids in aluminum</i>	6
<i>1.1.3 Hydrogen in Aluminum</i>	9
1.2 The Present Work	12
2. EXPERIMENTAL	14
2.1 Aluminum Foils	14
2.2 Positron Annihilation Spectroscopy	15
2.3 Field Emission Scanning Electron Microscopy	16
2.4 Transmission Electron Microscopy (TEM) and Scanning Transmission Electron Microscopy (STEM)	16
2.5 Hydrogen Permeation Experiments	17
2.6 Secondary Ion Mass Spectroscopy (SIMS)	19
2.7 Atomic Force Microscopy (AFM)	20
2.8 Open Circuit Potential Measurements	21
2.9 Cyclic Voltammetry Experiments	22
2.10 Potential Step Measurements	22

3. RESULTS AND DISCUSSION	24
3.1 Interfacial void formation in aluminum by alkaline dissolution.....	24
3.1.1 <i>Positron annihilation spectroscopy studies of voids by alkaline dissolution in Aluminum</i>	<i>24</i>
3.1.2 <i>Scanning Electron microscopy observations of voids formed by alkaline dissolution in aluminum</i>	<i>30</i>
3.1.3 <i>Transmission Electron microscopy observations of voids formed by alkaline dissolution in aluminum</i>	<i>33</i>
3.2 Measurement of hydrogen chemical potential during alkaline corrosion of aluminum.....	41
3.2.1 <i>Hydrogen chemical potential measurements during alkaline corrosion of aluminum</i>	<i>41</i>
3.2.2 <i>Hydrogen permeation measurements during alkaline dissolution of Al.....</i>	<i>56</i>
3.3 Detection of hydrogen-containing species during alkaline dissolution of aluminum.....	62
3.3.1 <i>A SIMS study of aluminum dissolution in alkaline solutions</i>	<i>62</i>
3.3.2 <i>AFM study of aluminum dissolution in alkaline solutions</i>	<i>73</i>
3.3.3 <i>Implications of the SIMS and AFM observations</i>	<i>80</i>
3.4 Electrochemical behavior of anodic aluminum dissolution in alkaline solutions	87
3.4.1 <i>Cyclic voltammetry studies of aluminum dissolution in alkaline solutions</i>	<i>87</i>
3.4.2 <i>Potential-step experiments.....</i>	<i>94</i>
3.4.3 <i>Development of the mathematical models for anodic aluminum dissolution reactions.....</i>	<i>101</i>
3.5 Factors affecting the corrosion potential of aluminum in alkaline solutions.....	112
3.5.1 <i>Effect of solution composition on open circuit potential</i>	<i>112</i>
3.5.2 <i>Effect of metal properties on open circuit potential</i>	<i>119</i>
3.5.3 <i>Effect of interrupted dissolution on open circuit potential transients.....</i>	<i>123</i>
3.5.4 <i>Cyclic Voltammetry for interpretation of the corrosion potential transients.....</i>	<i>128</i>
3.5.5 <i>SIMS analysis of alkaline treated aluminum at open circuit</i>	<i>131</i>
4. CONCLUSIONS	134
5. REFERENCES	141

LIST OF TABLES

Table 2.1	Measured impurity compositions of aluminum foils	15
Table 3.1	Values of actual μ_{H} (calculated from Al side OCP) and equilibrium μ_{H} (calculated from Pd side OCP) for various pH values.	52
Table 3.2	Masses of SIMS peaks for D containing species.	62

LIST OF FIGURES

Figure 2.1	Schematic of the sample preparation procedure for FE-SEM by anodizing and chemical stripping.	16
Figure 2.2	Sample preparation for TEM by single-sided electropolishing.	17
Figure 2.3	Schematic of the double cell for hydrogen permeation measurements.	19
Figure 3.1	PAS lineshape parameter S vs. beam energy for 4N electropolished Al foils after treatment in 1 M NaOH for various times.	26
Figure 3.2	Plot of experimental W and S parameters for 4N electropolished foils treated after treatment in 1 M NaOH for various times.	28
Figure 3.3	Characteristic defect layer parameters (S_d and B_d) vs. NaOH dissolution time for 4N electropolished Al foils.	29
Figure 3.4	FE-SEM images of 4N electropolished Al foil treated in NaOH for 3 min with (a) 5 nm (45° stage tilt), (b) 5 nm (0° stage tilt), (c) 23 nm (0° stage tilt) and (d) 50 nm (0° stage tilt) metal anodized and the anodic oxide stripped chemically. SEM accelerating voltage was 15-25 keV.	32
Figure 3.5	TEM images of 4N electropolished foils treated in NaOH for 3 min. The images are of the same region with one of them slightly tilted. Accelerating voltage was 200 keV.	34
Figure 3.6	STEM image of 4N electropolished foils treated in NaOH for 3 min for the same region as shown in the TEM image of Fig. 3.5.	35

- Figure 3.7 TEM images of 4N electropolished foil treated in NaOH for 3 min. Accelerating voltage was 150 keV. **37**
- Figure 3.8 Open circuit potential on Al side (entry) and Pd side (exit) during hydrogen charging by 1M NaOH solution. **42**
- Figure 3.9 Open-circuit potential transients on hydrogen exit (Pd) side with solutions of various pH on the Al side. The top and bottom plots are the same transients plotted to different time scales. **44**
- Figure 3.10 CV scans for Pd in pH 7.0 buffer solution before charging with hydrogen from the Al side. The potentials are corrected for ohmic drop using the cell resistance $R_s = 1050 \Omega\text{cm}^2$. **45**
- Figure 3.11 CV scans for Pd in pH 7.0 buffer solution after H-charging by pH 13.5 NaOH up to an open circuit potential of -0.6 V. The NaOH solution was then removed from the Al side compartment and the CV started. The potentials are corrected for ohmic drop with the cell resistance $R_s = 1050 \text{ ohm.cm}^2$. **47**
- Figure 3.12 Open-circuit potential transients on hydrogen exit (Pd) side with solutions of various pH on the Al side. The Pd side was cathodically charged to form Pd₂H before commencement of charging from Al side. **49**
- Figure 3.13 Open circuit potential on the Pd (exit) side before and after interruption and replacement of a high pH (12.00/ 13.50) NaOH solution with a lower pH (10.00/7.00) solution on the Al entry side. **50**
- Figure 3.14 Open-circuit potential transients on hydrogen entry (Al) side during

	charging with NaOH solutions of various pH on the Al side.	54
Figure 3.15	Dissolution rates for Al foil in NaOH solutions of various pH values.	55
Figure 3.16	Permeation current for Pd electrode in pH 7.0 buffer solution at a constant anodic applied potential of 45 mV (vs. Ag/AgCl). Al side solution was 0.1M NaOH (pH 13.0) solution at open circuit.	57
Figure 3.17	Permeation current for Pd electrode in pH 7.0 buffer solution at a constant anodic applied potential of 45 mV (vs. Ag/AgCl). Al side solution was 1M NaOH (pH 13.5) solution at open circuit.	58
Figure 3.18	Calculation of diffusion coefficient for hydrogen ingress in Al during dissolution in 1 M NaOH solution. Flux is in A/cm^2 .	61
Figure 3.19	SIMS profiles after caustic dissolution of 99.99% Al for 14.5 min.	63
Figure 3.20	SIMS profiles of as-electropolished 4N Al foil.	65
Figure 3.21	D^- depth profiles after alkaline dissolution of 4N Al foil normalized with respect to bulk Al_2^- counts.	67
Figure 3.22	AID^- depth profiles after alkaline dissolution of 4N Al foil normalized with respect to bulk Al_2^- counts.	68
Figure 3.23	OD^- depth profiles after alkaline dissolution of 4N Al normalized with respect to bulk Al_2^- counts.	69
Figure 3.24	Integrated AID^- depth profiles and profile thicknesses, after alkaline	

dissolution of 4N Al samples. The profile thickness is defined as the depth at which the normalized AID^- counts are a fraction $1/e$ (i. e., 0.368) of the profile maximum. Open symbols are averages of two data points at the same time. **71**

Figure 3.25 Integrated OD^- depth profiles and profile thicknesses, after alkaline dissolution of 4N Al samples. The profile thickness is defined as the depth at which the normalized AID^- counts are a fraction $1/e$ (i. e., 0.368) of the profile maximum. Open symbols are averages of two data points at the same time. **72**

Figure 3.26 AFM images of Al surface topography after alkaline dissolution. $5 \times 5 \mu\text{m}$ top view images after 40 s, 1, 2 and 3 min dissolution, respectively. Conversion of color scale to height is indicated below each image. **75**

Figure 3.27 FE-SEM image of Al surface after 4 min alkaline dissolution (image dimensions are $2.5 \times 1.7 \mu\text{m}$). The sample was dipped in 1 M HNO_3 solution after alkaline treatment. **77**

Figure 3.28 Particle size distributions at various NaOH dissolution times, obtained by analysis of AFM images. Particle radius is defined according to $\sqrt{(Particle_Area)/\pi}$. Number of particles in each size category is referenced to an Al surface area of $25 \mu\text{m}^2$. **78**

Figure 3.29 Heights and radii of individual particles, measured by AFM after dissolution times of 5-8 min. **79**

Figure 3.30 Open circuit potential during dissolution of the 4N electropolished foil in 1 M NaOH (H_2O). **83**

- Figure 3.31 First scan cyclic voltammetric response for 4N electropolished Al foil in 0.1 M Na₂SO₄ (pH 11.75). The foil was pretreated in 1 M NaOH for 1 min prior to the CV experiment. **89**
- Figure 3.32 Effect of diffusion on current measured during cyclic voltammetric scans. **90**
- Figure 3.33 Cyclic voltammetric response at pH 11. The solid and dashed lines represent the first and second voltage cycles, respectively. **92**
- Figure 3.34 Current density measured during initial portion of first anodic sweeps in Fig. 3.33, plotted against elapsed time during the potential scan. **93**
- Figure 3.35 Example of current response to sequence of applied potential steps. The applied potential was initially held at -1.55 V for 5 min, during which a steady passive current was obtained. Then, the potential was stepped by 0.1 V in the anodic direction, at 10 ms intervals. The experiments were done in the pH 11.75 Na₂SO₄ solution. **95**
- Figure 3.36 Examples of current-potential characteristics, obtained from the sequential potential step experiments at pH 11.75. Results are shown for various applied steady-state potentials prior to the potential steps. **97**
- Figure 3.37 Examples of current-potential characteristics, obtained from the sequential potential step experiments at pH 11.00. Results are shown for various applied steady-state potentials prior to the potential steps. **98**
- Figure 3.38 Reciprocal slopes of current-potential characteristics at pH 11 and

- 11.75, plotted against the applied steady-state potential prior to potential steps. Lines are linear regressions of the data. The zero-current intercepts of the regression lines are -2.32 V (pH 11) and -1.92 V (pH 11.75). **100**
- Figure 3.39 Comparison of experimental (solid lines) and simulated (dashed lines) cyclic voltammetric responses at pH 11.75, at various scan rates. **107**
- Figure 3.40 Comparison of experimental (solid lines) and simulated (dashed lines) cyclic voltammetric responses at pH 11. First scan for various scan rates. **109**
- Figure 3.41 Comparison of experimental (solid lines) and simulated (dashed lines) cyclic voltammetric responses at pH 11. Second scan for various scan rates. **110**
- Figure 3.42 Open circuit potentials of 4 electropolished Al foils in 0.1 M Na₂SO₄ solutions adjusted to various pH values by addition of NaOH. **114**
- Figure 3.43 Minimum potential of open circuit potential transients like those in Fig. 3.42, as a function of bulk pH. **115**
- Figure 3.44 Examples of open circuit potential transients of Al foil in Al₂SO₄ - containing 1 M NaOH baths at pH 13.5. The parameter is the Al₂SO₄ concentration. **117**
- Figure 3.45 Comparison of open circuit potential transients for electropolished and as-annealed Al in 1 M NaOH. **118**
- Figure 3.46 Open circuit potential transients in 1 M NaOH for as-annealed Al foils

- containing variable bulk concentrations of copper impurity. **122**
- Figure 3.47 Potential transients of interrupted dissolution experiments. In each panel, the solid and dashed lines are the potential transients before and after the Al foil was removed from the 1 M NaOH solution, rinsed, dried, and then re-immersed. Arrows represent the potential measured at the time of the interruption. Interruption times are 20 s and 1 min. **124**
- Figure 3.48 Potential transients of interrupted dissolution experiments. In each panel, the solid and dashed lines are the potential transients before and after the Al foil was removed from the 1 M NaOH solution, rinsed, dried, and then re-immersed. Arrows represent the potential measured at the time of the interruption. Interruption times are 2 min, 5 min and 10 min. **125**
- Figure 3.49 Initial open circuit potentials of as-annealed aluminum foil in 0.1 M Na₂SO₄ solution (pH 11.00), after dissolution in 1 M NaOH solution (pH 13.50) for various times. The open circuit potential in NaOH is shown for comparison. The markers are for pH 11.00 and the curve is for pH 13.50. **127**
- Figure 3.50 Cyclic voltammetry of electropolished foils in 0.1 M Na₂SO₄ solution (pH 11.75), after dissolution in 1 M NaOH solution for various times. The scan rate was 2 mV/s. Scans were initiated at -1.8 V. **130**
- Figure 3.51 AID⁻ depth profiles measured by SIMS after dissolution of 4N electropolished aluminum foils for the indicated times in 1 M NaOD (D₂O). Normalization is with respect to the counts of Al₂⁻ in the bulk of the sample. **132**

1. INTRODUCTION

After oxygen and silicon, the most abundant element in the Earth's crust is aluminum also making it the most abundant metal in the crust. This face-centered cubic metal is light (about one third the density of steel), non-toxic, ductile, a good thermal and electrical conductor and demonstrates very high yield strengths when alloyed with copper, zinc, manganese and magnesium. Because of its combination of lightness and strength, it finds extensive usage in a lot of applications in the construction, transportation and packaging industry. It is one of the most important materials used in aircraft bodies and in the automotive industry.

Aluminum is a reactive metal but has a very good corrosion resistance since it forms a thin surface layer of aluminum oxide in air (passivation), which prevents it from further corrosion. This film is quite stable in neutral and mildly acidic solutions but dissolves more readily in the alkaline pH range. Usually, corrosion behavior of aluminum is directly related to the stability of the oxide film. Typically, the corrosion rate of aluminum increases exponentially for pH values lower than 3 or higher than about 9. For example, the uniform corrosion rate at room temperature for aluminum at pH 7.5 is about 10^{-8} g/cm²/h while the same at pH 12 is 10^{-4} g/cm²/h indicating a 4 orders of magnitude increase from the neutral to the alkaline pH range.^[1] So, neutral solutions do not attack the oxide film, except for the case of 'pitting' which occurs in the presence of aggressive anions like Cl⁻ or Br⁻ and higher temperatures but corrosion rates can be as high as 30 g/cm²/h.^[2]

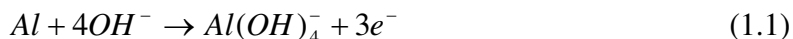
Uniform corrosion over the entire surface area of metals is the most dominant type of corrosion but it is usually easier to measure and predict making catastrophic failures

relatively rare. Corrosion forms in which there is an intense attack on localized sites while the rest of the surface corrodes much more slowly is called localized corrosion, which is much more unpredictable and hence much more difficult to measure and control. Pitting corrosion, crevice corrosion and stress corrosion cracking are the most common forms of localized corrosion depending on the type of material and environmental factors. Corrosive attack usually associated with small volumes of stagnant solutions under shielded areas (like gaskets, washers, surface deposits, insulation material etc.) or ‘crevices’ is called crevice corrosion. On the other hand, corrosive attack on the free surface of the material which leads to the formation of holes or ‘pits’ is called pitting corrosion. Various factors like high concentrations of Cl^- , poor protective coatings, acidity of solution or presence of non-uniformities in the metal structure, have been considered to lead to pitting corrosion.^[3] Stress corrosion cracking is the form of corrosion caused by the combined effect of tensile stress and a specific corrosive media. Hydrogen embrittlement, a process in which brittlement and subsequent cracking of metals is caused by ingress of atomic hydrogen into the metal, is also sometimes thought of as a type of stress corrosion cracking. Due to the detrimental effects of such corrosion processes, it is important to have a fundamental understanding of associated alkaline or acidic dissolution mechanisms.

1.1 Literature Review

In addition to being a primary corrosion process, dissolution behavior of aluminum and its alloys in alkaline solutions is of considerable interest because it is the anode reaction in aluminum-air batteries.^[4] Apart from being abundant and inexpensive, the major advantage of using aluminum as an anode material is its high voltage and energy density. Due

to its low molecular weight (26.98) and gram-equivalent weight (8.99) it can yield an electrochemical energy density of 8.04 Ah/cm³ (given by $(F \cdot \rho) / (8.99 \cdot 3600)$ where F is faraday's constant and ρ is the density of aluminum). The anodic half-reaction at the Al electrode is



which exhibits an electrode potential of -2.35 V in alkaline solutions (vs. NHE). However, the electrode potential is considerably lower than the theoretical value because of the formation of the protective oxide film on aluminum in aqueous solutions which decreases the reversible electrode potential and causes a delay for the cell to reach its maximum operating voltage. Another factor that leads to less than 100% utilization of the anode in aqueous alkaline solutions is the concomitant corrosion of aluminum with the evolution of hydrogen



Thus, the presence of the passive oxide film is undesirable here since active dissolution kinetics are required in Al-air batteries, which is the reason for using concentrated alkaline solutions in these batteries. The 'activation' here refers to changing of the passive metal surface to a chemically active state by controlling the behavior of the oxide film and reducing the rate of water reduction or hydrogen evolution. Aluminum activation is found to be induced by addition of alloying elements to the Al electrode. Small concentrations of a number of metals like indium, gallium, thallium, lead etc have been found useful in activation of aluminum.^[5, 6]

Another application of activation of aluminum is in anodic etching. Caustic dissolution used as a pretreatment prior to DC etching leads to an overall increase in the

number density of pits.^[7] Activation is also produced by cathodic half-cycles during AC etching.^[8] Such etching procedures are used in the production of aluminum electrolytic capacitors where large and controlled increase in surface area of the electrodes is desirable. A better understanding of the surface chemical and electrochemical processes accompanying activation in alkaline solutions would enhance control of corrosion and also applications where activation is desired.

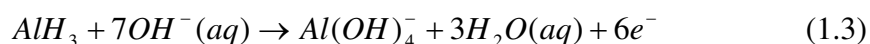
Apart from activation of the surface, dissolution of aluminum in alkaline solutions at open-circuit also leads extremely high rates of H-absorption into the metal, ^[9-14] and also formation of nanoscale voids or hydrogen bubbles ^[15, 16] near the aluminum surface. Both voids and metallic hydrogen have been considered to be mechanistically significant for environment assisted cracking. Insights gained into these processes accompanying dissolution will be beneficial in understanding the chemical mechanism of hydrogen injection during hydrogen embrittlement. Also, since near-surface voids function as sites for corrosion pits, a thorough understanding of void formation would elucidate fundamental aspects of the mechanism of pit initiation.

1.1.1 Surface chemistry of aluminum in alkaline solutions

A number of studies have been conducted on the electrochemical behavior of pure aluminum in alkaline solutions.^[17-24] The rate of the cathodic hydrogen evolution reaction was studied using impedance spectroscopy, potential scans and potential pulse techniques for measurement of the anodic dissolution of aluminum.^[19-22] Electrochemical impedance spectroscopy results of Al in concentrated KOH solutions by Macdonald *et al* and Shao *et al*

were interpreted in terms of stepwise addition of surface hydroxyl species (OH^-) until the stable aluminate ion, $\text{Al}(\text{OH})_4^-$, is formed.^[20, 24] Ellipsometry^[18] and rotating disk experiments^[17, 21] have indicated the formation of aluminum hydroxide or oxide films by dissolution. In all these studies, the primary anodic reaction was considered to be the direct oxidation of the Al metal to aluminate ions (Eqn. 1.1). As mentioned earlier, the Nernst potential for this reaction at pH 14 is -2.35 V (vs. NHE).^[1] But the measured open circuit potentials during dissolution of Al at this pH are about -1.75 V indicating a large dissolution overpotential of about 0.6 V, which is suggested to be due to the presence of a resistive surface film.^[17, 18, 21]

Another study of the dissolution of aluminum in aqueous solutions by Perrault revealed that the open circuit potential of aluminum in strongly alkaline solutions corresponds closely to the Nernst potential for oxidation of aluminum hydride to aluminate ions ^[25]



This suggests a role of surface aluminum hydride as a reaction intermediate in the dissolution process. Additional evidence for the presence of aluminum hydride was provided by Despic and co-workers.^[26, 27] They found that aluminum hydride formation was one of the major processes apart from aluminum dissolution and hydrogen evolution, during the cathodic polarization of aluminum. Titanium corrosion in alkaline solutions is also thought to proceed through a hydride mediated mechanism.^[28-30] The complexity involved with studying surface hydride species of aluminum is because of its strong tendency to oxidize which makes it difficult to detect.

Electrochemistry of processes involved during the alkaline dissolution of aluminum will be investigated in this work for gaining a fundamental understanding of the surface chemistry involved during open-circuit dissolution processes. Surface analytical and electrochemical techniques for identifying morphological changes and the potential at the metal-film interface will be one of the major focuses of this work.

1.1.2 Interfacial Voids in aluminum

A number of studies have used positron annihilation spectroscopy (PAS) for detection of nanometer-scale defects such as vacancies, vacancy clusters and voids in metals. In PAS, mono-energetic positron beams emitted from an isotopic source implant positrons to controlled depths within solid samples. The energy spectrum of gamma photons, emitted by the annihilation of these positrons with electrons in the sample, is measured and used to detect and characterize near-surface open-volume defects.

PAS investigations in aluminum have found evidence for nm-scale voids, located in the metal within tens of nm from the metal/oxide interface.^[15, 31, 32] Since these voids were found either at the surface itself or at depths up to 100 nm below the interface, these were collectively termed as “interfacial voids”. These studies indicated that the internal surface of the voids was oxide-free and if exposed at the surface, could act as reactive sites for localized corrosion. Interfacial voids result from either dissolution or oxide growth, suggesting that they form from vacancy-type defects injected by metal atom oxidation. However, the large vacancy formation energy in Al apparently prohibits room-temperature vacancy injection. The vacancy formation energy in Al has been found to be around 0.6eV^[33] which is much larger than the characteristic energy, kT , which is only 0.026eV at 300K.

In order to get a better insight into the nature and origin of these interfacial voids, the foil surfaces were also examined by Atomic Force Microscopy after NaOH dissolution and subsequent chemical stripping of the surface oxide layer. The in-situ AFM images of the surfaces after stripping revealed cavities with depths ranging from 20 to 140 nm.^[34] These PAS and AFM studies also gave substantial evidence that these cavities form from the interfacial voids by NaOH dissolution and are revealed in the AFM by the uniform dissolution of the overlying oxide layer.^[15, 34] TEM and AFM observations also revealed interfacial voids in alkaline treated aluminum after anodic oxidation of the metal. The number of voids seen by the microscopic observations of the anodic oxide was found to be proportional to the quantity of interfacial voids detected by PAS measurements for aluminum samples which were not anodized^[35] implying that these oxide voids seen in AFM and TEM observations were interfacial voids incorporated during anodizing.

Void formation mechanisms from vacancies injected by aluminum oxidation at room temperature are still not very well understood because of certain unusual aspects of these voids. First, as mentioned above, the concentration of thermal vacancies at room temperature is very low. Also, the cavities and voids detected through these methods were about $10^5 - 10^6$ times the size of aluminum metal atoms (considering Al atomic radius of 125 pm and average void radius of 50 nm). The large size of the voids indicates a surprisingly high growth rate at room temperature. If the metal vacancies are introduced by oxidation of aluminum at the metal-oxide interface and the voids grow by solid state diffusion of these vacancies, the diffusion length for the case of the moving (dissolving) interface is given by $2D/v$,^[36] where D is the diffusivity of the vacancies in Al and v is the dissolution rate of the metal.

Considering the void containing layer thickness of about 100 nm from the PAS studies and the calculated dissolution rate of about 2 nm/s in 1M NaOH from weight loss measurements,^[37] the diffusivity should be around 10^{-12} cm²/s which is reasonable for diffusion of uncomplexed vacancies at room-temperature.^[109, 110] However, the concentration of vacancies required for formation of voids of these sizes by simple monovacancy diffusion processes is enormously high. The concentration of vacancies from volume balance calculations is given by

$$C_v = R^2 / (2D_v \Omega t) \quad (1.4)$$

where R is the average void radius (assumed ~20 nm), D_v is the vacancy diffusion coefficient ($\sim 10^{-12}$ cm²/s^[109]) and Ω is the molar volume of aluminum (10.0 cm³/mol). Assuming a time of 100 s the estimated vacancy mole fraction is 2×10^{-4} while the equilibrium concentration of vacancies in aluminum extrapolated to room temperatures have been reported to be less than 10^{-8} mole fraction.^[62] Therefore, there must be other factors contributing to the thermodynamic stabilization and diffusion of vacancies in aluminum and leading to void formation. Metallic impurities like Cu have been proposed to play a role in void formation and removal by energetically stabilizing vacancies in aluminum.^[31]

In any case, direct visualization of metallic voids is necessary to provide information about size, morphology and location relative to surface features. These details cannot be conclusively obtained from indirect visualization of voids incorporated by anodizing or from PAS data. Also, since near-surface voids have been reported to function as sites for corrosion pits,^[39] these details would also be helpful in understanding their role in the mechanism of pit

initiation. Hence, direct imaging of metallic voids created by the same alkaline dissolution processes which lead to activation of the metal surface will be discussed in this work.

1.1.3 Hydrogen in Aluminum

Apart from metallic impurity elements, another possibility of the formation of voids is through the injection of hydrogen-vacancy defects in aluminum. Birnbaum *et al* have found that significant quantities (up to about 3000 at-ppm) of hydrogen can be introduced into high purity aluminum at room temperature by cathodic electrochemical charging, low energy H₂ gas plasma charging and also open-circuit caustic dissolution processes.^[40-43] Considering that the solubility of hydrogen in aluminum at 300K is just about $1-3 \times 10^{-4}$ wt-ppm,^[44, 45] this implies that the concentrations of H in aluminum introduced by these processes is about 10^7 times the equilibrium concentrations at room temperature. However, X-ray diffraction measurements revealed that either a small contraction or zero change in lattice parameter resulted even on the introduction of high hydrogen concentrations into the aluminum matrix. Since almost all FCC materials exhibit a lattice expansion when hydrogen enters the lattice interstitially, it was hypothesized that the zero change in lattice parameter was due to a formation of a H-vacancy complex at the surface which diffuses into the volume, i.e. hydrogen was associated with vacancies introduced during the treatments. Fukai *et al* have also observed superabundant vacancies due to hydrogen-vacancy interactions in a number of metals, resulting from hydrogen absorption at high pressure, as well as from room-temperature electrodeposition processes.^[46, 47] The formation of Vac-H defects in Al has also been predicted in recent theoretical calculations.^[48] Birnbaum *et al* pointed out that such large

concentrations were possible because the H-vacancy binding energy in Al (~ 0.5 eV ^[40]) compensates for the vacancy formation energy (~ 0.6 eV ^[33]). Small-angle neutron scattering and TEM revealed gas-filled voids of various sizes evidently formed by agglomeration of these defects at the surface and in the bulk aluminum.^[43] Inelastic neutron-scattering experiments showed that hydrogen resides in the bulk in the form of H₂ molecules. The bubbles of H₂ could grow by further incorporation of vacancies to reduce the strain energy. Interestingly, some of the bubbles were of the same size as the interfacial voids detected by PAS. Since the aluminum foils used and the treatment procedures are the same, there is a possibility that the absorption of hydrogen in aluminum by open circuit alkaline dissolution in the form of hydrogen-vacancy defects is correlated with the formation of interfacial voids as detected by positron methods. Insights gained into these processes and the accompanying surface chemistry would also be beneficial in understanding the chemical mechanism of hydrogen injection during hydrogen embrittlement.

Most of the work on hydrogen effects in metals during aqueous corrosion has been done using Devanathan and Stachurski's electropermeation method, i.e. using the DS cell.^[49] In the DS cell, a thin metal membrane is sandwiched between two independent electrochemical cells. Hydrogen is introduced on one side using electrolytic cathodic charging or open circuit dissolution processes. The atomic hydrogen that is absorbed into the metal diffuses through it and is oxidized on the other side (exit side). The exit side of the metal should be passive enough so that the background corrosion current is small and the current due to hydrogen ionization can be resolved. This is achieved by depositing a thin layer of palladium on the exit side which is inert, highly permeable and hence does not affect

the rate of hydrogen permeation.^[50] The DS cell has been extensively used for hydrogen permeation and diffusivity studies in metals like palladium, steel as well as high purity aluminum and aluminum alloys.^[51, 52] In principle, the electrochemical potential of the hydrogen exit side (palladium side) can also be used for determining the chemical potential of hydrogen in equilibrium with aluminum during corrosion. Using the measured chemical potential of hydrogen the thermodynamic conditions leading to hydrogen absorption and hydrogen-vacancy defect formation can be quantitatively characterized.

Secondary ion mass spectroscopy (SIMS) has also been successfully used for characterization of hydrogen absorption in aluminum by open circuit chemical charging in alkaline solutions or cathodic electrochemical charging in acidic solutions.^[53, 54] Deuterium (D) is used instead of hydrogen in these experiments (in the form of NaOD or D₂SO₄) to avoid interference with hydrogen from the ambient. Actual concentrations–depth profiles of D during the electrochemical and chemical reactions in aluminum with aqueous solutions have been obtained from SIMS. This can be helpful in correlating the formation of hydrogen interior bubbles and voids formed in aluminum from the same dissolution processes. In addition, SIMS can be used to detect surface hydride species, which may be involved in surface chemical processes during dissolution.^[25-27] SIMS has been used earlier for detection of aluminum hydride species (in the form of AlH⁺, AlH₂⁺ and AlH₃⁺) formed by exposing high purity aluminum single crystal surfaces to hydrogen.^[55-60] Such an hydride layer if present in direct contact with the metal, could facilitate formation of hydrogen vacancy defects and thus be involved in accompanying processes of hydrogen absorption and void formation.^[40]

1.2 The Present Work

Alkaline dissolution processes of aluminum lead to formation of nanoscale voids and hydrogen bubbles accompanied by absorption of large quantities of hydrogen. It has been suggested that the interfacial void formation in aluminum is more favored at specific sites rather than being random.^[32, 64] So, it is necessary to determine the exact nature and location of these “favored sites”. The first part of this work would deal with identification of voids created by alkaline dissolution of aluminum using PAS measurement. Simulations of the measurements will be conducted to reveal global characteristics of these voids. Also, instead of indirect microscopic observations of these voids using anodic oxidation of the metal, direct imaging of interfacial voids formed in aluminum during alkaline dissolution will be attempted, using TEM and STEM. Additional microscopic observations by FE-SEM will be reported, following removal of controlled depths of metal to expose subsurface voids. Information obtained from the PAS and microscopy results about depths, geometry and number densities of voids in the metal will be analyzed with respect to logistics of a void formation mechanism involving vacancy diffusion at room temperature.

The second part of the work deals with studies on hydrogen interactions with aluminum during alkaline dissolution processes using the DS cell and Al/Pd bilayer films discussed earlier. The change in the electrochemical potential on hydrogen entry and exit side will be monitored and used to calculate the chemical potential of hydrogen in equilibrium with the aluminum. The calculated H-chemical potential will be used to quantitatively characterize the thermodynamic conditions of H in aluminum and its implications for H-absorption and H-vacancy defect formation will be discussed. Permeation studies and

diffusivity measurements of H in Al will also be conducted in order to gain information about hydrogen transport behavior in aluminum.

As mentioned earlier, the same alkaline dissolution process which is accompanied by void formation and hydrogen absorption, also leads to activation of the surface. Such activation is desired in aluminum-air batteries and also as a pretreatment for etching procedures used in the manufacture of aluminum electrolytic capacitors. Hence, the surface chemical processes during the dissolution and especially the effect of hydrogen absorption is of great technological interest. SIMS will be used for studies of H-absorption during early stages of alkaline dissolution. Evidence for formation of hydride species will be sought with SIMS. AFM will be used to correlate the changes in surface features to transient changes observed by SIMS. The mechanism of anodic alkaline dissolution of aluminum will be studied using CV and potential step measurements and the results will be interpreted using models based on the proposed mechanism. The SIMS and AFM studies will be supplemented with measurements of the potential at the metal-film interface in order to determine whether it corresponds to the Nernst potential of aluminum hydride. The electrochemical behavior of aluminum in alkaline solutions will be thoroughly investigated by a review of solution and metal side factors affecting the corrosion potential of Al. The potential relevance of the surface chemistry accompanying H-absorption to interfacial void formation will be discussed.

2. EXPERIMENTAL

2.1 Aluminum Foils

The aluminum foils used in most of the work were 110 μm thick, 99.99% purity (Toyo Corp.) manufactured for use in electrolytic capacitor electrodes. The foils were provided in the as-annealed condition and had a typical grain size of 100 μm . The large grain sizes were due to an extended final annealing at a temperature greater than 500 $^{\circ}\text{C}$. These foils will be referred to as the 4N purity foils henceforth. Another set of foils were used for studying the effect of copper enrichment on the aluminum surface during dissolution. The bulk Cu concentrations in these foils were 8, 49 and 96 wt-ppm while the concentrations of all other impurities were the same. These foils will henceforth referred to as foils A1, A2, and A3 respectively. These foils again had typical grain sizes of 100 μm and were supplied in the as-annealed condition. The foils used for hydrogen permeation experiments were 25 μm thick and 99.999% purity (henceforth referred to as 5N purity foil). These foils were annealed for 52 hrs at 500 $^{\circ}\text{C}$ in vacuum. Their typical grain sizes measured using an optical microscope were again found to be around 100 μm . The bulk impurity compositions of the foils 4N, A1, A2 and A3 are listed in Table 2.1 below.

Some foils were used in the as-annealed condition while some others were electropolished. Electropolishing was carried out in a solution containing 20% perchloric acid and 80% ethanol (v/v). It was done by applying a constant potential of 30 V between the aluminum foil and a platinum counter electrode for 5 min with the electropolishing solution temperature maintained at 5 $^{\circ}\text{C}$. The potential was applied using a BK Precision D.C. power supply source (Model 1635 A). The exposed aluminum electrode area during electropolishing

was 5 cm². The platinum counter electrode was attached in a semicircular shape over the aluminum foil so as to have a uniform electric field over the electrode surface.

Table 2.1 Measured impurity compositions of aluminum foils.

	<i>Concentrations (wt-ppm)</i>			
<i>Sample</i>	<i>Cu</i>	<i>Pb</i>	<i>Si</i>	<i>Fe</i>
<i>4N</i>	55	0.58	19	13
<i>A1</i>	8	0.47	23	23
<i>A2</i>	49	0.49	24	24
<i>A3</i>	96	0.48	24	24

2.2 Positron Annihilation Spectroscopy

Doppler broadening PAS measurements were done using a slow positron beam system at the University of Missouri-Kansas City. The spectrum of gamma radiation was measured at 2000 cps with a germanium solid-state detector having an energy resolution of 1.5 keV at the annihilation photopeak energy of 511 keV. The positron source was 50 mCi ²²Na.

2.3 Field Emission Scanning Electron Microscopy

The preparation procedure for FE-SEM samples was (i) electropolishing; (ii) NaOH dissolution; (iii) anodizing in 0.1 M boric acid and 0.05 M sodium borate solution (pH ~ 8.8), at a constant applied current of 1 mA/cm^2 , until attaining voltages of 7, 31 and 69 against the counter electrode corresponding to depths of 5 nm, 23 nm, and 50 nm of metal reacted; (iv) stripping the oxide in a 5 % chromic- 20% phosphoric acid bath at $70 \text{ }^\circ\text{C}$ for 2 min (Fig. 2.1). All solutions were made using reagent grade chemicals and nanopure water.

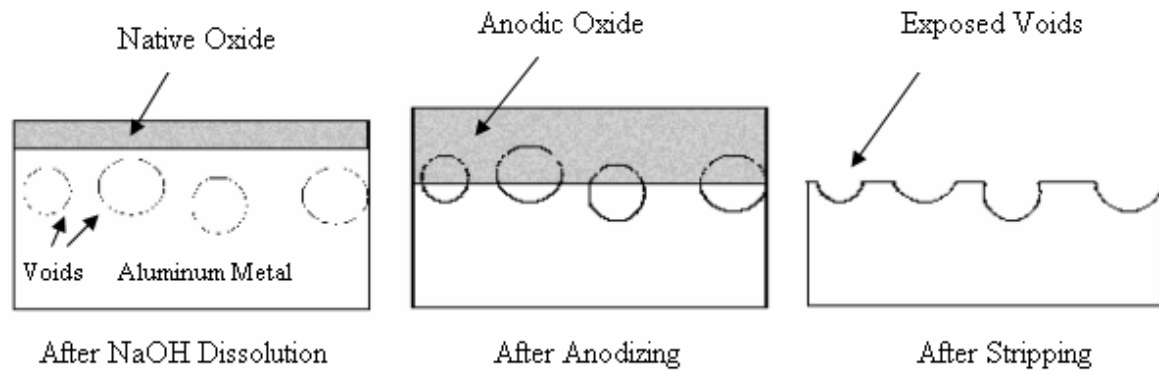


Fig. 2.1 Schematic of the sample preparation procedure for FE-SEM by anodizing and chemical stripping.

2.4 Transmission Electron Microscopy (TEM) and Scanning Transmission Electron Microscopy (STEM)

To prepare samples for transmission and scanning/transmission electron microscopy (TEM, STEM) observations, the NaOH-treated or as-electropolished samples were thinned

from the back (unreacted) side using a single-jet electropolisher, until the sample was perforated. The treated side was not exposed to the polishing solution during the thinning process (shown in Fig. 2.2 below). The electron-transparent regions close to the hole were then imaged using Philips CM30 scanning transmission electron microscope and a FEI-Tecnai G2- F20 scanning transmission electron microscope. The thickness of these regions was roughly 100 nm.

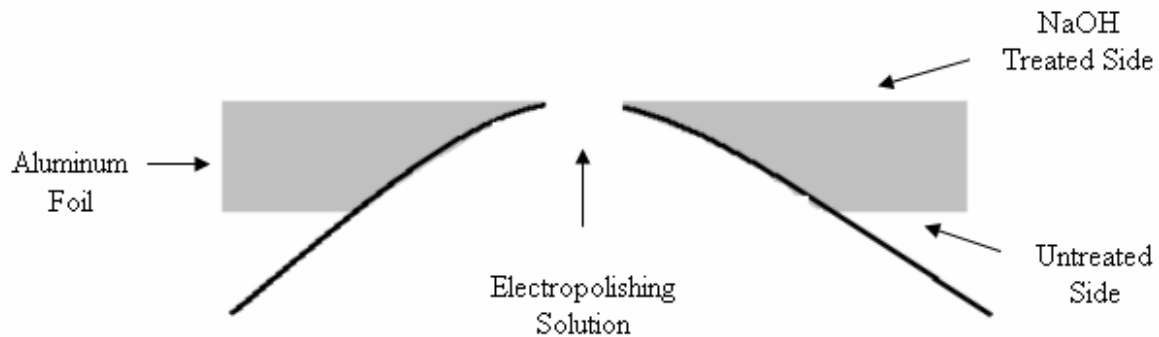


Fig 2.2 Sample preparation for TEM by single-sided electropolishing.

2.5 Hydrogen Permeation Experiments

The aluminum foils used in these experiments were 99.999% purity foils obtained from Alfa Aesar. The thickness of the foils was 25 μm (0.001 inches). The foils were annealed at 550°C for 52 hours prior to the experiments. Palladium was coated on one side of the foil using a Denton sputter coater at a current of 40 mA for 5 min. The thickness of the Pd film was found to be about 30 nm. The foil was then attached to a glass double cell as shown in below using two Viton o-rings (Fig 2.3). The solution on the Pd side in all experiments

was a standard potassium phosphate monobasic/sodium hydroxide pH 7.0 buffer solution obtained from Fisher Scientific. The Pd was electrochemically cleaned by continuous cycling between -0.5 and 1.1 V (vs. Ag/AgCl reference electrode) for 30 min until a stable voltammogram was obtained. The continuous oxidation and reduction processes in the selected potential window ensure a clean Pd surface which was necessary for obtaining reproducible measurements.^[61] After this the potential on the Pd side was held at 0.9 V for 1 min to remove residual organic contaminants and form palladium oxide. Then, the potential was held at -0.4 V for 1.5 min to reduce the oxide and form a clean palladium surface.^[61] The holding potential was then released leaving the palladium at open circuit. After letting the potential on the Pd side stabilize (~ 30 min) solutions of various pH values (controlled by adding NaOH in nanopure water) were introduced on the Al side while monitoring the potential on both sides of the foil. In some cases permeation currents on the Pd side were measured after introducing the solution on the Al side. A platinum counter electrode was used on the Pd side for these current measurements. The exit side that oxidizes the atomic hydrogen needed to be polarized anodic to the hydrogen equilibrium potential (~0.6 V vs. Ag/AgCl reference electrode at pH 7.0) so that there is sufficient anodic driving force to rapidly oxidize the atomic hydrogen without any localized attack. An anodic polarization of 45 mV (vs. Ag/AgCl) was chosen at which potential, prolonged polarization experiments and microscopic observations after that revealed absence of any localized attack.^[52] Any residual atomic hydrogen in the metal was also exhausted by the anodic polarization leading to a stable low background current after 1 hour of the polarization. Then, NaOH solution was poured into the Al side beaker continuing to measure the permeation current on the Pd side at

the applied potential. Cyclic voltammetry experiments were also conducted on the Pd side before and after H-charging from the aluminum side. In these measurements the solution on the Al side was first removed before the CV measurements.

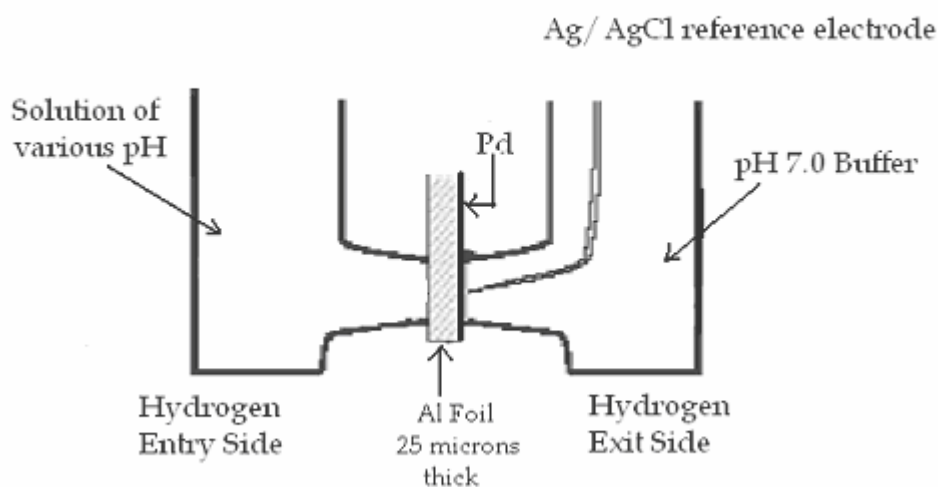


Fig. 2.3 Schematic of the double cell for hydrogen permeation measurements.

2.6 Secondary Ion Mass Spectroscopy (SIMS)

Time-of-flight Secondary Ion Mass Spectroscopy (ToF - SIMS) was done at the Center for Microanalysis of Materials, University of Illinois at Urbana-Champaign using a PHI Trift III instrument (Physical Electronics). The aluminum foils used for SIMS were all electropolished. Electropolishing was necessary to obtain a flat reference surface so that the depth of the crater after sputtering during SIMS could be measured accurately. After electropolishing, all samples were treated at open-circuit in 1M NaOD/D₂O solutions at room temperature for various times. Deuterated solutions were required to remove interference

from water vapor adsorbed from the atmosphere. The foils were then washed with de-ionized D₂O to stop the dissolution reaction in the alkaline solution, and dried using a nitrogen jet. Four samples were mounted on the sample holder at a time for the SIMS measurements. The mounting time was approximately 5 min and the time required to pump down the vacuum chamber was about 45 min. Measurement time per sample was about 30 min. Thus, the total time between alkaline treatment and measurement for the 4 samples was between 50 to 150 min. Sputtering was accomplished with a 15 kV Ga⁺ beam, and analysis of negative secondary ions used a 2 kV Cs⁺ beam. The sputtered and analyzed areas were 400 x 400 μm and 50 x 50 μm, respectively. The samples were sputtered for 5 s, and then analyzed for 8 s during depth profiling. The depth of a sputtered crater was measured to calibrate the sputtering rate in the metal using a Sloan Dektak Surface Profilometer. The sputtering rate in the metal was found to be 0.23 nm/s. The sputtering rate in the overlying oxide was not measured.

2.7 Atomic Force Microscopy (AFM)

The foils used for AFM were again electropolished 4N foils. The samples were treated in 1M NaOH (in nanopure H₂O) for various times at room temperature and open circuit before the microscopy. AFM was done in direct contact mode using a 14 μm scanner with Si cantilevers and a Si₃N₄ tip (Nanoscope III, Digital Instruments). The photodiode voltage was set to 4.60 V; assuming a cantilever spring constant of 0.06 N/m, the estimated applied force is 1.5 nN. The scan area in most cases was 5 μm by 5 μm.

2.8 Open Circuit Potential Measurements

For the open-circuit dissolution measurements, samples were mounted in a vertical glass cell having a cylindrical opening at the bottom of diameter 1.5 cm (area of 1.767 cm²). The aluminum foil was attached to this opening using 2 O-rings such only the center of the electropolished area was exposed to solution. The edge of the electropolished area was intentionally avoided since it showed indications of preferential dissolution. In some cases, the 4N, A1, A2 or A3 foils were used in the as-annealed condition for open circuit potential measurements. For most open circuit potential measurements, the solution used was 1 M NaOH made using nanopure water. The pH of this solution was found to be 13.5. For experiments investigating effects of variable pH on the open circuit potentials, a 0.1 M Na₂SO₄ solution was first made and then the pH was adjusted to the desired value using solid crystals of NaOH (to minimize alterations in the Na₂SO₄ concentration due to change of volume). For experiments investigating the effect of aluminum concentration on open circuit potential, Al₂SO₄ crystals were first added to the 1M NaOH solution so as to make the solution of the desired aluminum concentration. This generally decreased the pH of the NaOH solution slightly from its initial value of 13.5 (depending on the amount of Al₂SO₄ added). Hence the pH was again raised to 13.5 by adding adequate amount of NaOH crystals. In some interruption experiments, the solution was removed from the glass cell, the Al foil was washed and air-dried and then fresh solution of the same or different pH was poured into the cell. An Ag/AgCl reference electrode was used for the open circuit potential measurements. The temperature was 21-22 °C during all dissolution experiments.

2.9 Cyclic Voltammetry Experiments

For cyclic voltammetry (CV) experiments, the same cell setup as that in the open circuit potential measurements was used. The foils were first dissolved at open circuit for 1 min in 1 M NaOH at 21 °C. Then the solution in the cell was replaced by a 0.1 M Na₂SO₄ solution with its pH adjusted to either 11.00 or 11.75 using NaOH crystals. A Pine Instruments Bi-Potentiostat model AFRDE-5 was used to apply the electrochemical polarization. An Ag/AgCl electrode was used as the reference and a platinum wire was used as the counter electrode. In most CV experiments, the solutions were air-saturated but in some cases, the solution was de-aerated by nitrogen-sparging for 1 hour. The temperature during the CV experiments was controlled at 21 °C since the measured currents were found to be temperature-sensitive. The CV experiments were carried by first scanning the potential in the anodic direction starting from a potential close to the open circuit potential at a desired scan rate between 0.5 to 4 mV per second.

2.10 Potential Step Measurements

The potential step experiments were done to obtain information about the conduction in the surface film and the potential at the metal-film interface. The experiments were again done using the same cell setup as described earlier and the same reference and counter electrodes. In this case, the potential at the aluminum electrode was first held at a constant potential above the open circuit potential for a period of 5 min in order to obtain a steady state passive current density. After that, a series of anodic steps of 0.1 V were applied at intervals of 10 ms. For the analysis of some of the CV and the potential step experimental

data, it was required to calculate the cell ohmic resistance. This was done by anodically etching aluminum foils in 1 M HCl solution, in the same cell.^[65] The etching current density had been shown to be controlled by the cell ohmic resistance. The cell resistance during etching was multiplied by the ratio of the conductivity of 0.1 M Na₂SO₄ to that of 1 M HCl, to obtain the cell resistance applicable to both experiments. The resistance was found to be 300 Ω-cm².

3. RESULTS AND DISCUSSION

3.1 Interfacial void formation in aluminum by alkaline dissolution

This section reports TEM, STEM and FE-SEM observations of voids in aluminum created by dissolution in 1M NaOH solutions. The microscopy results are compared to PAS measurements on samples subject to the same surface preparation. The information from PAS and microscopy are complementary, in that PAS reveals global characteristics of the void population, while microscopy yields details of the geometry and location of voids.

3.1.1 Positron annihilation spectroscopy studies of voids by alkaline dissolution in Aluminum

PAS data are analyzed in terms of 2 line shape parameters called the S- parameter and the W-parameter. Annihilations by valence and core electrons contribute to the S and W parameters, respectively. Since valence electrons populate open volume defects such as vacancies or voids, these defects have higher S and lower W parameters. A typical PAS S-parameter vs. beam energy (~ implantation depth) is shown in Fig. 3.1 for electropolished Al foils treated for three representative NaOH treatment times. All S-values were normalized against the bulk S-value, representing a defect-free reference. The top scale represents the mean implantation depths of the positrons, which is controlled by the beam energy.^[66]

$$z_m = 14.8E_b^{1.6} \quad (3.1)$$

S-values greater than one in the metal indicate annihilation events occurring at open volume defects like vacancies and nm-scale voids. Fig. 3.1 clearly shows a region of depths up to ~100 nm with the values of $S > 1$, indicating the presence of open volume defects. The oxide

layer is the region of a few nm thickness with characteristic S values less than 1.^[67] The solid lines are predictions of simulation by a defect layer model to be discussed below. Similar defect containing regions were indicated by S-energy profiles for several sodium hydroxide treatment times between 0-30 min.

A W-parameter vs. S-parameter plot for 4N electropolished foils dissolved for different times, is shown in Fig. 3.2 below. S and W values for all the experiments fall along two straight-line segments connecting 3 vertices. The vertices identify states with characteristic S and W values, which can be phases such as the metal, oxide or particular kinds of defects. The leftmost point (lowest S values) represents annihilation within the oxide layer, and the rightmost points (highest S values) correspond to annihilation in the defect-containing layer. The points then move along the lower straight line from right to left with the vertices corresponding to the defect layer and the aluminum bulk. The S and W parameters for the defect layer (rightmost vertex) as seen from the plot are 1.045 and 0.95, respectively. The S-W plot indicates that there was only one defect type present in all the samples.^[68] The S values obtained here are higher than the value of 1.027 for vacancies in aluminum^[33] suggesting that the defects in the samples studied are larger than vacancies. The S values for the defect state in Fig. 3.2 is close to values of ~1.06 found earlier by Hebert *et al* for metallic voids of nm scale or larger.^[15, 31] The difference in the S values is due to the lower energy resolution of the detector used in the current work. Also, the high S values for the defect layer as compared to the S values for the oxide layer (0.94) suggests that the defect layer voids are oxide free, or have at most a monolayer thick oxide film, which does not trap

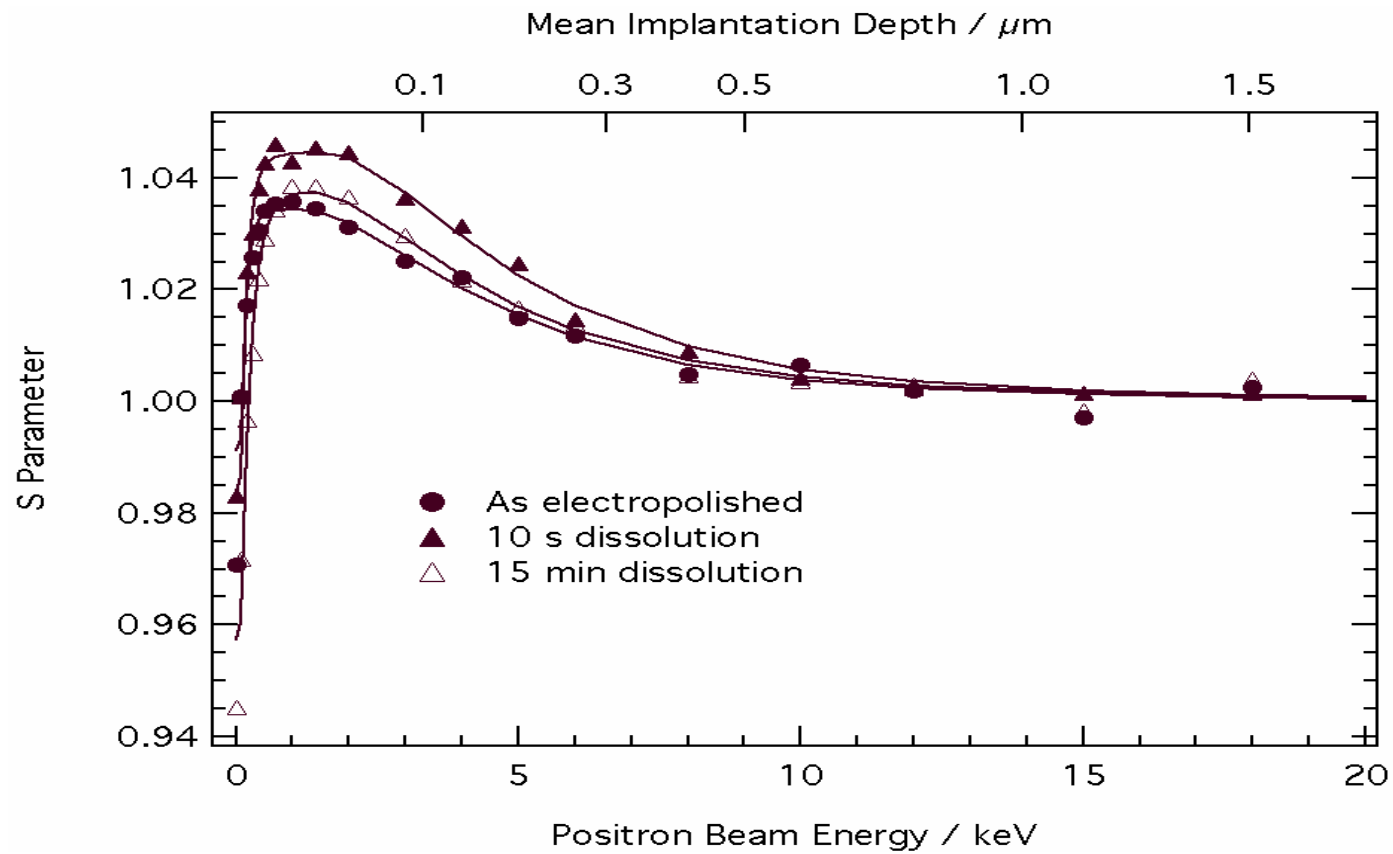


Fig. 3.1 PAS lineshape parameter S vs. beam energy for 4N electropolished Al foils after treatment in 1 M NaOH for various times.

positrons effectively.^[38] Thus, we conclude that the defect state in Fig. 3.2 corresponds to voids of at least 1 nm in size whose inner surfaces are free of oxide. Such subsurface metallic voids have also been revealed by PAS in as-annealed aluminum before and after NaOH treatment^[15], anodic oxidation^[32] or acid dissolution.^[64]

Quantitative analysis of the spatial distribution of defects was done by fitting the S profiles to a solution of the diffusion-annihilation equation for positrons in a solid, using the software application VEPFIT. The simulation assumed a uniform void-containing layer adjacent to the oxide-metal interface. It yielded fit values of the characteristic S-parameter (S_d) and thickness (B_d) of the defect layer. Fit values of defect layer parameters for various dissolution times in NaOH for the 4N electropolished foil are shown in Fig. 3.3 below. The value of S_d is semi-quantitatively related to defect type and volume fraction by

$$S_d \approx f_d S_D + (1 - f_d) S_B \quad (3.2)$$

where S_D is the characteristic S parameter of voids, $S_B = 1.0$, the S parameter of aluminum crystal, and f_D is the void volume fraction in the defect layer. Since Fig. 3.2 shows that voids are the only defect, the variations of S_d in Fig. 3.3 reflects changes in the void volume fraction. Thus, the void volume fraction seems to have a maximum value around 2-4 min of NaOH dissolution time, and then decayed slowly. The defect layer thickness was around 60 nm in most cases, with some scatter.

All the PAS studies indicated the presence of a void layer in the metal beneath the oxide-metal interface within 50-100 nm from the interface. Indirect and direct imaging of voids was then attempted to confirm their presence, and to reveal their geometry and location. Since the maximum S_d value was seen to be at about 3 min NaOH dissolution time,

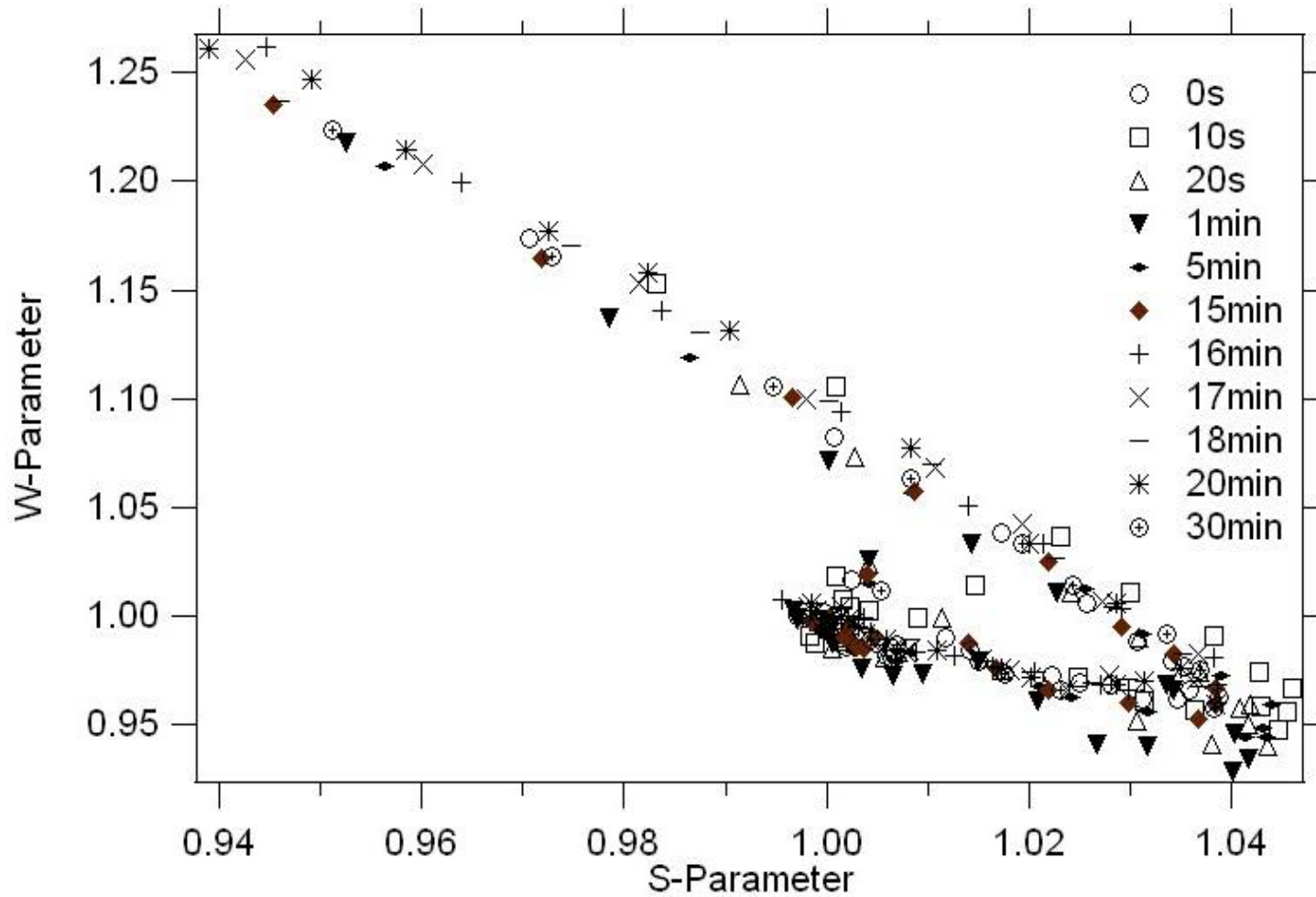


Fig. 3.2 Plot of experimental W and S parameters for 4N electropolished foils treated after treatment in 1 M NaOH for various times

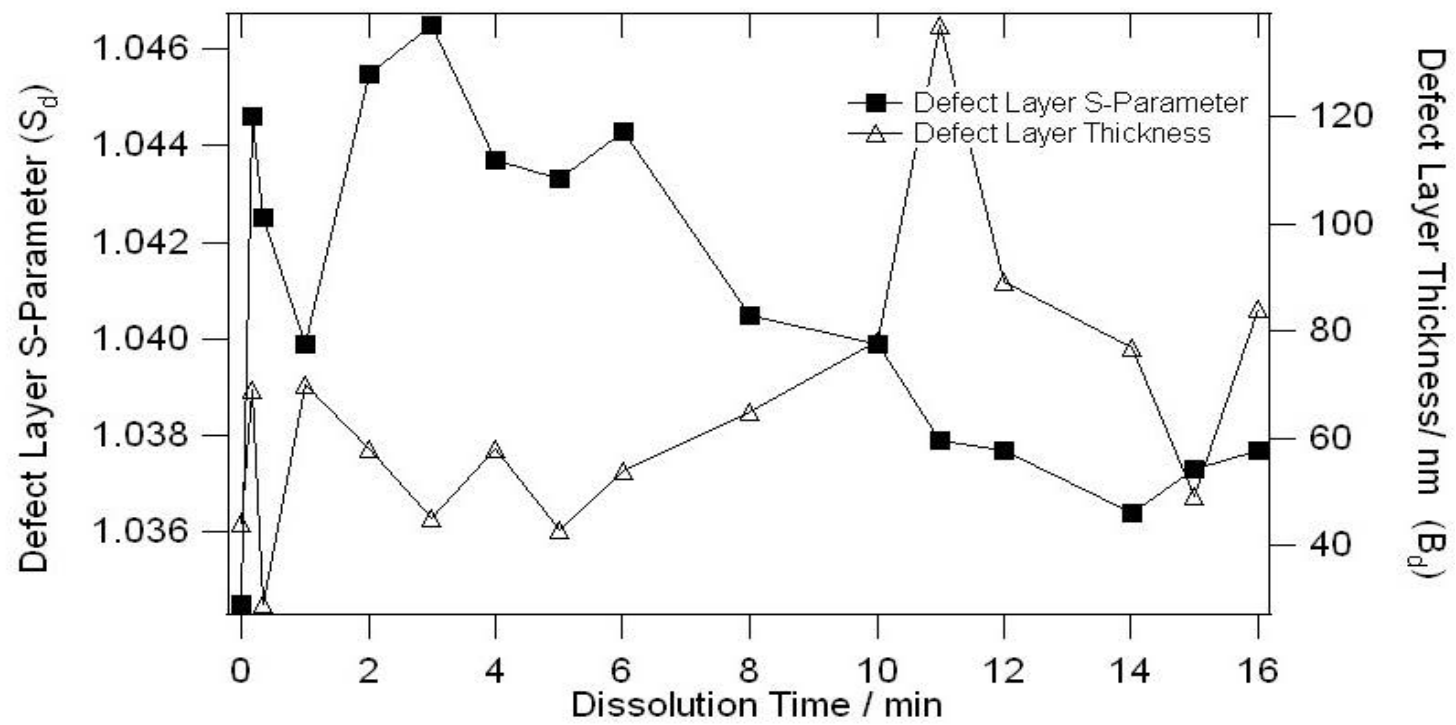


Fig. 3.3 Characteristic defect layer parameters (S_d and B_d) vs. NaOH dissolution time for 4N electropolished Al foils.

this dissolution time was chosen for most microscopic investigations using FE-SEM, TEM or STEM.

3.1.2 Scanning Electron microscopy observations of voids formed by alkaline dissolution in aluminum

Electropolished aluminum foils treated in NaOH for 3 min were anodized in a borate buffer solution at constant current density of 1 mA/cm^2 , until the voltage vs. the platinum counter electrode corresponding to a desired metal dissolution depth was reached. The transport number of Al^{3+} ions in the anodic oxide film has been found to be 0.4.^[107] Thus, 40% of the film is formed at the film-solution interface and 60% at the metal-film interface by oxidation of the metal. Assuming a 100% current efficiency for oxide growth and using the forming voltage-thickness ratio of 1.2 nm/V ,^[108] the oxidized depth of the void-containing defect-layer was calculated from the measured voltage during anodizing. The overlying anodic oxide was then stripped in a chromic-phosphoric acid solution. This treatment dissolves the oxide and then forms a nm-thick Cr containing film which suppresses further dissolution. Fig. 3.4 below shows FE-SEM images of a foil in which the metal was anodized up to depths of (a, b) 5 nm, (c) 23 nm, and (d) 50 nm respectively after the NaOH treatment. A large number of circular cavities, most of which around 20 nm in size can be clearly seen in the images (a) and (b), for which the sample was oxidized up to a depth of 5 nm. The number density of these cavities is on the order of 10^9 cm^{-2} . These cavities were not seen in samples that were treated in NaOH for the same duration of time but not oxidized. Fig. 3.4 also clearly shows that the number density of cavities decreases significantly when

the oxidized metal depth is increased to 23 and 50 nm. This indicates that the objects producing the cavities are found in a metal layer of less than 20 nm thickness from the oxide-metal interface. This depth is roughly similar to the estimated void-containing defect layer thickness of 60 nm obtained from the PAS simulation results. Thus, the cavities could be voids in the metal, exposed at the surface by oxidation followed by oxide removal. From the micrographs, it appears that the cavities are preferentially found near ridges created by the alkaline dissolution treatment, although a few are also located in the scalloped depressions between ridges.

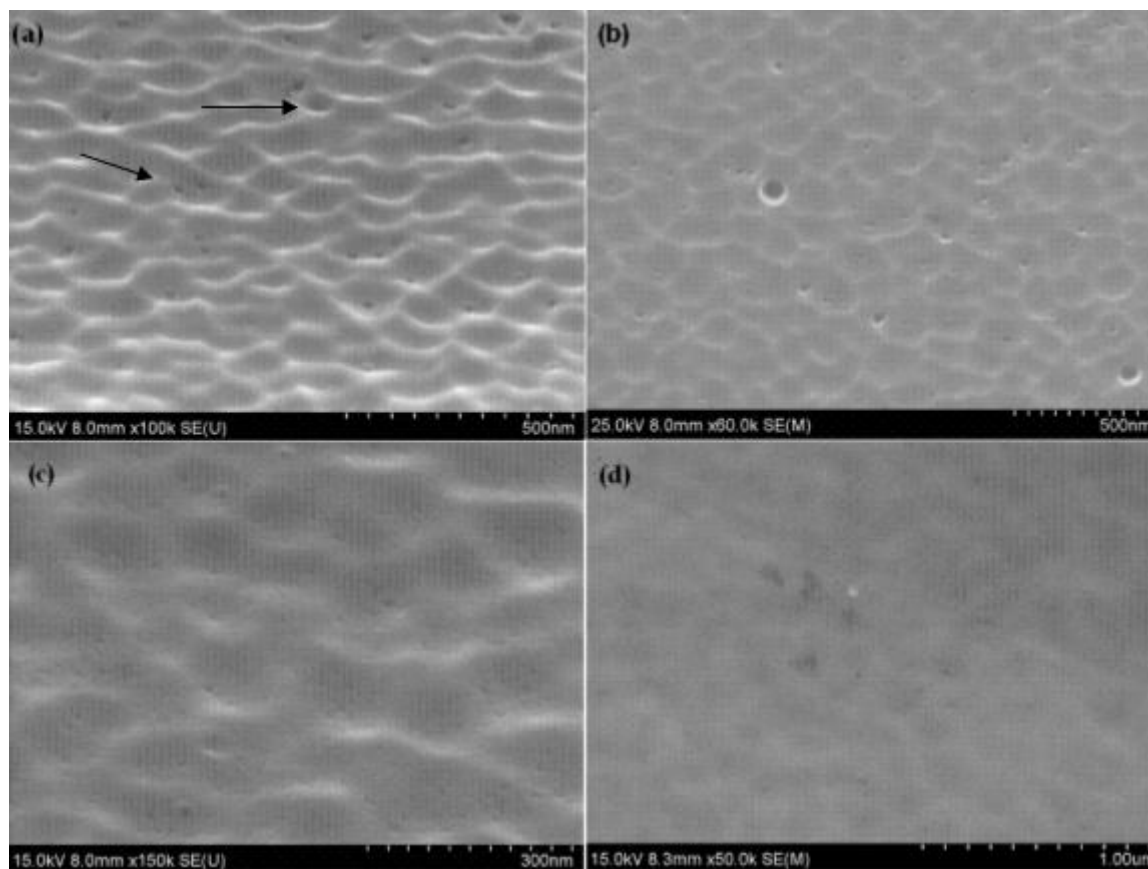


Fig. 3.4 FE-SEM images of 4N electropolished Al foil treated in NaOH for 3 min with (a) 5 nm (45° stage tilt), (b) 5 nm (0° stage tilt), (c) 23 nm (0° stage tilt) and (d) 50 nm (0° stage tilt) metal anodized and the anodic oxide stripped chemically. SEM accelerating voltage was 15-25 keV.

3.1.3 Transmission Electron microscopy observations of voids formed by alkaline dissolution in aluminum

TEM imaging of the same 3 min alkaline treated electropolished foils was done after thinning the samples from the back (unreacted) side, protecting the defect layer formed during the NaOH dissolution process. Fig. 3.5 below shows TEM micrographs of the same region on a sample before and after tilting the sample slightly. The sample reveals the presence of small circular features 10-20 nm in size. Tilting of the sample about the Bragg diffraction condition revealed changes in contrast consistent with what is expected for small voids ^[69], i. e. the objects changed from light to dark. Tilting in this manner is equivalent to obtaining "through focus" images, the method commonly used to identify voids. The response of the voids to tilt was substantially different from the contrast exhibited by nearby dislocations, which could be made to become invisible while the voids were always visible. White arrow marks in Fig. 3.5 point to voids and black arrow marks point to dislocations.

The same region in Fig. 3.5 which was imaged in the conventional TEM mode, was also imaged in the STEM mode, wherein a strong objective lens is used to de-magnify the electron beam to a narrow spot, which is then scanned over a the sample in a two-dimensional raster. STEM provides the flexibility of operating the instrument at relatively low magnifications and hence, larger instantaneous field of view. Also, since in the case of STEM, the area of the specimen actually being scanned is exposed to the electron beam, it reduces the chances of the damage to the sample by electron beam irradiation. Fig. 3.6 shows a STEM image of the same general region imaged by TEM as shown in Fig. 3.5, for the

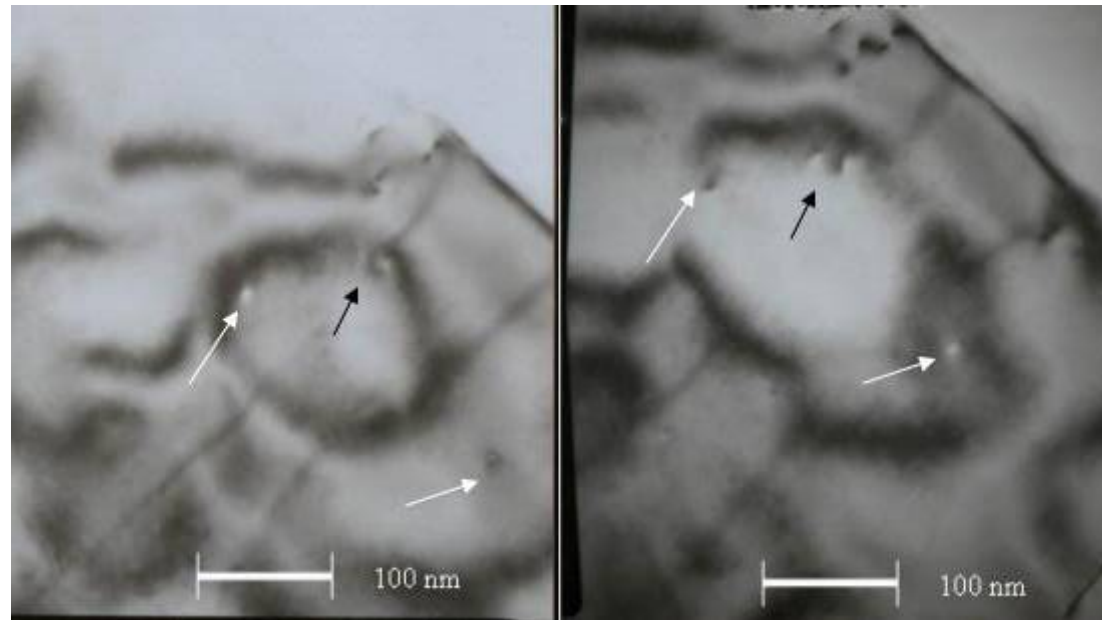


Fig. 3.5 TEM images of 4N electropolished foils treated in NaOH for 3 min. The images are of the same region with one of them slightly tilted. Accelerating voltage was 200 keV.

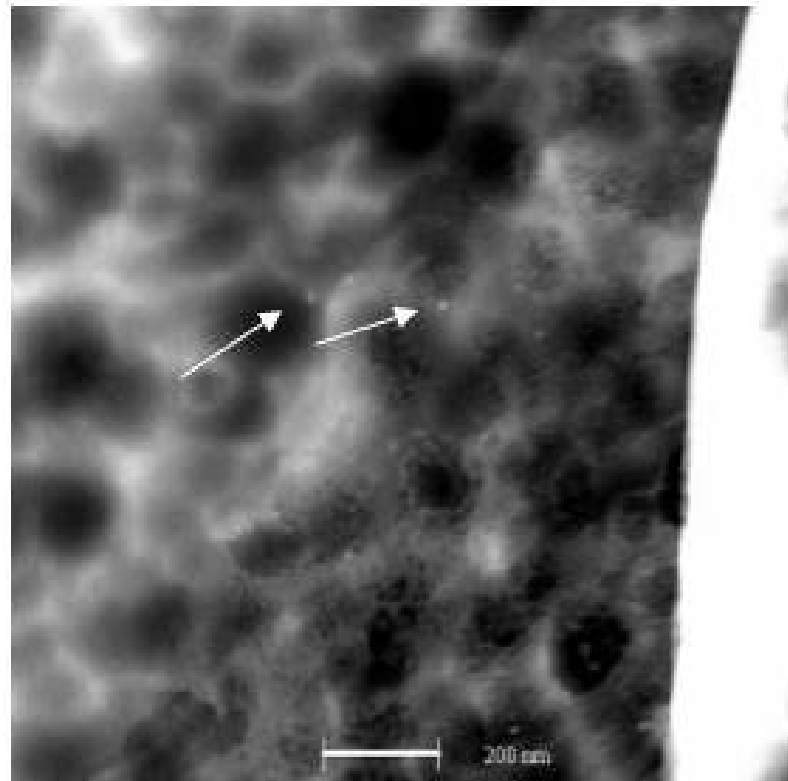


Fig. 3.6 STEM image of 4N electropolished foils treated in NaOH for 3 min for the same region as shown in the TEM image of Fig. 3.5.

3 min NaOH treated sample. It again indicates the presence of similarly sized features at these locations. The greater field of view reveals a higher number of such features than the TEM images. The scalloped surface of the samples apparent in the SEM images is also seen clearly in the STEM image.

Since the PAS studies indicated an S-parameter of more than one even for the as-electropolished samples, some voids are also expected to be seen in TEM images for these samples. While a few features like those seen for the treated samples were discovered in the untreated sample, the number observed (as determined from about 20 micrographs), was at least ten times smaller than that in the treated samples (as determined from around 40 micrographs with a total imaged area of about $25 \mu\text{m}^2$). The order of magnitude of the void number density was estimated at 10^8 cm^{-2} for the treated sample. These values corroborate the PAS observation that the void number density, indicated by the defect layer S-parameter, increased significantly due to the NaOH treatment (Fig. 3.3). The void number density in the treated sample is about an order of magnitude lower than the value from SEM. A possible reason for this could be that a significant number of voids were located at the metal-oxide interface and were removed during the sample preparation process for TEM i. e. following perforation of the sample by electropolishing. Also, the mechanism through which the chromic-phosphoric acid treatment dissolves and passivates the metal surface is not known. This process could also have led to increased void concentrations during preparation of the SEM samples.

The threshold energy for aluminum above which electron-beam induced displacement of atomic nuclei and degradation of the crystalline structure starts to appear is about 180

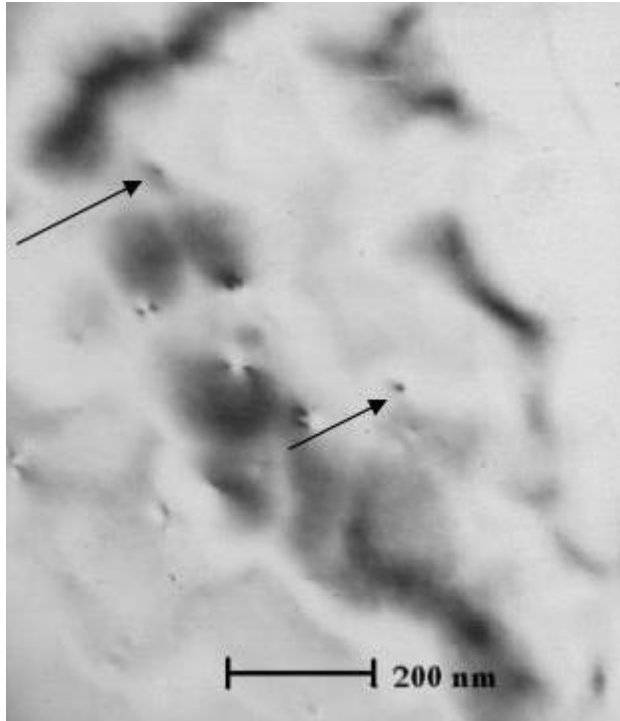


Fig. 3. 7 TEM images of 4N electropolished foil treated in NaOH for 3 min. Accelerating voltage was 150 keV.

keV.^[114,115] In order to rule out beam-induced void formation, the same 3 min treated sample was imaged in the TEM using lower beam currents of 150 keV as compared to 200 keV used for the images in Fig. 3.5. Again, as shown in Fig. 3.7 below, similar features 10-20 nm in size were observed for the treated sample, while they were far less numerous in the untreated sample at the same voltage.

In summary, the PAS studies show that a void-containing defect layer is found beneath the oxide-metal interface for the electropolished aluminum foil. This layer was found to tens of nanometers thick and the inner surface of the constituting voids was free of oxide. FE-SEM images indicated the presence of 10-20 nm voids after anodic oxidation of the metal up to depths of 5 nm but the void population diminished significantly in samples where 23 or 50 nm of the metal was oxidized. Thus, the voids are present in a metal layer less than 20 nm from the metal-oxide interface. TEM and STEM images provide direct evidence of the presence of such voids. The voids were circular in cross-section and around 20 nm in diameter. The number density of voids was found to be about 10^8 cm^{-2} and it increased by at least ten times as a result of alkaline treatment. PAS is a completely nondestructive process. Hence the presence of voids detected though PAS and the similarity between the voids imaged in SEM and TEM/STEM in the same region rules out the possibility that the voids are formed during anodizing in preparing the SEM samples. The alkaline dissolution generates a surface topography consisting of ridges surrounding scalloped depressions. Voids were preferentially located near these ridges, an indication that their formation is coupled to the dissolution mechanism. The oxide-free surface of the voids revealed by PAS shows that the voids are formed internally and not by the dissolution of the metal surface. In spite of the

fast dissolution rate (~ 120 nm/min), these voids continue to appear in measurements at dissolution times when the pre-existing defect layer should have been dissolved away. Thus it can be expected that voids are formed by solid state diffusion of vacancy type defects which occurs rapidly enough to penetrate the metal faster than the rate of dissolution.

Vacancies are generated at the metal-film interface during the dissolution process due to oxidation of aluminum atoms. The voids seen in TEM were about 20 nm diameter and considering Al atomic radius of 125 pm, the voids seen are about 5×10^5 times the size of aluminum atoms or even larger in terms of metal vacancies, since the relaxed atomic volume of vacancies is smaller than the Al atomic volume.^[62] The large size of the voids indicates a high growth rate at room temperature if they are formed by solid state diffusion of vacancies introduced at the metal-film interface. The estimated diffusivity for vacancies should be of the order of R^2/t where R is the radius of the void and t is the dissolution time. For an average void radius of 10 nm and a dissolution time of about 100 s, the expected diffusivity is about 10^{-14} cm²/s. Also, if the metal vacancies are introduced by oxidation of aluminum at the metal-oxide interface and the voids grow by solid state diffusion of these vacancies, the diffusion length for the case of the moving (dissolving) interface is given by $2D/v$,^[36] where D is the diffusivity of the vacancies in Al and v is the dissolution rate of the metal. Considering the void containing layer thickness of about 60 nm from the PAS studies and the calculated dissolution rate of about 2 nm/s in 1 M NaOH from weight loss measurements,^[37] the diffusivity should be around 6×10^{-13} cm²/s. Thus, similar diffusivities of $10^{-14} - 10^{-12}$ cm²/s are estimated from the void size and the void layer thickness. The diffusivity of uncomplexed Al vacancies extrapolated to room temperatures has been found to be $\sim 10^{-12}$

cm^2/s ,^[109, 110] even larger than the estimated vacancy diffusivities in the present work. However, extrapolated diffusivity values from high temperatures might not be entirely reliable since there are thermodynamic factors such as the large vacancy formation energy in Al apparently prohibits room-temperature vacancy injection. Subsurface vacancy diffusion has also been discussed with regard to dealloying processes during corrosion of noble metal alloys. In this work, vacancy complexation has been invoked to explain the diffusion fluxes.^[112, 113] This was not necessary in the present work.

While, monovacancy diffusion can account for void growth, it is more difficult to explain vacancy formation at room-temperature. The vacancy formation energy in Al has been found to be around 0.6eV ^[33] which is much larger than the characteristic energy, kT , which is only 0.026eV at 300K . Recent work by Birnbaum *et al* suggests that vacancies at room temperatures could be thermodynamically feasible since vacancy injection in Al is accompanied by substantial hydrogen absorption^[40] They suggested formation of hydrogen-vacancy defects, which are supposed to agglomerate to form hydrogen bubbles or voids.^[40, 53] The H-vacancy binding energy in Al ($\sim 0.5\text{eV}$ ^[40]) compensates for the high vacancy formation energy at room-temperature. Formation of these H-vacancy defects could be better understood by characterizing the thermodynamic conditions of hydrogen in aluminum, which motivated the measurement of chemical potential of H in Al during the alkaline dissolution process. This will be discussed in the next section.

3.2 Measurement of hydrogen chemical potential during alkaline corrosion of aluminum

This section deals with studies of hydrogen permeation in pure aluminum during chemical corrosion of aluminum in alkaline solutions, using the DS cell and Al/Pd bilayer films discussed earlier. The change in the electrochemical potential on hydrogen entry and exit side was monitored and used to calculate the chemical potential of hydrogen in aluminum. Measurements the permeation current due to hydrogen ionization on the exit side (Pd side) during open circuit chemical charging from the Al side are also presented.

3.2.1 Hydrogen chemical potential measurements during alkaline corrosion of aluminum

Prior to adding solution on the Al side, the open circuit potential of Pd was stable at about ~ 0.28 V (Vs. Ag/AgCl). The Nernst potential for the oxidation of Pd to PdO at pH 7.0 is about 0.29 V (vs. Ag/AgCl).^[1] Hence the Pd surface during this time was in equilibrium with a surface palladium oxide layer. After the potential was stabilized, solutions of various pH values (adjusted by adding NaOH to nanopure water) were poured into the Al side compartment, and the change in the open circuit potential on the Pd side (and Al side in some cases) measured with time. The Pd side open-circuit potential after adding a 1 M NaOH solution (pH ~ 13.5) on the Al side is shown in Fig. 3.8. Zero time corresponds to the moment when the NaOH solution was added. The Al side potential is also shown in the figure. During the experiment, the alkaline solution continuously dissolved the aluminum. Thus, after a certain time depending on the pH value of the NaOH solution, the potentials of the Al side and the Pd side started to approach each other, due to the formation of pinholes in the foil.

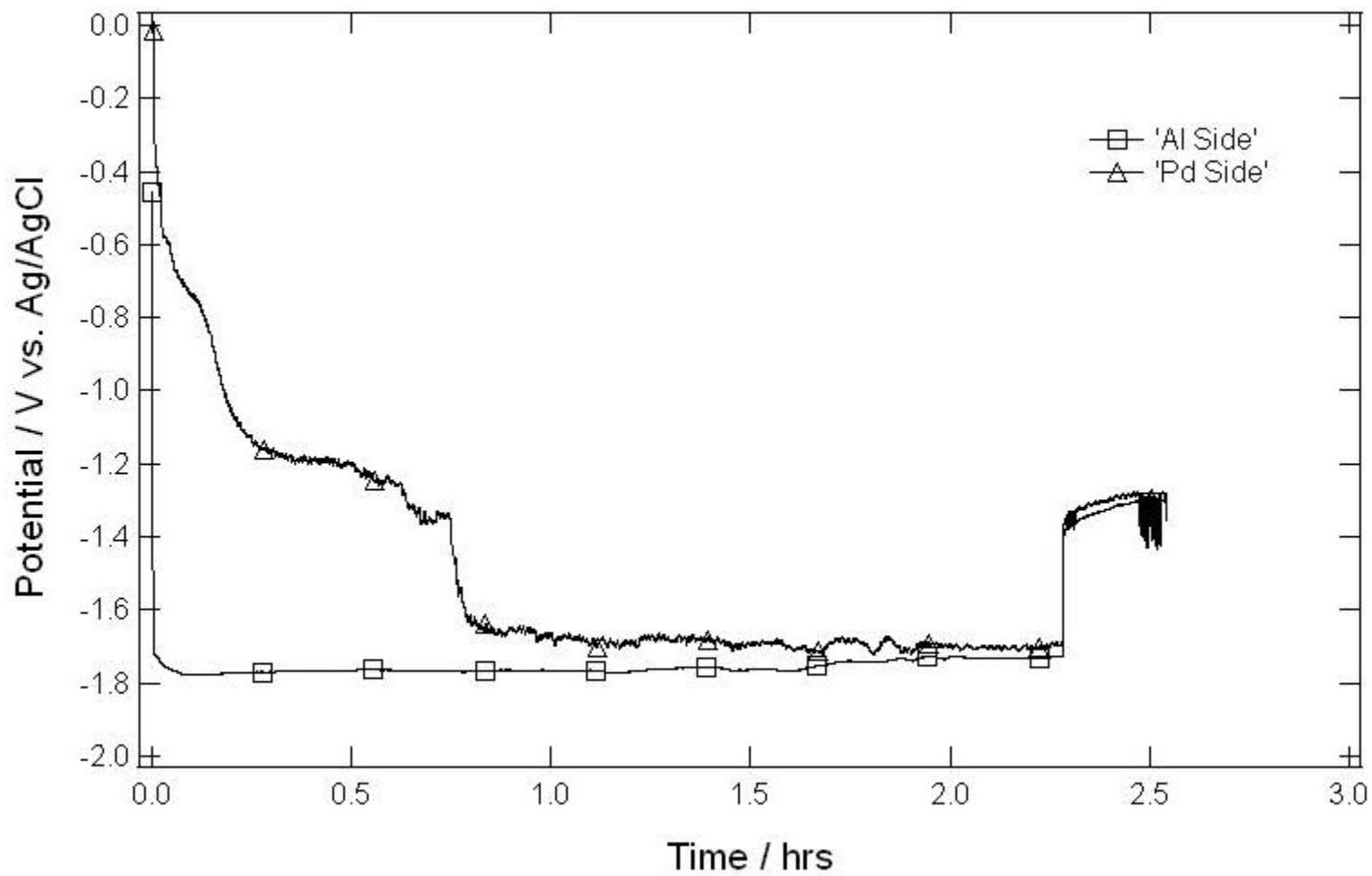


Fig. 3.8 Open circuit potential on Al side (entry) and Pd side (exit) during hydrogen charging by 1M NaOH solution.

Finally the foil dissolved away completely mixing the solution in the two compartments, and the potentials on both sides showed an abrupt jump and merged together. The time taken for complete dissolution of the foil was about 135 min which gives an average dissolution rate of 180 nm/min at pH 13.5. This is quite similar to the dissolution rate of 220 nm/min found for 99.98% purity aluminum in the same 1 M NaOH solution from weight loss experiments.^[37]

Pd side open-circuit potential measurements for NaOH solutions of pH values 11, 12, 12.5, 13.0 and 13.5 are shown at two different time scales in Fig. 3.9. The plot shows two experiments at each pH value, confirming the reproducibility of the transients. The zero time is again the moment when the NaOH solution is added into the aluminum side compartment of the DS cell. All transients start from an initial potential of about 0.28 V where the palladium is in equilibrium with PdO as mentioned earlier. Then, except at pH 11, each transient passed through 2 or 3 potential arrests, representing different electrochemical reactions on the Pd. The first arrest at -0.1 V appeared as a point of inflexion at pH 13.5 but as a well-defined plateau at other pH values. Cyclic voltammetry (CV) scans of the Pd in the pH 7.0 buffer, without any hydrogen charging from the Al side, were carried out to identify the arrest. The CV scan is shown in Fig 3.10. The potentials were corrected for the ohmic drop with a calculated cell resistance of 1050 $\Omega\text{-cm}^2$ for the current cell configuration, measured from potential-step measurements with the pH 7.0 buffer solution on the Pd side. The CV shows a PdO reduction peak from -0.1 V to 0.2 V.^[1] Since the arrest potential of -0.1 V is on the negative side of the peak, the arrest corresponds to the reduction of PdO by H diffused from the Al side. Hence at these times, the H chemical potential had increased sufficiently to reduce the PdO.

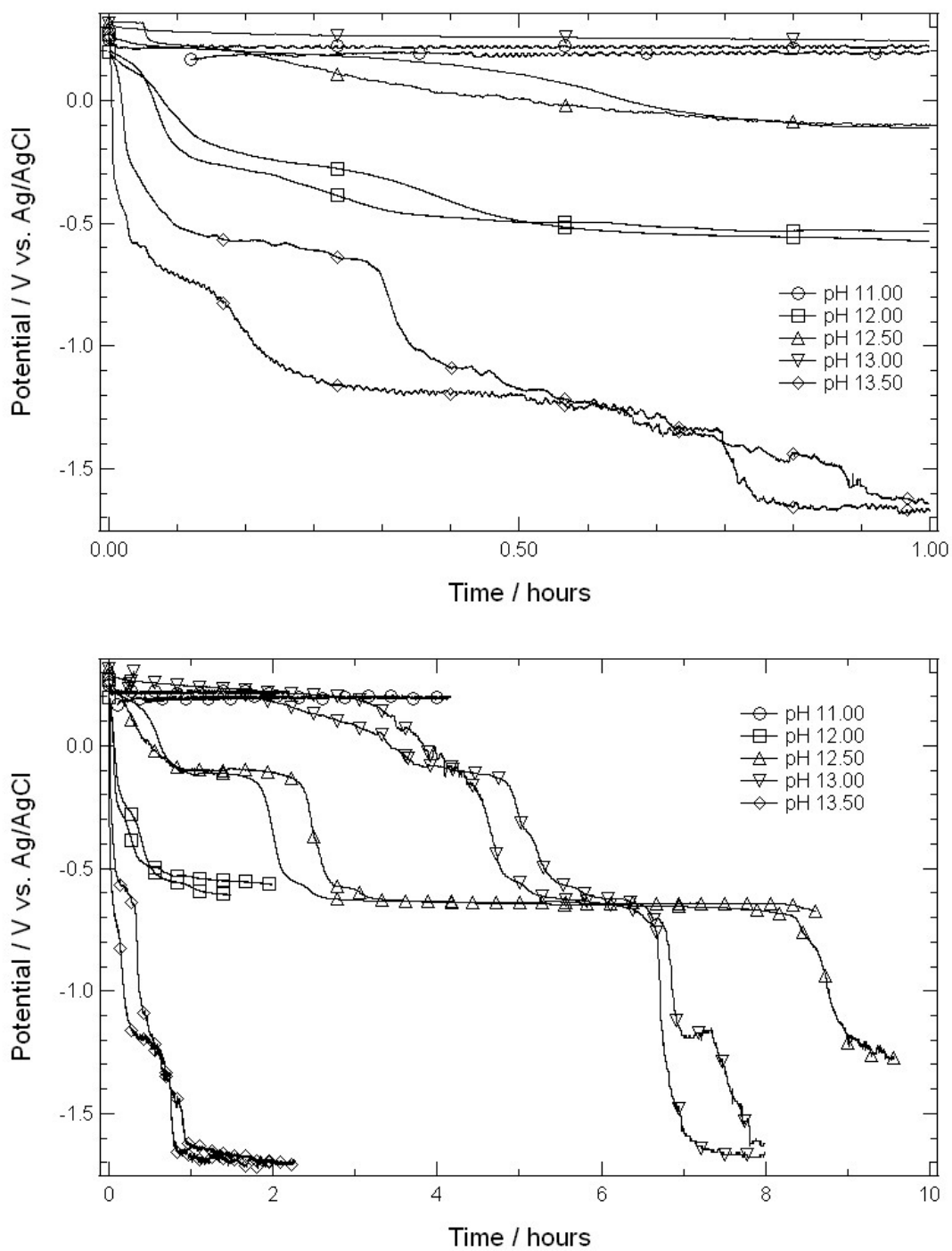


Fig.3.9 Open-circuit potential transients on hydrogen exit (Pd) side with solutions of various pH on the Al side. The top and bottom plots are the same transients plotted to different time scales.

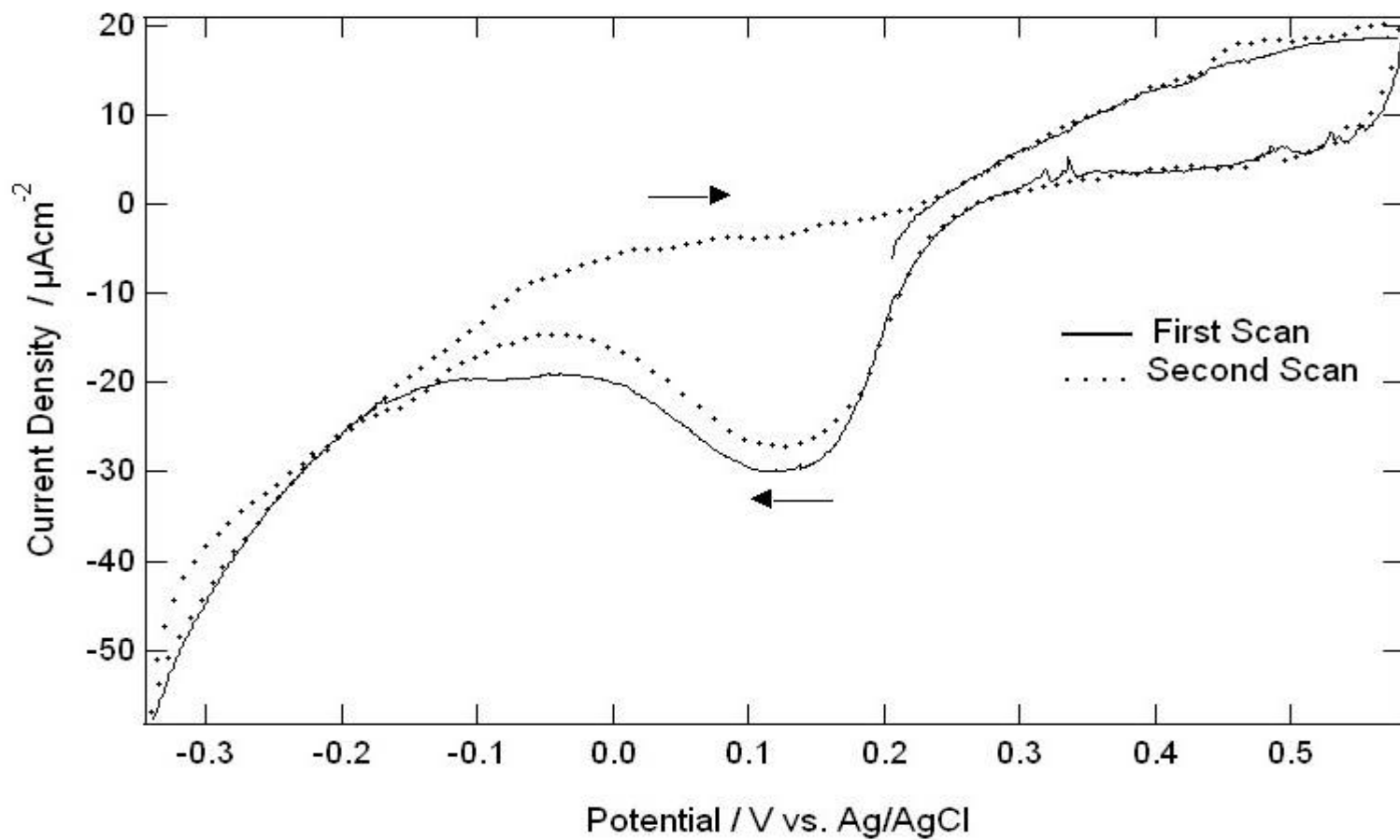


Fig. 3.10 CV scans for Pd in pH 7.0 buffer solution before charging with hydrogen from the Al side. The potentials are corrected for ohmic drop using the cell resistance $R_s = 1050 \Omega\text{cm}^2$.

Another plateau is seen in Fig. 3.9 at about -0.5 to -0.6 V. However, note that the transient for pH 11.00 does not show either arrest, probably because the rate of H-absorption is too small to induce chemical processes on the exit side. The Nernst potential for Pd₂H formation at pH 7.0 is about -0.56 V (vs. Ag/AgCl).^[1] A CV scan for the Pd film after H-charging in 1 M NaOH (pH 13.5), to the time when the Pd potential reaches -0.6 V, is shown in Fig. 3.11. The NaOH solution on the Al side was removed to prevent further H absorption into the metal prior to starting the CV scan. Fig 3.11 shows an oxidation peak around -0.55 V which is close to the Nernst potential for Pd₂H formation. Thus, this plateau corresponds to the chemical reaction of H with Pd to form Pd₂H. The forward scan in the second cycle shows a higher hydride oxidation peak, probably because of additional hydrogen absorbed during the reverse scan of the first cycle.

In the pH 13.5 transient, another plateau is seen at a potential of about -1.23 V. A small potential arrest is also seen for one of the pH 13.0 transients though at a slightly higher potential ~ -1.17 V. The final decreases of potential below -1.23 V for the pH 13.5 transients and below -0.6 V for the others corresponds to penetration of the Al foil by dissolution as shown earlier in Fig. 3.8. The measured potential after this final decrease is of no fundamental significance, since it is determined by the OCP of the aluminum. Since there is no evidence of a hydride phase other than Pd₂H at a high equivalent hydrogen pressure, we interpret the plateau potential of -1.23 V in the pH 13.5 experiment (from Fig. 3.9) as the state in which H is close to equilibrium with the Al side of the membrane. The other

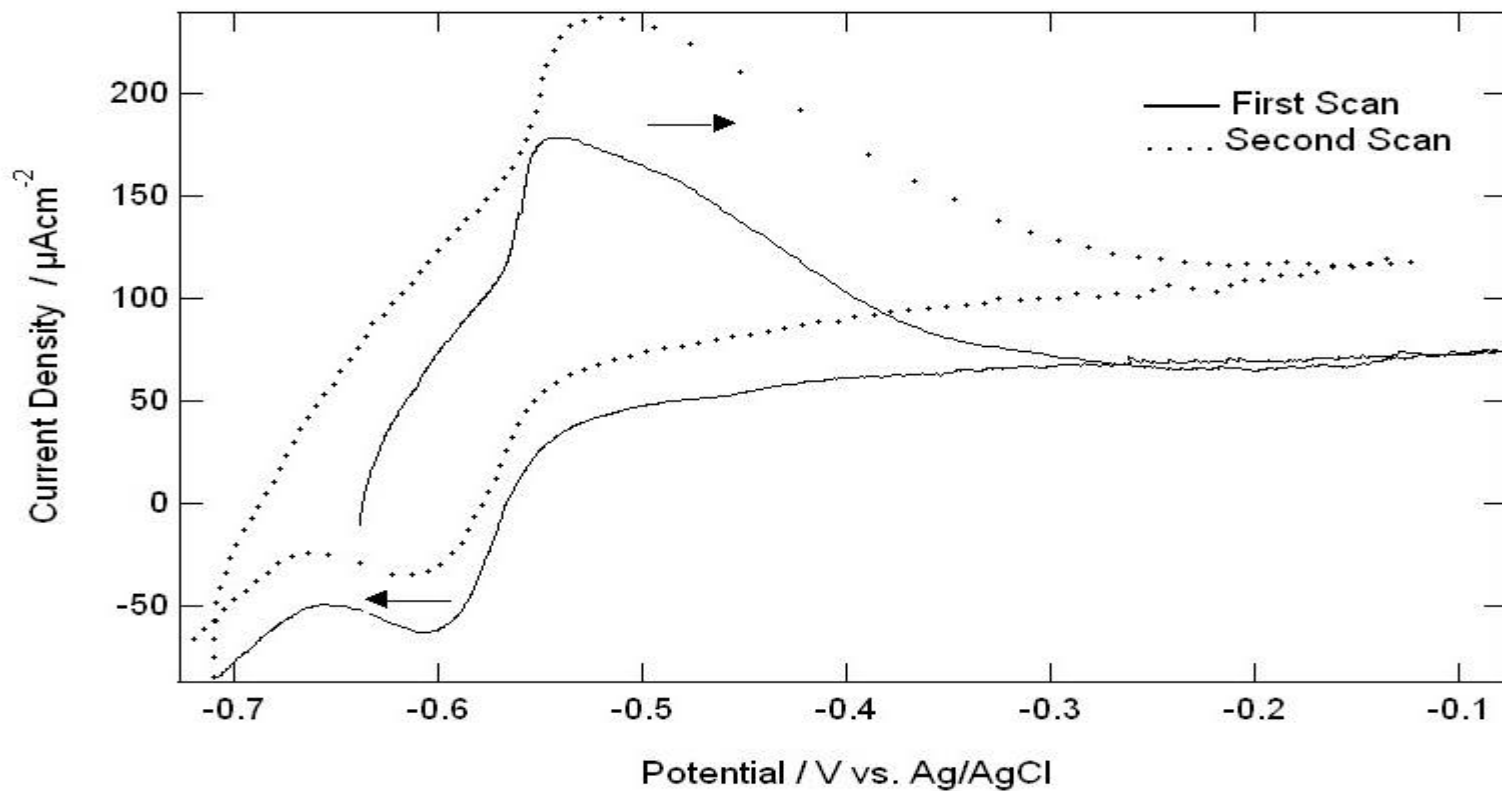


Fig. 3.11 CV scans for Pd in pH 7.0 buffer solution after H-charging by pH 13.5 NaOH up to an open circuit potential of -0.6 V. The NaOH solution was then removed from the Al side compartment and the CV started. The potentials are corrected for ohmic drop with the cell resistance $R_s = 1050 \text{ ohm.cm}^2$.

experiments at pH values less than 13.5 did not approach equilibrium with the Al because the hydrogen chemical potential was too small to convert all the Pd into Pd₂H on the experimental time scale.

In order to improve the response time of the Pd layer, additional experiments were carried out in which the Pd film was converted to Pd₂H by cathodic charging, prior to the open-circuit hydrogen injection. The OCP of cathodically charged Pd₂H for pH values of 12, 12.5 and 13 are shown in Fig. 3.12. It can be seen that the potential before the solution on the Al side is poured is ~ -0.6 V, corresponding to the Nernst potential and the plateau of Pd₂H formation in Fig. 3.10. Plateaus for both pH 13 and 12.5 were seen at the more negative potential of ~ -1.13 V (vs. Ag/AgCl). This plateau potential is again attributed to equilibrium of H with the Al side. No plateau is seen for pH 12 since evidently the permeation rate was too small to convert the remaining Pd to Pd₂H.

There were no significant irreversible changes in the Pd film due to corrosion and the OCP transients reflected the changes in the chemical potential of hydrogen in the Al membrane. This is indicated by Fig. 3. 13 which shows potential transients on the Pd side for experiments which were begun with a high pH (12.00 or 13.50) solution on the Al side and then interrupted and replaced with a lower pH (10.00 or 7.00) solution. The two transients shown for pH 13.50 are the same at two different time scales. In the case of charging with the pH 12.00 solution, the experiment was interrupted just after the reduction of the PdO. The Pd side potential in this case increased and went back to the PdO formation potential since the H-absorption in to the membrane due to the pH 10.00 NaOH was very small. The pH 13.50 transient was interrupted close to the last plateau (~ -1.22 V) after the Pd₂H film had already

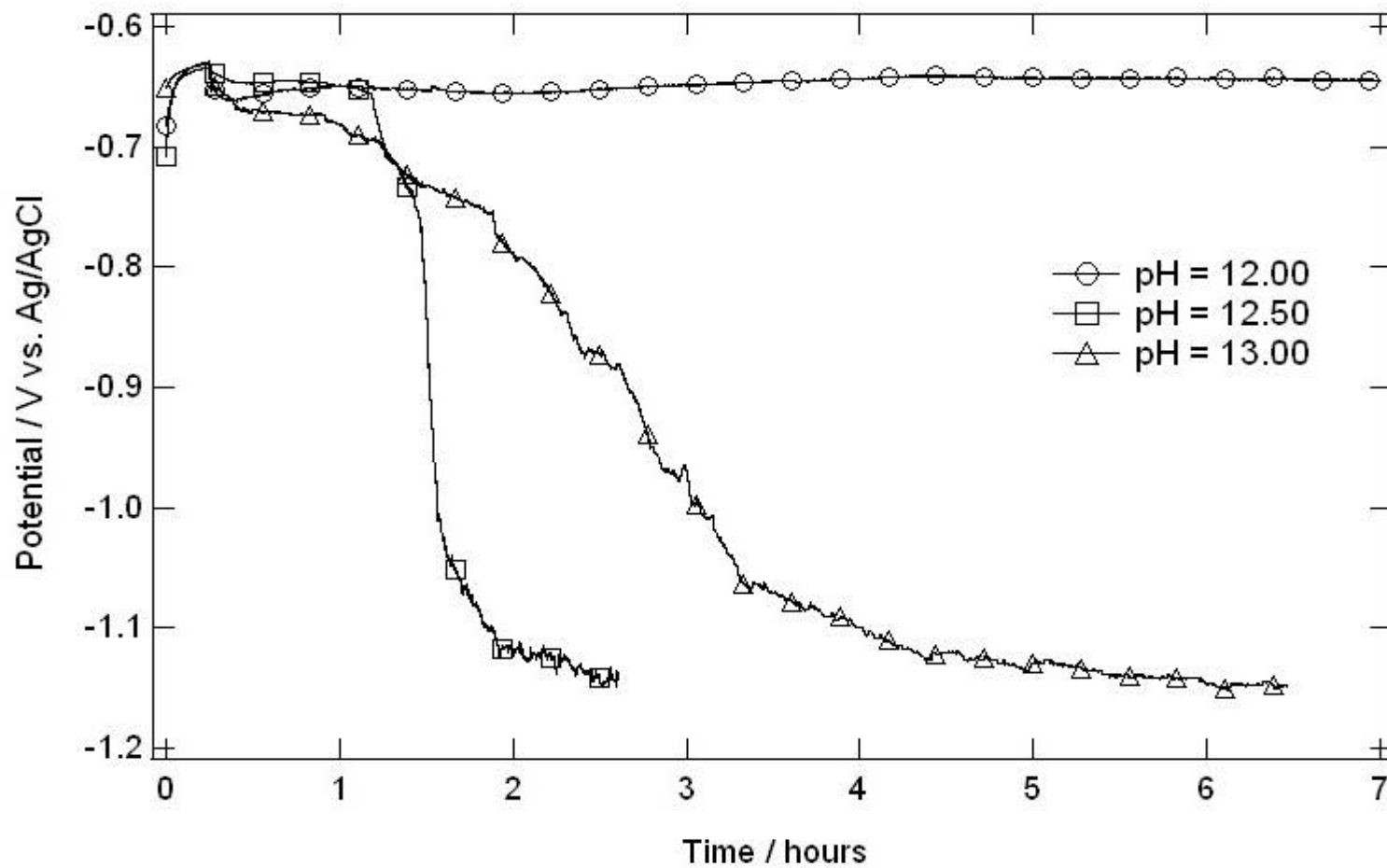


Fig. 3.12 Open-circuit potential transients on hydrogen exit (Pd) side with solutions of various pH on the Al side. The Pd side was cathodically charged to form Pd₂H before commencement of charging from Al side.

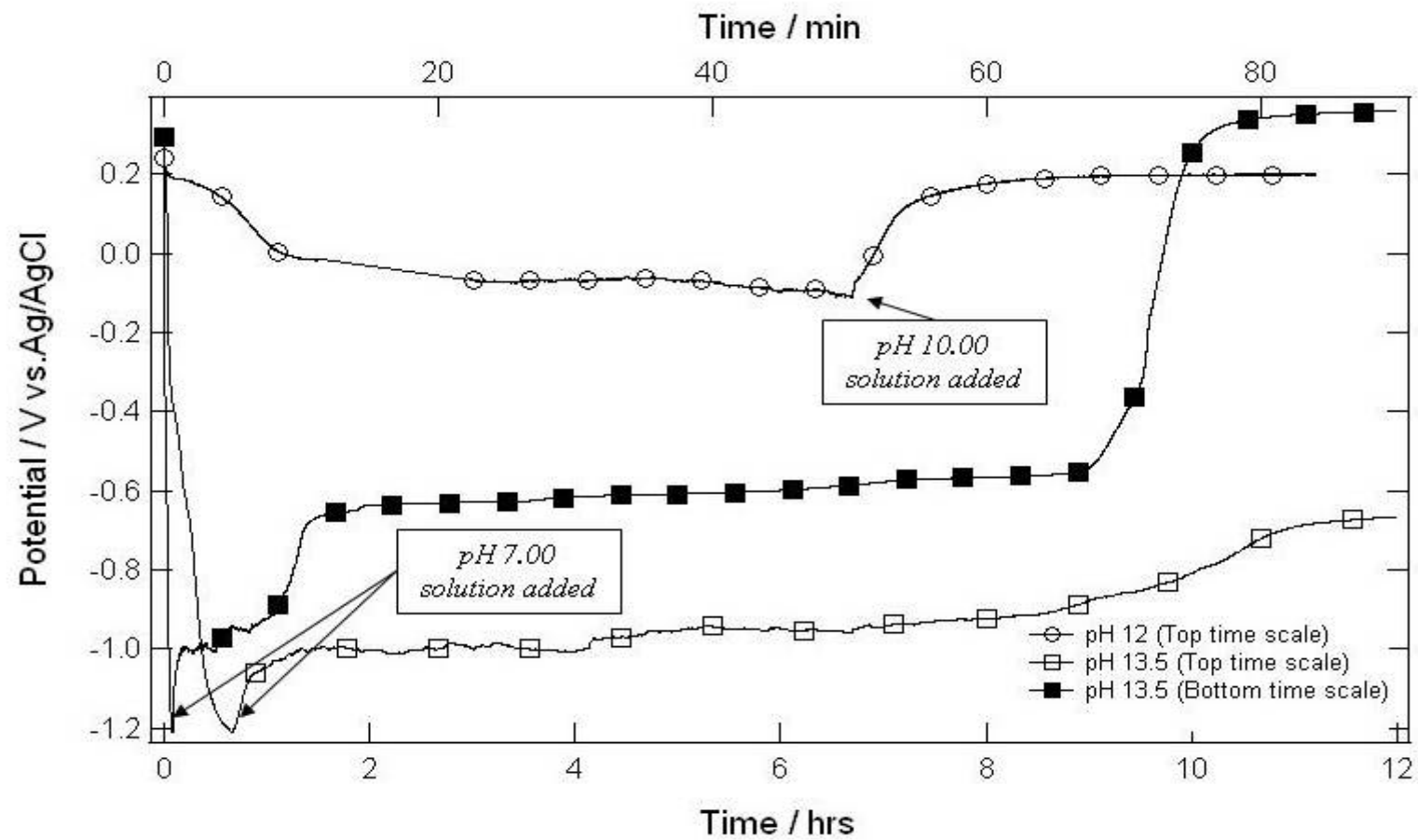


Fig. 3.13 Open circuit potential on the Pd (exit) side before and after interruption and replacement of a high pH (12.00/13.50) NaOH solution with a lower pH (10.00/7.00) solution on the Al entry side.

formed. On replacing the solution with a pH 7.00 solution, the potential again started drifting in the positive direction showing a decrease in the chemical potential of H since the rate of hydrogen leaving the membrane from the Pd side was faster than the rate of H-absorption from the Al side. In both cases, if there was a permanent change in the Pd film due to corrosion, the potentials would not have relaxed on decreasing the pH on the Al side.

The hydrogen chemical potential in Al (μ_H) can be calculated from the measured Pd potential at equilibrium with Al. The Pd potential is given by

$$E = E_{H_2}^0 - 2.303 \frac{RT}{F} pH - \left(\mu_H - \frac{1}{2} \mu_{H_2}^0 \right) \quad (3.3)$$

where $E_{H_2}^0$ is the standard electrode potential for the NHE (-0.20 V vs. Ag/AgCl reference electrode), F is Faraday's constant, and $\mu_{H_2}^0$ is the chemical potential of H_2 in the standard state (ideal gas at 1 atm pressure and 298.16 K). Setting $E = -1.23$ V for the pH 13.5 solution, and pH as 7.0 for the Pd side on which the potential was measured, we get a value of 0.62 eV for $\mu_H - \frac{1}{2} \mu_{H_2}^0$ at pH 13.5. The same treatment for the pH 13.0 and pH 12.5 equilibrium

potential of -1.13 V gives a value of $\mu_H - \frac{1}{2} \mu_{H_2}^0 = 0.52$ eV for pH 13.0 and pH 12.5.

Given the potential and pH of the Al side, we can calculate the value of $\mu_H - \frac{1}{2} \mu_{H_2}^0$ which would be in equilibrium with the Al side solution according to Eqn. 3.3. The Al side potentials are shown in Fig. 3.14 below. Table 3.1 below summarizes the values of Al side

OCP and corresponding equilibrium values of $\mu_H - \frac{1}{2}\mu_{H_2}^0$ for the various pH solutions. The

chemical potential $\mu_H - \frac{1}{2}\mu_{H_2}^0$ is related to the hydrogen fugacity f_{H_2} in equilibrium with the

metal by

$$\mu_H - \frac{1}{2}\mu_{H_2}^0 = \frac{1}{2}RT \ln(f_{H_2}) \quad (3.4)$$

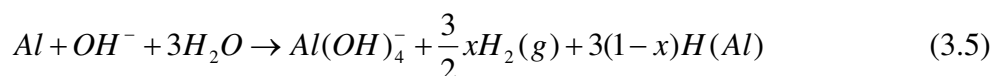
Table 3.1 Values of actual μ_H (calculated from Al side OCP) and equilibrium μ_H (calculated from Pd side OCP) for various pH values.

<i>pH</i>	<i>E_{Pd}</i> (vs. Ag/AgCl)	<i>E_{Al}</i> (vs. Ag/AgCl)	$\mu_H - \frac{1}{2}\mu_{H_2}^0$ (Al, measured)	$\mu_H - \frac{1}{2}\mu_{H_2}^0$ (Al, equilibrium)
13.50	-1.23 V	-1.77 V	0.62 eV	0.77 eV
13.00	-1.13 V	-1.86 V	0.52 eV	0.90 eV
12.50	-1.13 V	-1.80 V	0.52 eV	0.86 eV
12.00	-	-1.71 V	-	0.80eV
11.00	-	-1.62 V	-	0.77eV

This equation gives fugacity values of 6.78×10^{20} atm for pH 13.5 and 2.96×10^{17} atm for pH 13.0. These extremely high hydrogen fugacities in aluminum are confirmation that a very high concentration of hydrogen is introduced into the metal. Very large hydrogen fugacities

of $\sim 10^{15}$ atm were also inferred by Buckley *et al* from analytical measurements of H in the metal after alkaline dissolution. However, they found that the high H-concentrations in Al did not increase the lattice parameter of the metal. This was attributed to the formation of complexes with vacancies injected into the metal by the dissolution process.^[16, 40] The association of H with vacancies is energetically favored because of the large binding energy of H to aluminum vacancies. The lower measured H chemical potentials compared to the equilibrium values (Table 3.1) may be attributed to a kinetic barrier for H entry at the Al/solution interface. The measured hydrogen chemical potential values of ~ 0.52 - 0.62 eV are very close to the vacancy-hydrogen binding energy in Al of ~ 0.5 eV.^[40] Thus, it is possible that all the hydrogen complexes with a vacancy formed from metal oxidation right at the interface and almost all the hydrogen entering the metal is in the form of hydrogen-vacancy defects.

One of the intriguing features of the OCP transients seen in Fig. 3.10 is the time dependence of these transients. It can be seen that the pH 13.5 transients reach the potential corresponding to Pd₂H formation fastest. This is followed by transients for pH 12, 12.5 and 13 in that order. Thus, a regular trend with hydrogen absorption rates with increasing pH is not seen although the dissolution rates display an increasing trend with pH as seen in Fig. 3.15 below. The rate of the overall hydrogen formation (combined gas and metal phase) is proportional to the open circuit dissolution rate.



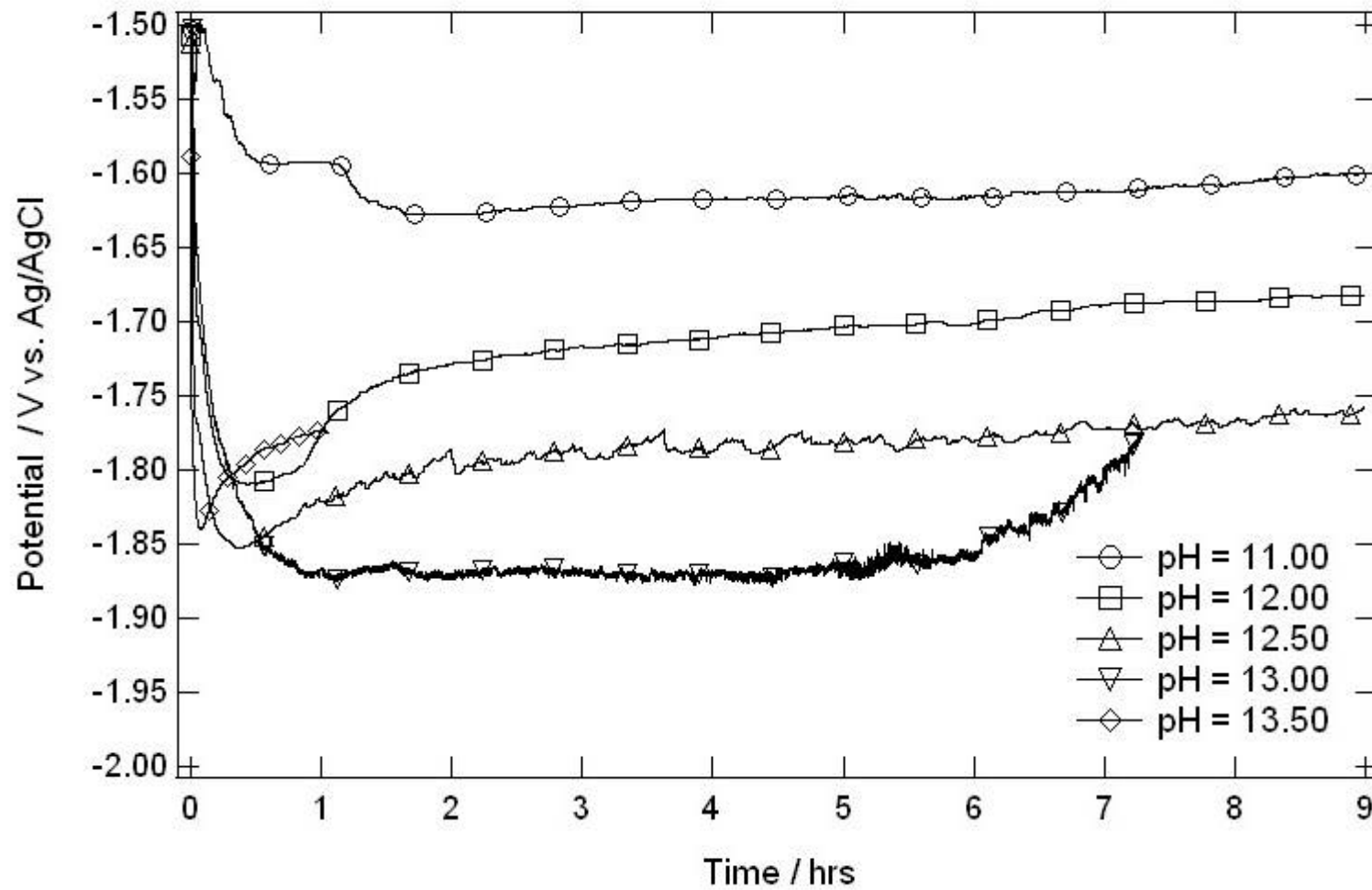


Fig. 3.14 Open-circuit potential transients on hydrogen entry (Al) side during charging with NaOH solutions of various pH on the Al side.

Dissolution rates below pH 12 could not be measured reliably since the metal dissolution was too slow to perforate through the entire foil and the pH of the solution also decreased appreciably from its initial pH value because of the consumption of OH^- ions. In any case, the potential response time is evidently not determined by the overall rate of hydrogen formation. The response time of E_{Pd} might also be determined by μ_H on the Al side, which provides the driving force H diffusion through the membrane. However, the trend with pH of the calculated equilibrium μ_H values (Table 3.1) and that of the E_{Pd} response time are not the same. Both E_{Pd} and E_{Al} transients have been shown to be reproducible. Thus, there may be considerable complexity involved in the process of hydrogen absorption in the metal.

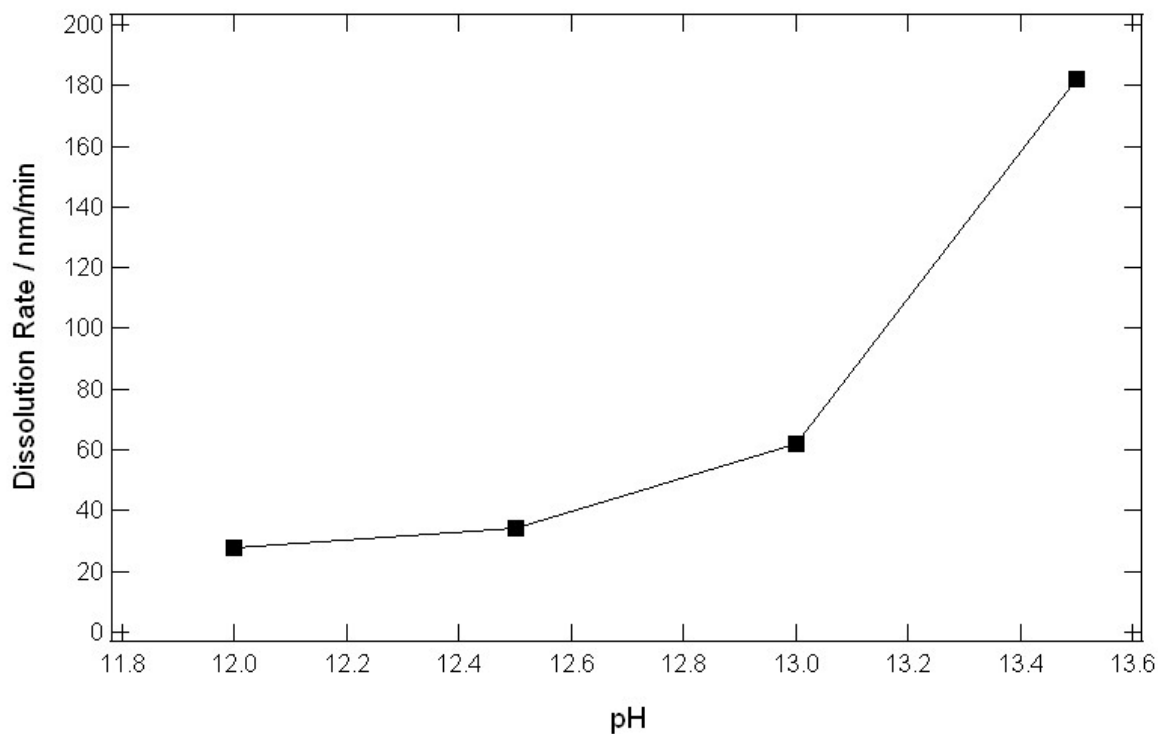


Fig. 3.15

Dissolution rates for Al foil in NaOH solutions of various pH values.

3.2.2 Hydrogen permeation measurements during alkaline dissolution of Al

Measurements of H permeation were carried out to determine whether our experiments displayed typical permeation behavior documented in literature. Fig. 3.16 and Fig. 3.17 show 2 runs each for permeation current measurements with 0.1 M (pH 13.0) and 1 M NaOH (pH 13.5), respectively, on the Al side, with a constant anodic potential of 45 mV(vs. Ag/AgCl) applied on the Pd side. Although the initial currents for one of the runs with 1 M NaOH were high, both experiments display comparable steady state permeation current values. The noise seen in the current signal is because of formation of bubbles on the hydrogen entry as well as exit side which grow for some time, and periodically break free, resulting in a changing surface area which affects the hydrogen flux. Also, the permeation current in both cases decreases from its initial background value for about 30 s, before starting to increase as in a typical diffusional process. This initial decrease of permeation current has been observed in a number of hydrogen permeation studies and has been attributed by some workers to changing hydrogen entry flux because of changing electrolyte composition close to the entry side.^[52] The changing solution composition could affect the aluminum oxide composition which in turn would affect the hydrogen entry flux. Stress effects by formation of solid phase surface layers like aluminum hydride causing back diffusion of hydrogen have also been argued to be the reason for this decrease in early time permeation currents.^[70-72]

The permeation currents showing increasing trends with time can be interpreted in terms of the characteristic transient for diffusion of hydrogen through the Al foil. A number

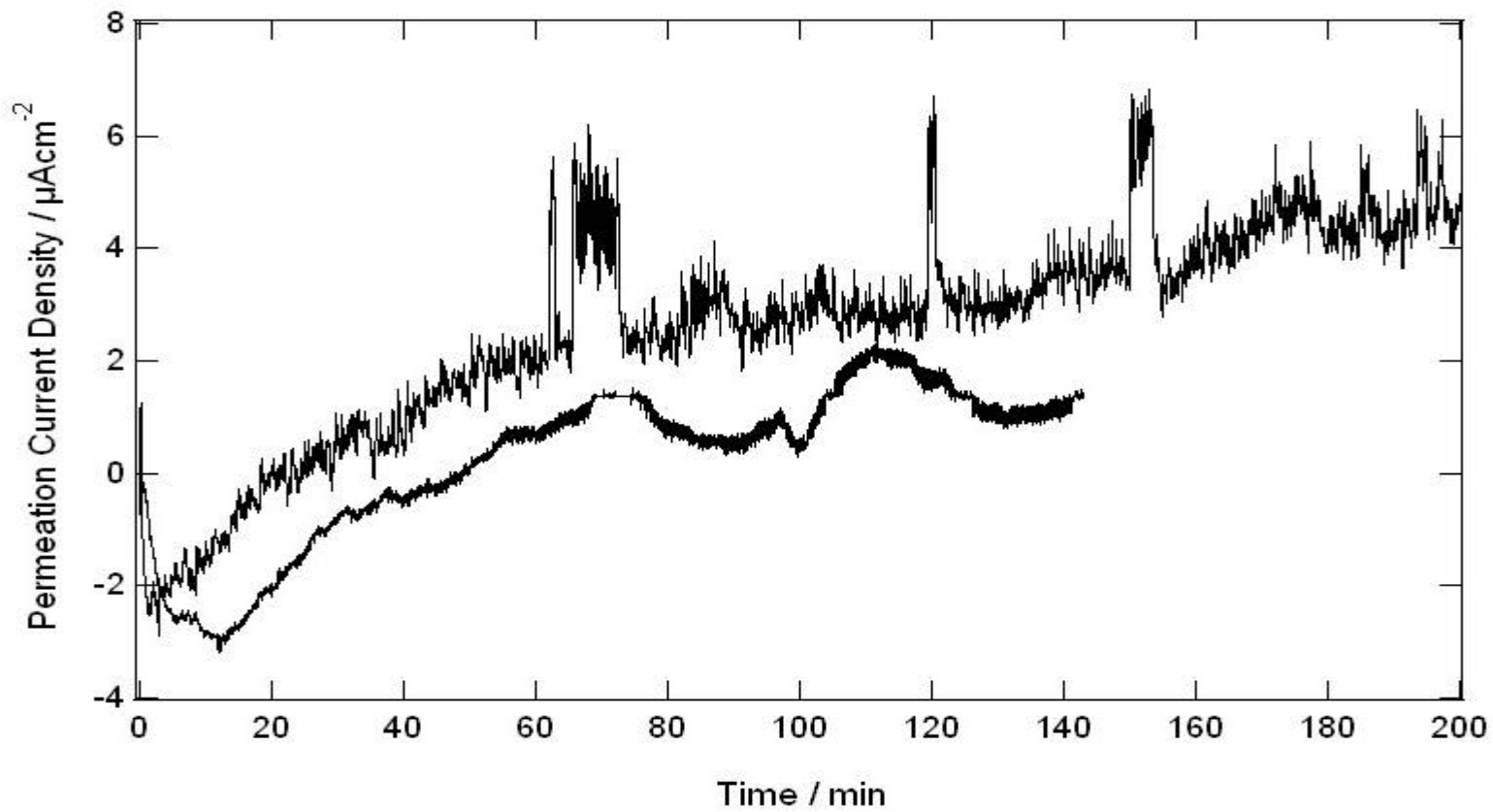


Fig. 3.16 Permeation current for Pd electrode in pH 7.0 buffer solution at a constant anodic applied potential of 45 mV (vs. Ag/AgCl). Al side solution was 0.1M NaOH (pH 13.0) solution at open circuit.

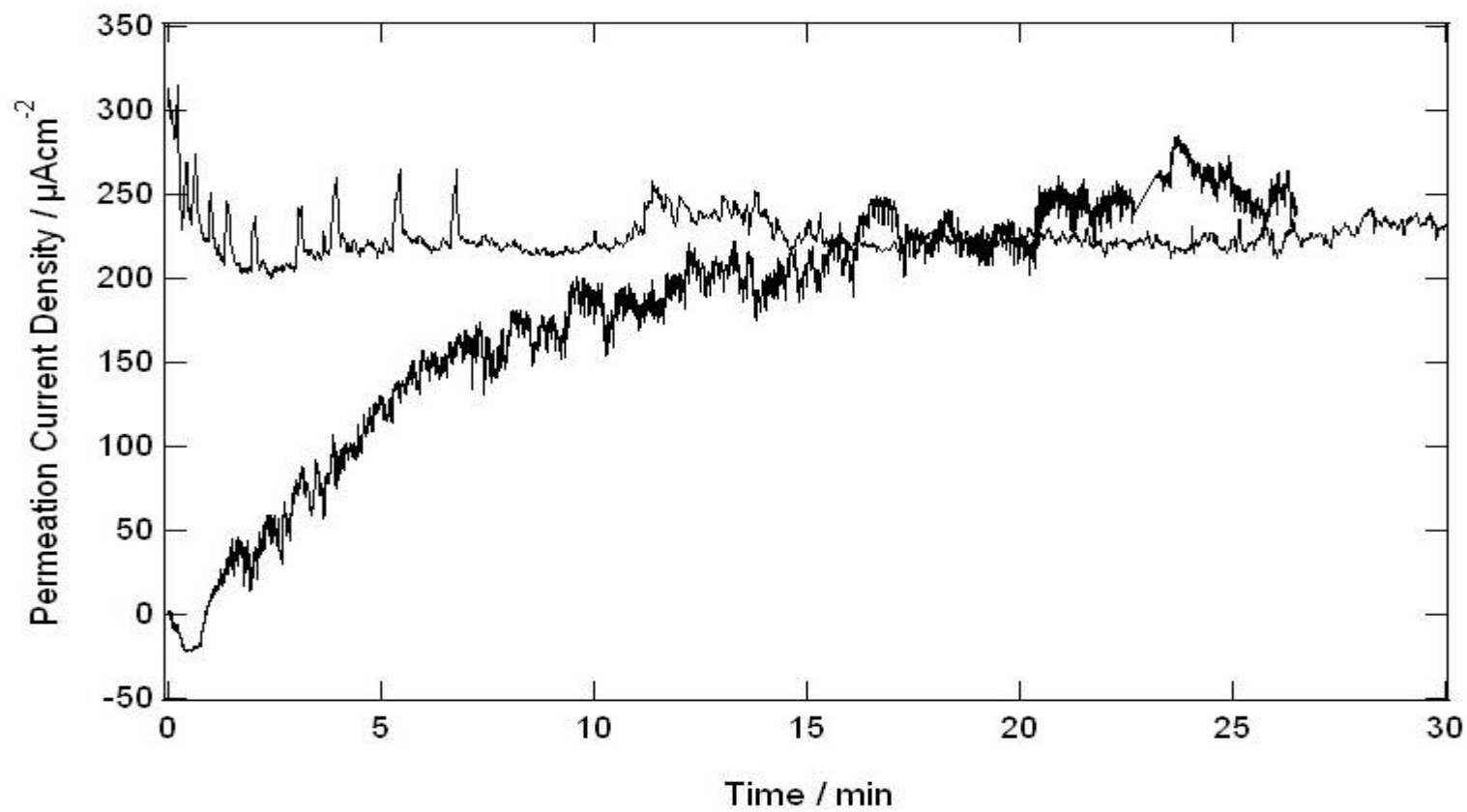


Fig. 3.17 Permeation current for Pd electrode in pH 7.0 buffer solution at a constant anodic applied potential of 45 mV (vs. Ag/AgCl). Al side solution was 1M NaOH (pH 13.5) solution at open circuit.

of ways have been suggested for calculation of the diffusion coefficient from permeation current – time data.^[73] The more reliable forms involve using a majority of the data points rather than using breakthrough times when the current values reach a certain fraction of the steady state current. The permeation current flux is related to the diffusivity and time by the equation

$$\ln(Jt^{1/2}) = \text{const} - \frac{L^2}{4Dt} \quad (3.6)$$

where J is the permeation current flux (in A/cm^2), t is the time elapsed, L is the thickness of the foil and D is the diffusion coefficient.^[52, 73] Thus, D can be obtained from the slope of a plot of $\ln(Jt^{1/2})$ vs. $1/t$. Such a plot for the case of chemical charging of hydrogen using the 1 M NaOH solution is shown in Fig. 3.18. Using the foil thickness of 25 μm , the diffusion coefficient was calculated from the slope of the fitted straight line and found to be $3.01 \times 10^{-9} \text{ cm}^2/\text{s}$. The calculated diffusion coefficient for the two cases of H-charging with 0.1 M NaOH were found to be $3.79 \times 10^{-11} \text{ cm}^2/\text{s}$ and $2.53 \times 10^{-10} \text{ cm}^2/\text{s}$, which are about 1-2 orders of magnitude smaller.

The values of hydrogen diffusivity in pure aluminum at room temperature (20° C) in literature show a large amount of scatter ranging from 10^{-20} to $10^{-7} \text{ cm}^2/\text{s}$.^[74] The discrepancies are attributed to variations in hydrogen transport behavior in the oxide film on aluminum which is always present in varying thicknesses and compositions on both sides of the Al foil, depending on the experimental conditions. The diffusivity in the oxide is typically orders of magnitude smaller than in bulk aluminum. Fowler et al found that the diffusion coefficient for tritium in sintered forms of aluminum oxide was about $4.2 \times 10^{-28} \text{ cm}^2/\text{s}$ and also that it is very sensitive to the impurity concentration in the oxide.^[75] The

scatter in the diffusivity values of hydrogen in high purity aluminum is also associated with trapping sites for hydrogen like dislocations and vacancies with corresponding binding energies of 0.24 eV and 0.6 eV respectively.^[74] Such trapping sites especially vacancies, because of their stronger binding energies can have a large impact on hydrogen diffusion through aluminum.

The diffusivity of H in the metal should not depend on the pH of the solution under similar experimental conditions. Hence, the unusual order of E_{Pd} response time with pH can not be understood in terms of diffusion alone. However it is possible that the diffusivity is influenced by the rate of injection of vacancies at the Al surface, which could depend on the pH of the solution. As mentioned earlier, evidence of high concentrations of vacancies and vacancy-hydrogen interactions in aluminum during hydrogen absorption are not uncommon.^[40-43, 45-48] However, explaining the large values of μ_H observed and the formation of room temperature voids requires a better understanding of the surface chemistry of involved processes, especially the presence of hydrogen containing species during alkaline dissolution of aluminum. An extensive study of surface species during the dissolution process was conducted using SIMS and AFM. The potential at the metal-film interface during anodic dissolution was also identified by analyzing CV and potential-step experiments. This work is discussed in the following chapters.

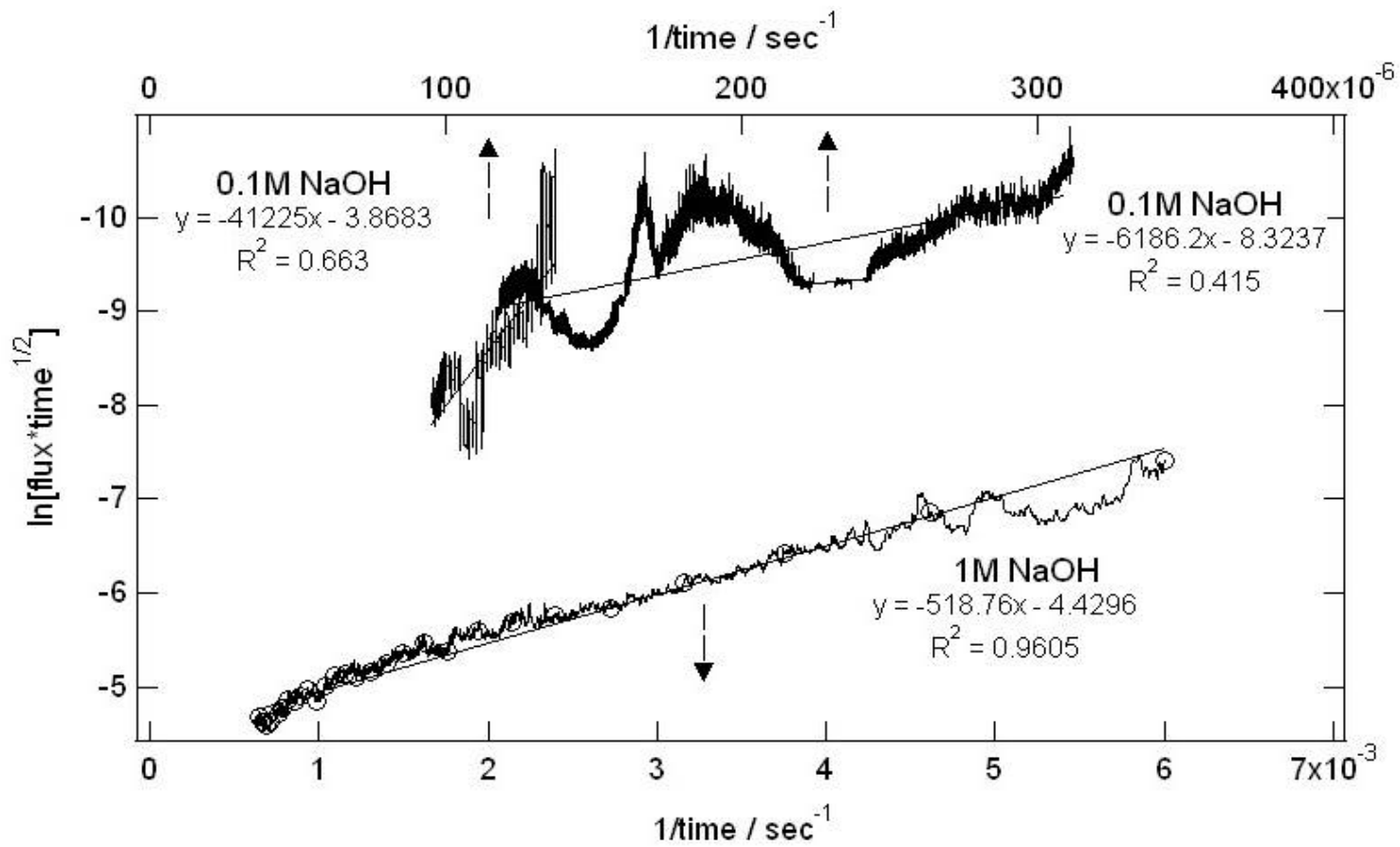


Fig. 3.18 Calculation of diffusion coefficient for hydrogen ingress in Al during dissolution in 1 M NaOH solution. Flux is in A/cm^2 .

3.3 Detection of hydrogen-containing species during alkaline dissolution of aluminum

The results of a study of the electrochemical behavior of aluminum in alkaline solutions are presented in this chapter. The role of hydrogen containing surface species will be investigated with the help of secondary ion mass spectroscopy and atomic force microscopy. Implications of the observations will then be discussed.

3.3.1 A SIMS study of aluminum dissolution in alkaline solutions

As mentioned earlier in the experimental section, electropolished 4N foils were used for most SIMS measurements and alkaline dissolution was studied in 1 M NaOD/D₂O solutions in order to differentiate from hydrogen adsorbed from air during the dissolution and transfer processes. A set of depth profiles of all the major negative secondary ions in the 4N aluminum foil after a treatment in the deuterioxide solution for 14.5 min is shown below in Fig. 3.19. The highest counts amongst the secondary ions detected were for Al₂⁻ and Al⁻ in the bulk metal and AlO⁻ and O⁻ in the oxide. Apart from these, distinct profiles of deuterium containing species D⁻, AlD⁻ and OD⁻ were also observed. Table 3.2 below shows the theoretical masses of the deuterium containing peaks and the corresponding mass deviations for those species obtained from the SIMS data peaks.

Table 3.2 Masses of SIMS peaks for D containing species (for measurements in Fig.3.19).

<i>Peak Mass (amu)</i>	<i>Species Assigned</i>	<i>Mass Deviation ($\times 10^{-3}$ amu)</i>
2.0141	D ⁻	0.2
17.9991	OD ⁻	-0.3
	H ₂ O	11.4
28.9956	AlD ⁻	-1.6
	CHO ⁻	5.5

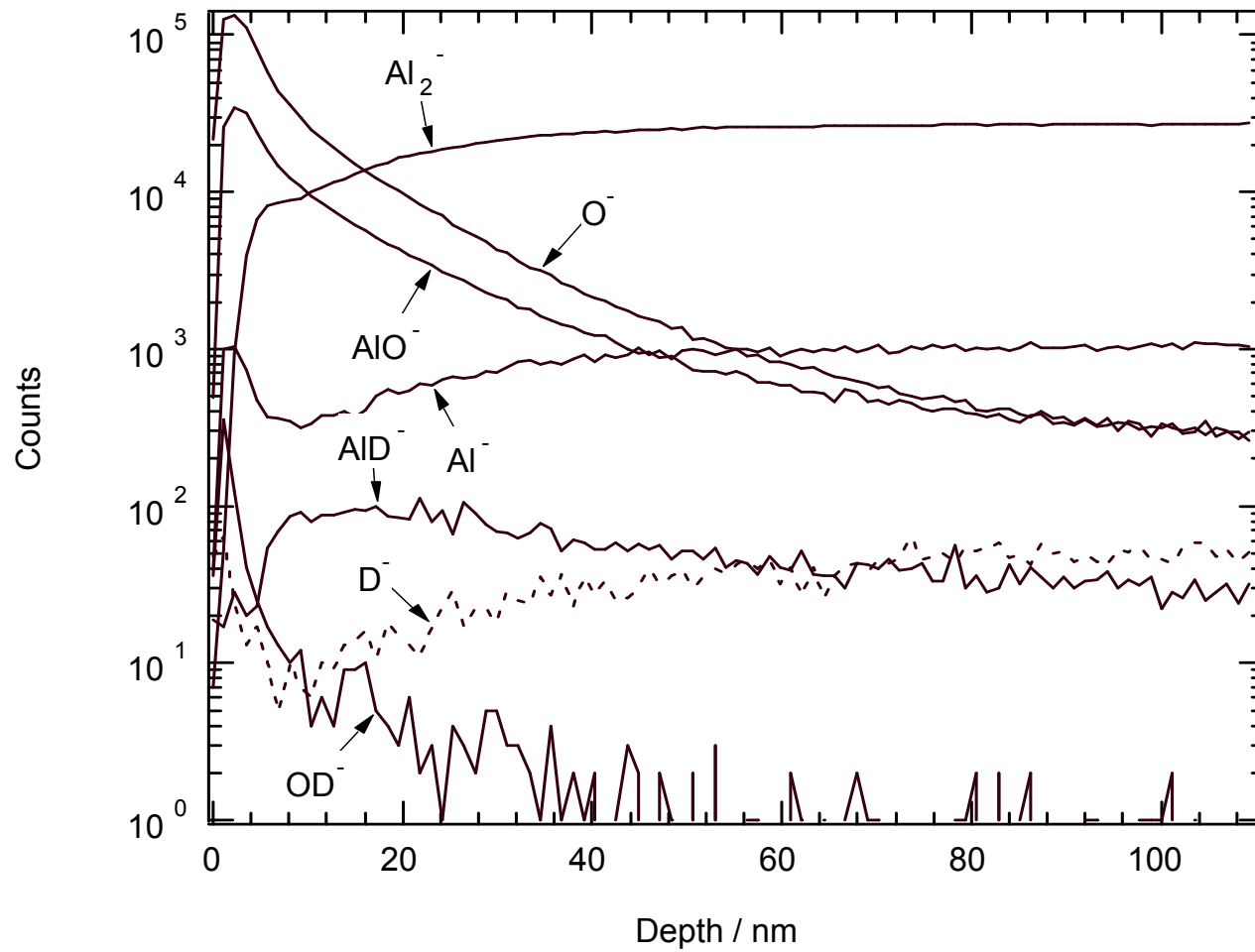


Fig. 3.19 SIMS profiles after caustic dissolution of 99.99% Al for 14.5 min.

The deviations were found to be 0.0002, 0.0003 and 0.00114 amu for D^- , OD^- and AlD^- respectively. Two separate peaks for OD^- and H_2O were always seen at around mass 18 for all NaOD treated while only the one corresponding to H_2O was seen in the as-electropolished sample. Similarly, the AlD^- peak seen around mass 29 was absent in the as-electropolished (untreated) sample unlike the CHO^- peak (probably arising from surface contamination during the NaOD treatment and transfer processes), which was present in the treated as well as untreated samples. The AlD^- peak shows a very clear dependence on the alkaline dissolution time which further justifies its assignment to that particular atomic mass value. The profiles for an as-electropolished sample are shown in Fig. 3.20 where the D^- , AlD^- and OD^- counts are measured for the same atomic masses as observed in the 14.5 min sample. The signals are much smaller and are probably due to background contamination. It can be seen in Fig.3.20 that both the AlO^- and the O^- profiles increase to a maximum value at a very small depth and then decrease sharply to much lower counts. The depth at which the AlO^- counts fall down to 50% of its maximum value (also marked by a sharp change in slope of the Al_2^- profile) is considered to be the position of the oxide metal interface.^[76, 77] From the data corresponding to Fig.3.20, this depth was found to be around 5.8 nm. This value for the oxide layer thickness is not completely accurate because the depth calibration is based on the average sputtering rate in the bulk aluminum and this is usually different from the sputtering rate in the oxide.

The total counts for the SIMS measurements vary from sample to sample. Hence for comparison of profiles for samples treated for different amounts of time in the NaOD solution, the counts for the different D-containing species were normalized against the counts

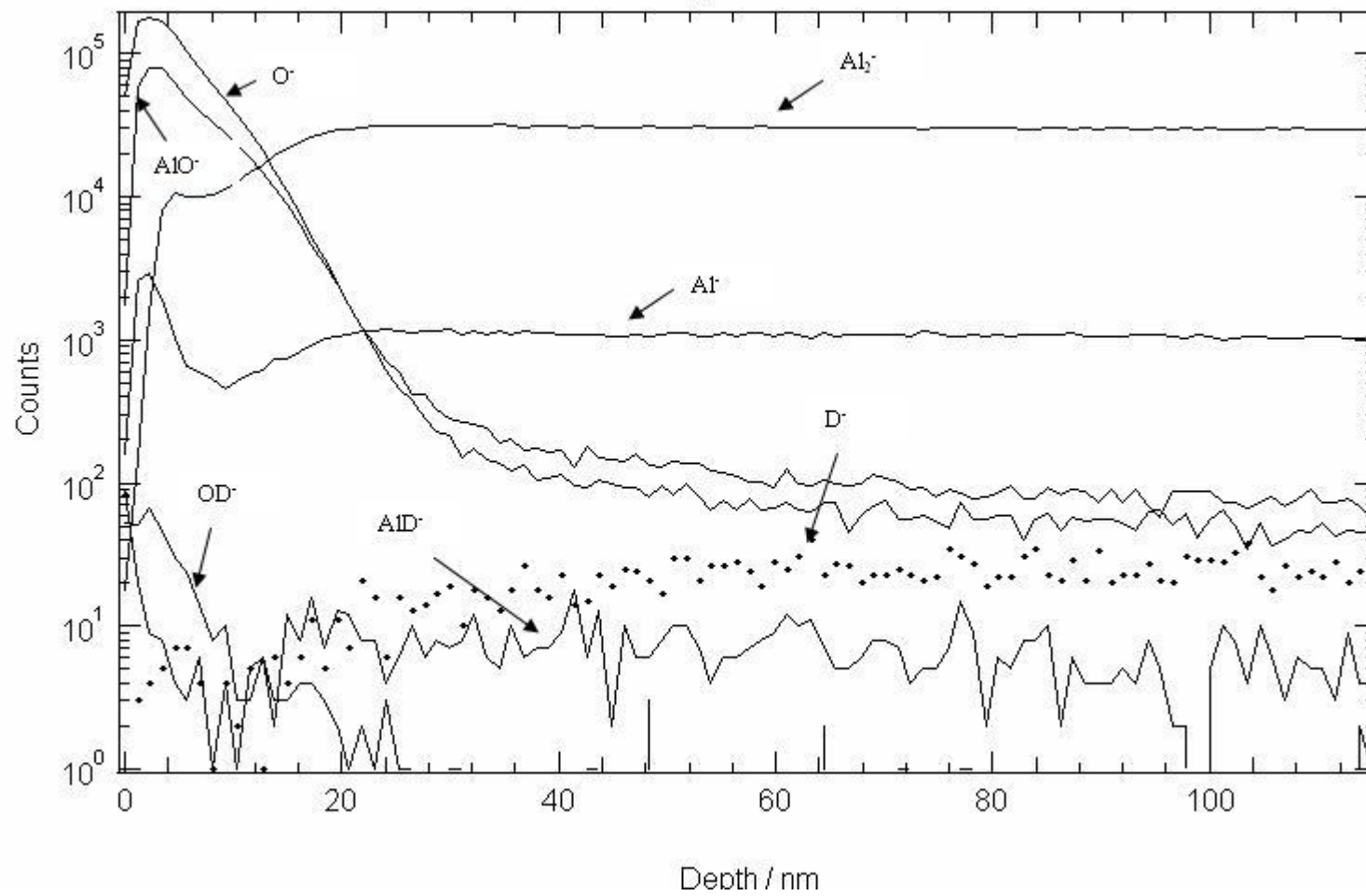


Fig. 3.20 SIMS profiles of as-electropolished 4N Al foil.

for the bulk value of the Al_2^- counts, since it was the most dominant signal in the metal in each sample. Absolute concentrations of the species observed in SIMS can also be calculated using sensitivity factors for the secondary ions but that was not attempted in this work since the comparison of concentrations of different D^- containing species with each other was not necessary. The D^- profiles for 0, 10, 12, 13 and 14.5 min treatment in NaOD are shown in Fig. 3.21 below. It can be seen that the D^- profiles for all the treatment times are almost the same, including the as-electropolished foil which was not exposed to any D. Thus, we can conclude that the profiles for the D^- secondary ions are all due to background contamination rather than the dissolution in NaOD. Normalized profiles for AlD^- and OD^- for the same dissolution times are shown in Fig. 3.22 and Fig. 3.23 respectively. We can see that the normalized counts for both AlD^- and OD^- in the as-electropolished foil are still very low but the counts are much higher for some of the treated foils (12 and 14.5 min for AlD^- and all treatment times for OD^-). Thus, there definitely seems to be a strong but non-monotonic dependence of the profiles of these 2 species on the alkaline dissolution time. The AlD^- counts, for example, are low for 10 min, rise at 12 min, again decrease at 13 min, and then increase again at 14.5 min. Also, the AlD^- counts for the 12 and 14.5 min samples are low very close to the surface, rise to a maximum at a depth of about 10-20 nm and then decrease slowly to low background values around 60 nm. The OD^- profiles on the other hand have a maximum very close to the surface at a depth of around 2-4 nm.

In order to study the dependence of the concentrations of AlD^- and OD^- species on the dissolution time, a large number of SIMS measurements were done with NaOD treatment times in the range of 0 – 20 min. The total AlD^- and OD^- contents were calculated by

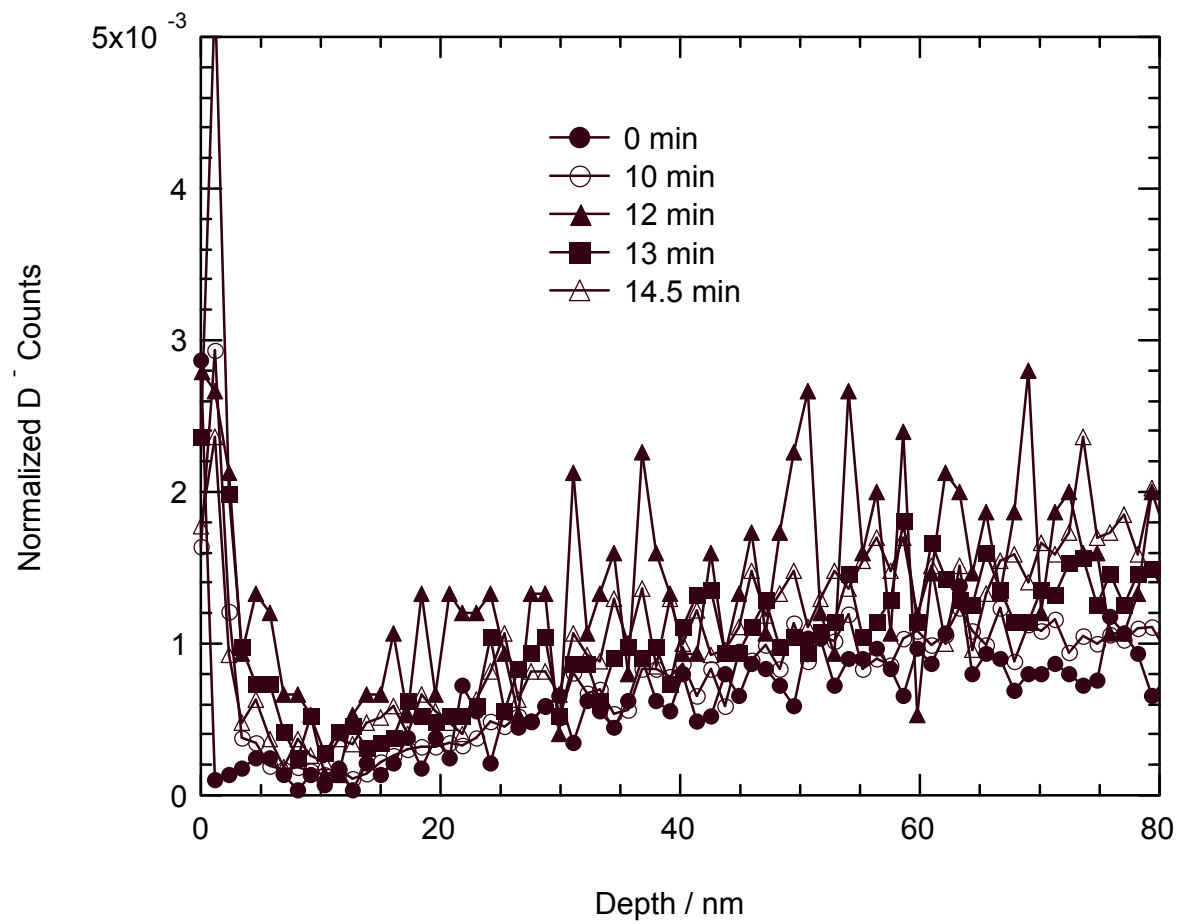


Fig 3.21 D^- depth profiles after alkaline dissolution of 4N Al foil normalized with respect to bulk Al_2^- counts.

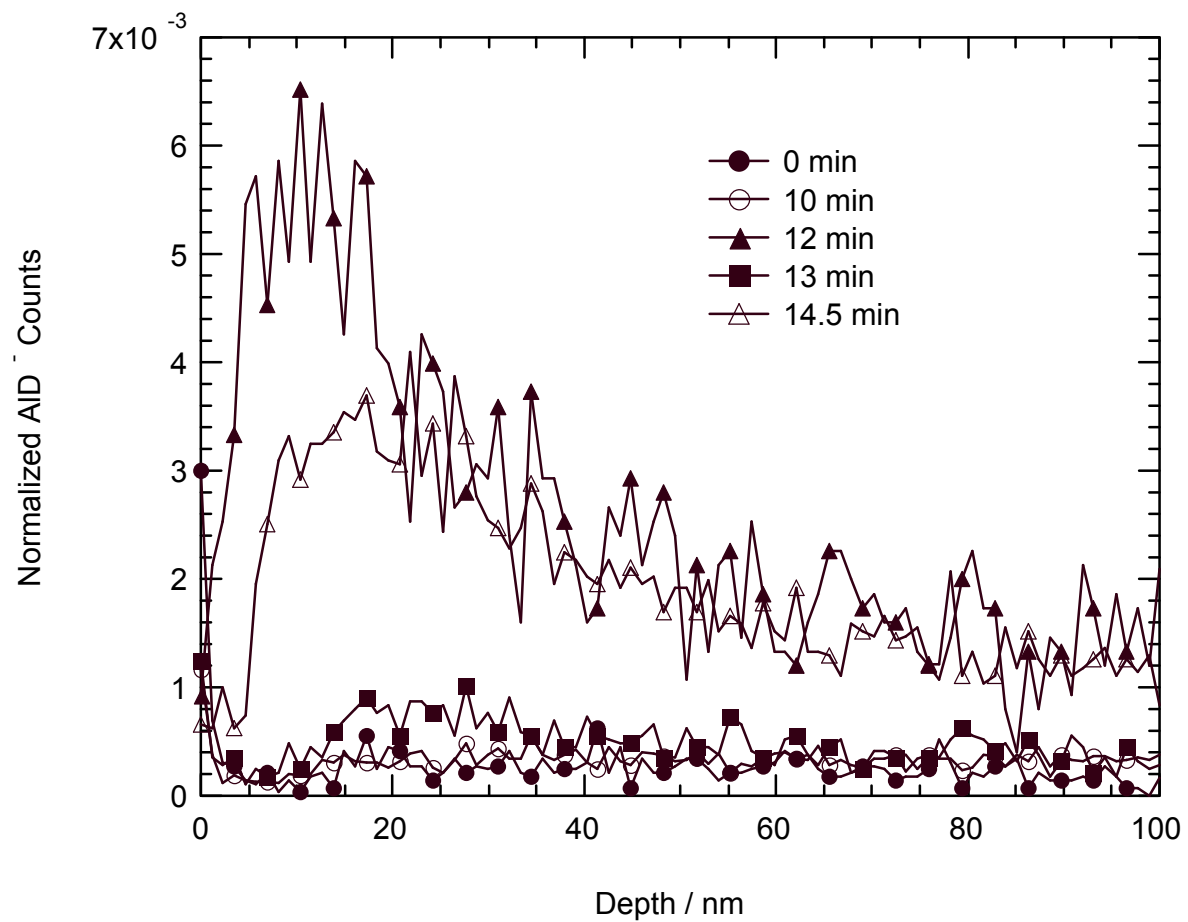


Fig. 3.22 AlD^- depth profiles after alkaline dissolution of 4N Al foil normalized with respect to bulk Al_2^- counts.

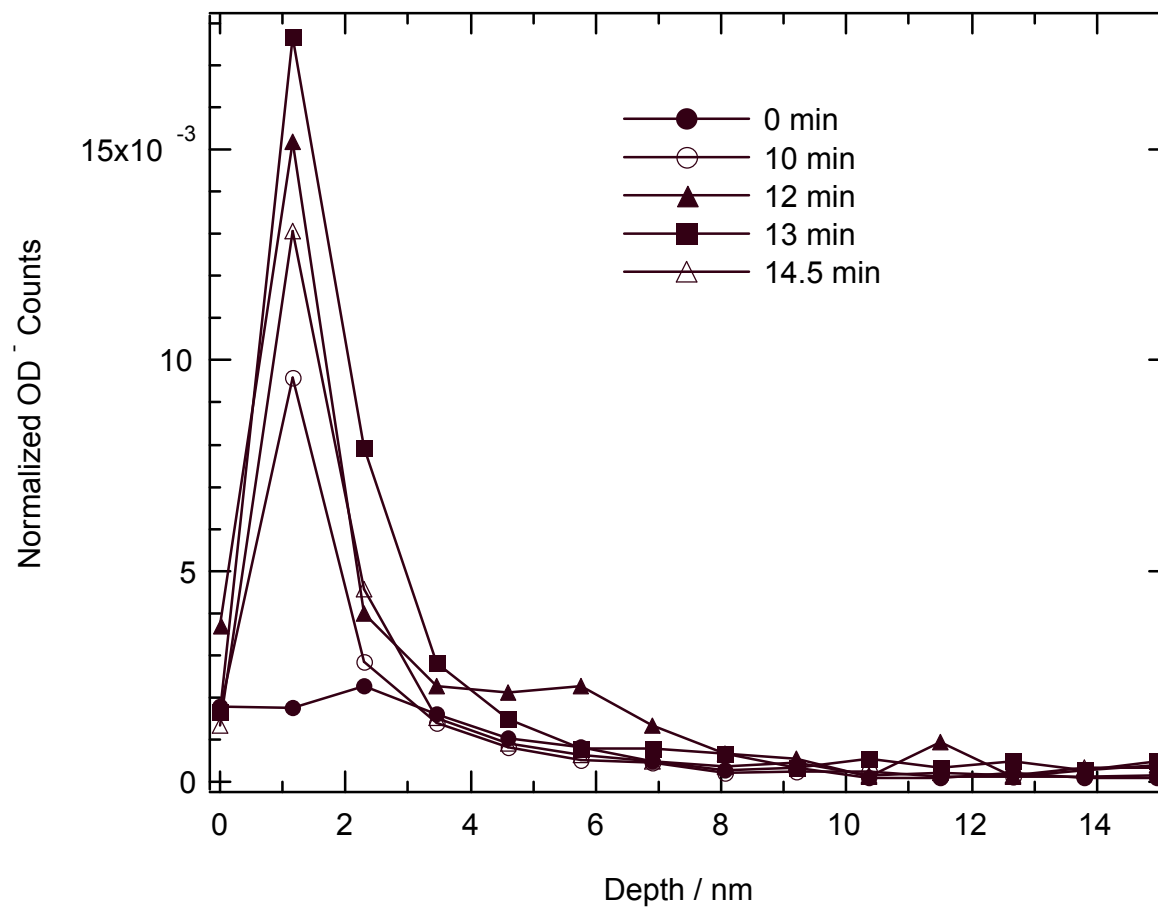


Fig 3.23 OD⁻ depth profiles after alkaline dissolution of 4N Al normalized with respect to bulk Al₂⁻ counts.

integrating the respective profiles as seen in Fig. 3.22 and Fig. 3.23 up to depths of 60 nm and 10 nm respectively after subtracting the average background signal seen after these depths. The profiles thicknesses were also estimated from the profiles in Fig. 3.22 and Fig. 3.23 as the depths at which the normalized counts go down to $1/e$ (36.8%) times the maximum values. Fig. 3.24 and 3.25 below show the integrated profiles and the profile thicknesses for the AlD^- and OD^- species. The open symbols are average values of two data points at the same dissolution time. The normalized counts and the profile thicknesses for data points at which the integrated areas for AlD^- and OD^- did not exceed 0.001 were set as zero since they were probably due to background noise. Fig. 3.24 shows that AlD^- integrated areas and profile thickness increase and decrease together in almost uniformly distributed time periods. There AlD^- signal maxima at 1, 4, 7-8, 12 and 15 min. In between these “bursts” of AlD^- signal, there are periods of ~1-2 min where the signal is extremely low and hence attributed to background noise. The time duration of each of these bursts was about 2 min, during which the AlD^- profiles looked similar to those shown for 12 and 14.5 min dissolution times in Fig. 3.22. Profiles for OD^- in Fig. 3.25 show that the OD^- integrated areas and depths again show similar bursts as shown by the AlD^- up to about 7-8 min, after which it is detected for all the treatment times (except for the time of 14 min which might be an experimental artifact) indicating the onset of accumulation of OD^- on the surface. The burst seen for OD^- are at the same NaOD treatment times as those of AlD^- i.e. at 1, 4 and 8 min.

The aluminum foil is continuously dissolving during the alkaline treatment process. Hence, the bursts of AlD^- and OD^- detected by SIMS could be related to repeated nucleation and dissolution events of a new phase on the surface. A rotating disk electrode study of the

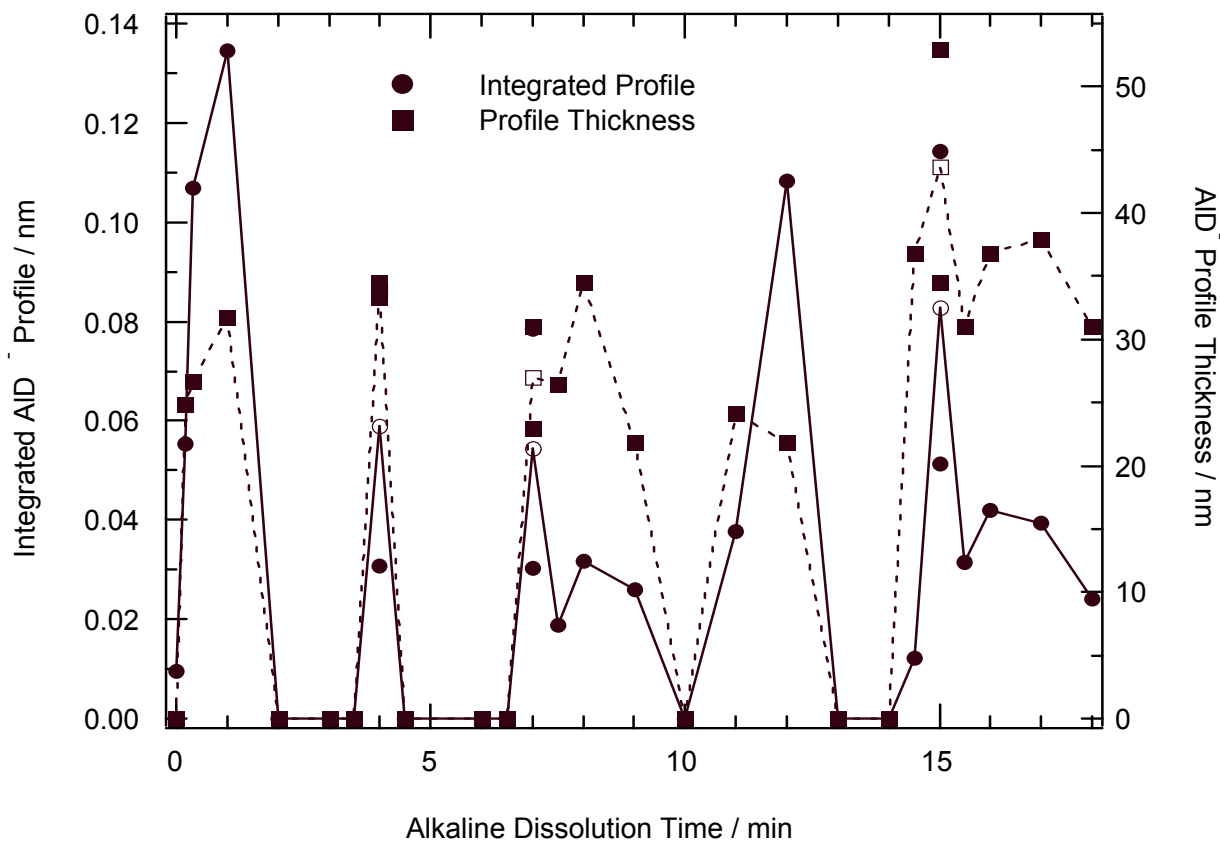


Fig. 3.24 Integrated AID⁻ depth profiles and profile thicknesses, after alkaline dissolution of 4N Al samples. The profile thickness is defined as the depth at which the normalized AID⁻ counts are a fraction 1/e (i. e., 0.368) of the profile maximum. Open symbols are averages of two data points at the same time.

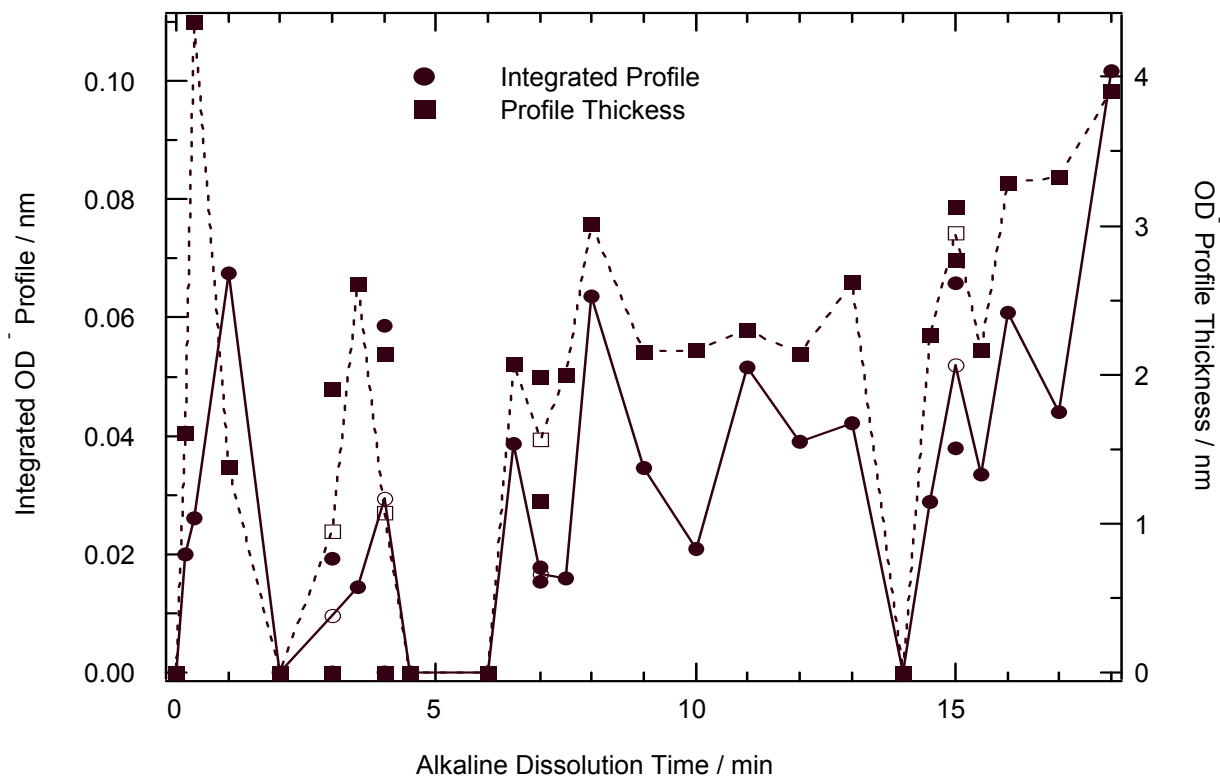


Fig. 3.25 Integrated OD⁻ depth profiles and profile thicknesses, after alkaline dissolution of 4N Al samples. The profile thickness is defined as the depth at which the normalized AID⁻ counts are a fraction 1/e (i. e., 0.368) of the profile maximum. Open symbols are averages of two data points at the same time.

alkaline dissolution of aluminum has found evidence for the presence of a hydroxide film on the surface.^[17] Hence the surface species nucleating could be aluminum deuterioxide. SIMS OD^- peaks originating from passive films on aluminum containing deuteroyl groups have been reported.^[77] But no AlD^- and D^- peaks from SIMS were found in these studies. Interestingly, cationic peaks of AlH^+ , AlH_2^+ , AlH_3^+ have been detected in high purity aluminum single crystal surfaces exposed to hydrogen in high vacuum studies.^[55-60] These cations are supposed to have originated from aluminum hydride species (AlH_3 , Al_2H_6) formed by the chemical reaction of hydrogen with aluminum. In order to identify the AlD^- , OD^- and D^- species and especially for finding evidence of the formation of a new phase during the alkaline dissolution process, AFM imaging of the aluminum samples was conducted at treatment times corresponding to the SIMS measurements.

3.3.2 AFM study of aluminum dissolution in alkaline solutions

The samples for the AFM imaging were 4N electropolished foils treated for various times between 0 – 10 min in 1M NaOH (H_2O) solutions. AFM images for NaOH dissolution times of 40s, 1, 2 and 3 min are shown in Fig. 3.26 below. The typical ridge-scallop topography of electropolished and alkaline treated aluminum is clearly seen in all samples with larger scallop sizes in the treated samples. On top of those, we see numerous round particles which seem to have diameters of less than 100 nm. These particles are not present at 40s, but can be clearly seen in the 1min treated sample. They seem to be less numerous but larger at 2 min and then there is a significant drop in the number density and size of these objects in the 3 min sample. The same white circular features as well as the scallops and

ridges are seen more clearly in the FE-SEM image shown in Fig. 3.27 below. The sample in the SEM image was a 4N electropolished foil treated for 4 min in NaOH cleaned with 1M HNO₃ before the imaging. The size of the SEM image is 2.5 x 1.7 μm while the AFM images were all 5 x 5 μm. From the AFM images it is evident that these particles are formed between 40 s and 1 min, grow in size between 1-2 min and then dissolve between 2-3 min. Interestingly, these events correspond to the AID⁻ and OD⁻ bursts seen in the SIMS measurements with maxima for both the species at 1 min. In order to quantitatively characterize the times of nucleation, growth and removal by dissolution of these particles, number density and size distributions of these particles in the same time range as that of the SIMS measurements were examined. At each dissolution time, 2-3 images from different experiments were analyzed. Each image was 5 x 5 μm in size. The particle number densities were calculated by normalizing with the total image area of 25 μm². The particle radii were calculated as $\sqrt{(Particle_Area)/\pi}$. The number density-size distributions are shown in Fig. 3.28 below. As is clearly seen, there is a significant increase in the particle number densities at 1 min and 8 min in comparison with 0 and 7 min (0 min is not shown here because it was the as-electropolished sample and did not show any of these particles). The number densities are slightly higher at 4 min as compared to that at 3 min suggesting that there might have been another significant increase of the particle numbers between 3-4 min. The particles are larger but fewer at 2 and 9 min as compared to those at 1 and 8 min indicating growth and coalescence of the particles at these times after their nucleation as seen in Fig. 3.26. In all cases the particles were mostly smaller than 50 nm when they first nucleated. The particles

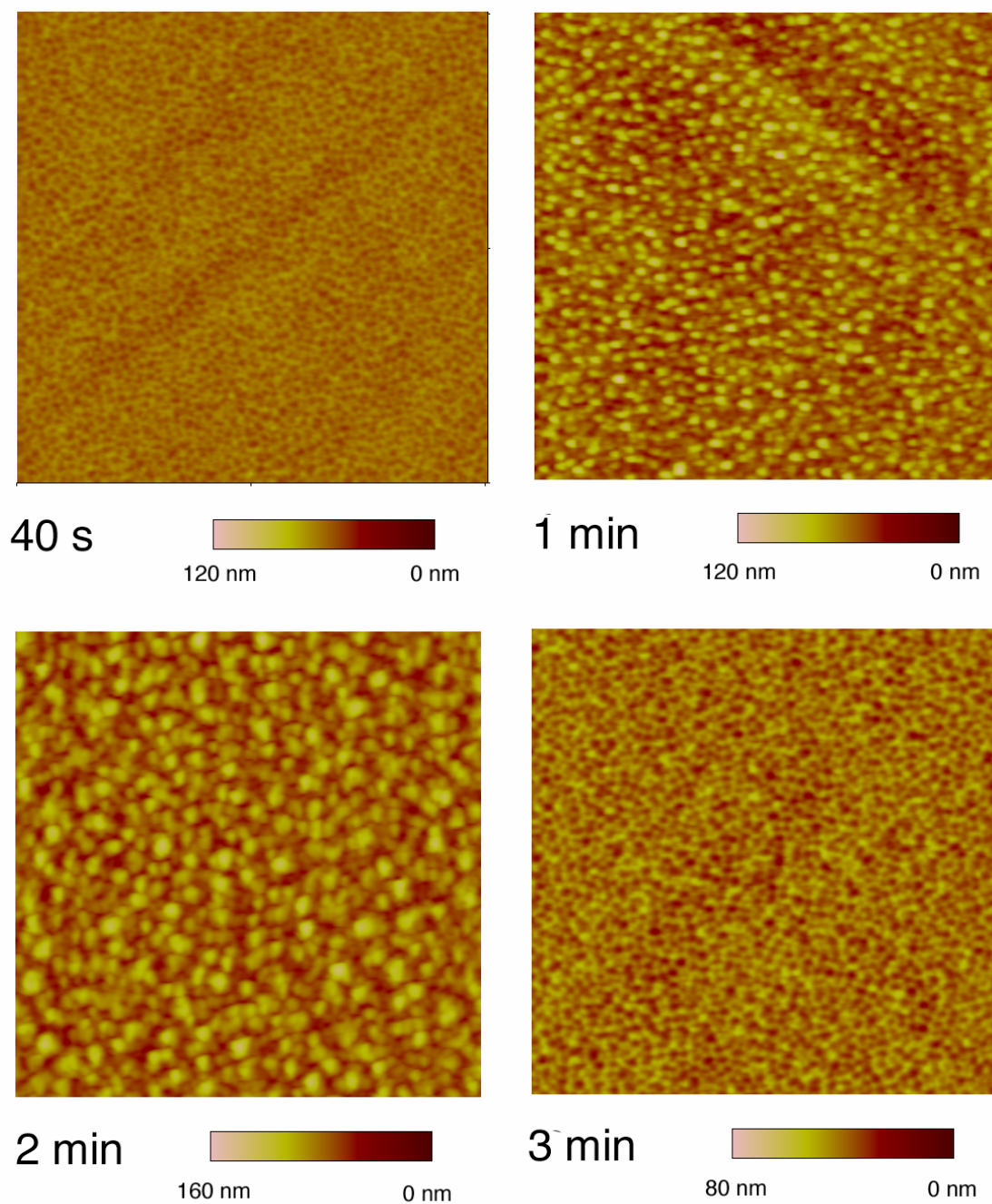


Fig. 3.26 AFM images of Al surface topography after alkaline dissolution. $5 \times 5 \mu\text{m}$ top view images after 40 s, 1, 2 and 3 min dissolution, respectively. Conversion of color scale to height is indicated below each image.

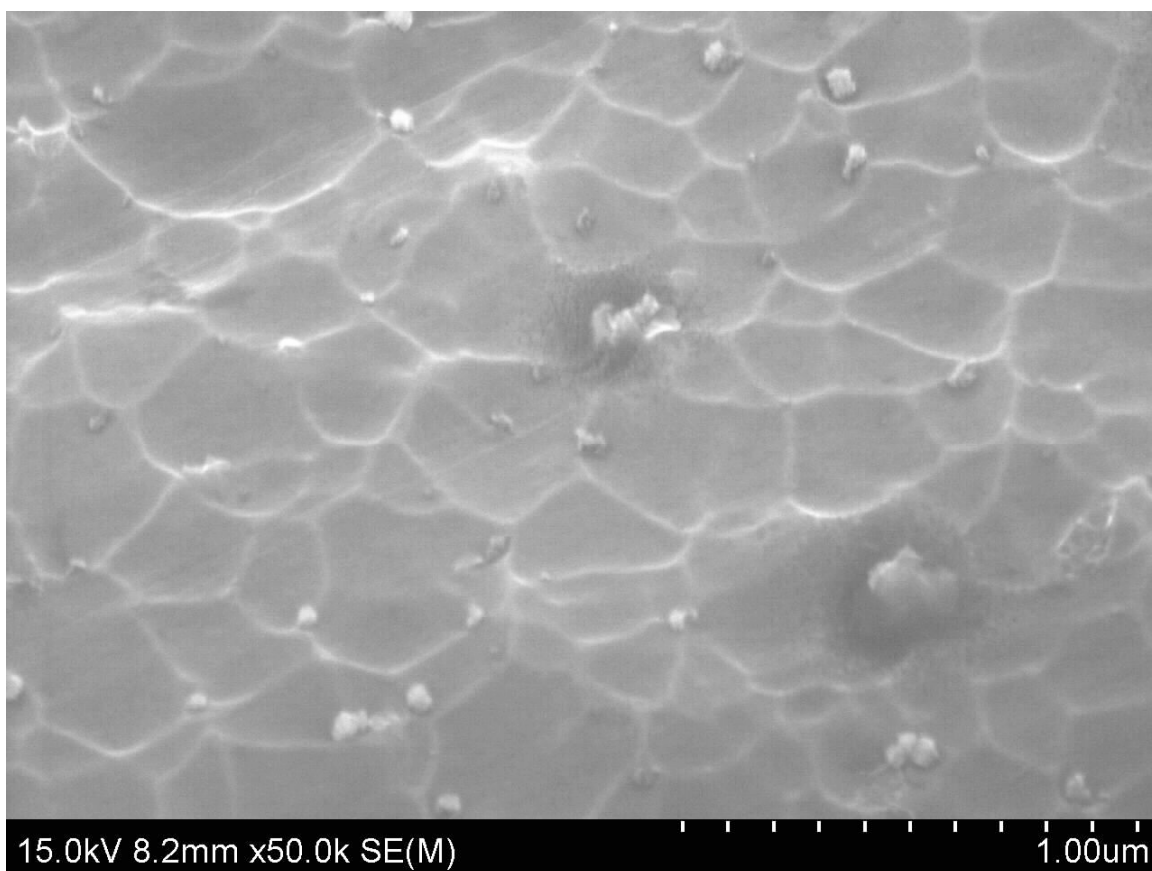


Fig. 3.27 FE-SEM image of Al surface after 4 min alkaline dissolution (image dimensions are $2.5 \times 1.7 \mu\text{m}$). The sample was dipped in 1 M HNO_3 solution after alkaline treatment.

numbers were significantly diminished at 3 and 10 min dissolution times possibly due to removal by dissolution. All these nucleation times roughly coincide with the times of the AID^- burst seen in SIMS. Also, the time between the nucleation of these particles and their removal is around 2 min. Thus, the timing as well as the duration of these precipitation events are consistent with the AID^- and OD^- bursts observed with SIMS. Fig. 3.29 below shows the particle height and particle radii for dissolution times between 5-8 min. Clearly, the particles heights are all between 5-20 nm at 5, 6 and 7 min but increase to about 40 nm at 8 min, just like the increase in the AID^- and OD^- signal at around 8 min detected by SIMS.

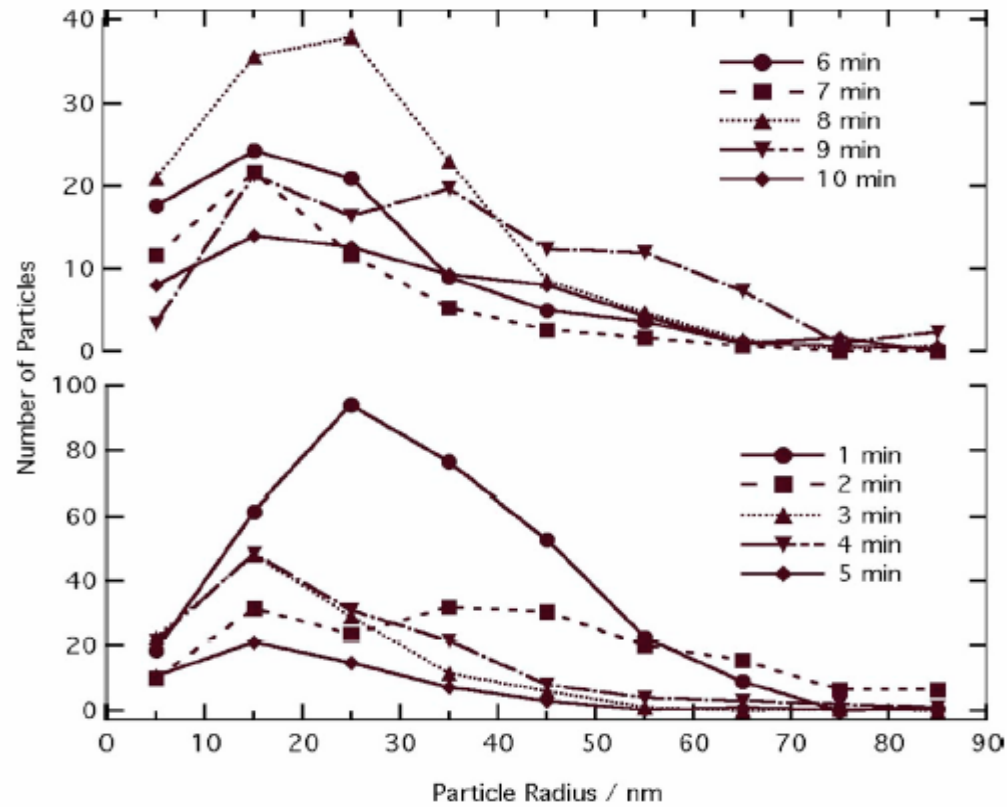


Fig. 3.28 Particle size distributions at various NaOH dissolution times, obtained by analysis of AFM images. Particle radius is defined according to $\sqrt{(Particle_Area)/\pi}$. Number of particles in each size category is referenced to an Al surface area of $25 \mu\text{m}^2$.

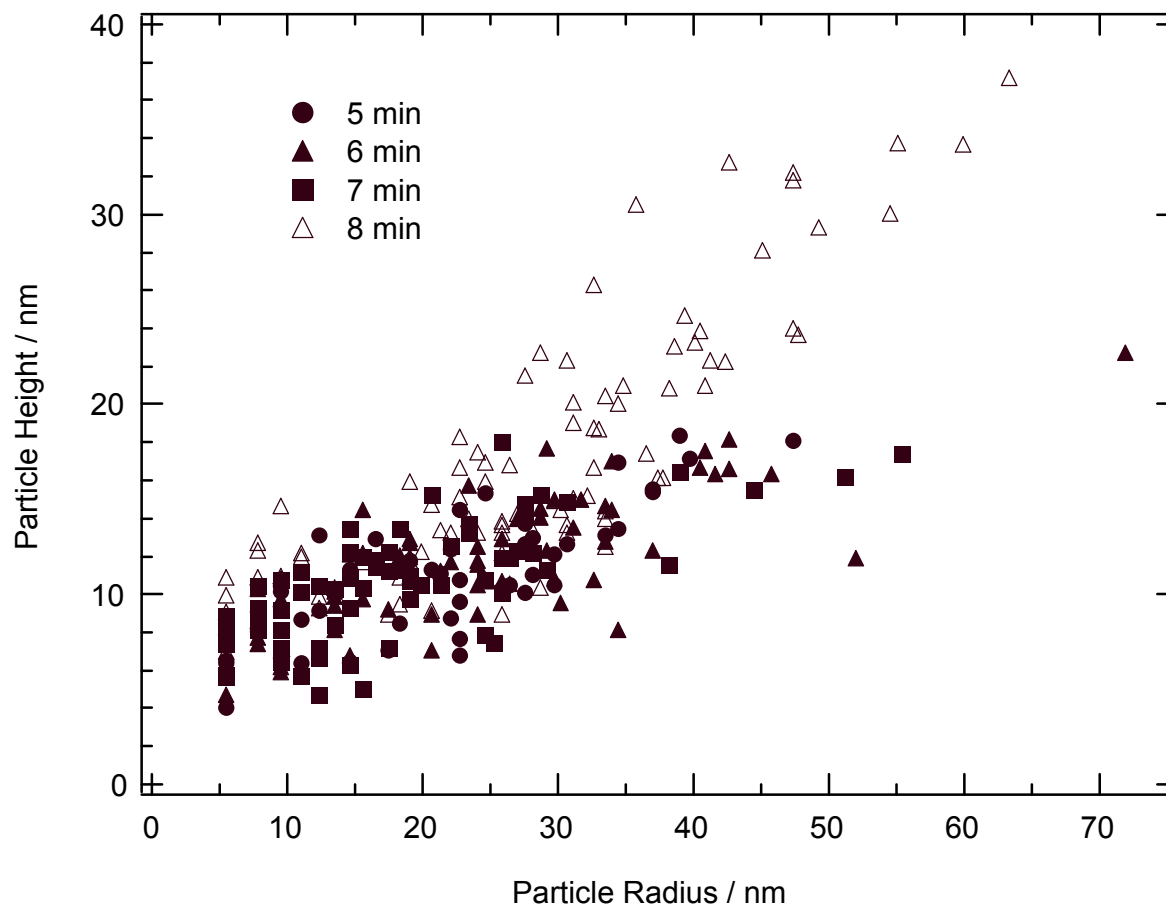


Fig. 3.29 Heights and radii of individual particles, measured by AFM after dissolution times of 5-8 min.

3.3.3 Implications of the SIMS and AFM observations

The only source of deuterium in the samples observed in SIMS was the NaOD (in D₂O) treatment procedure. The correspondence between the nucleation/dissolution of the large particles seen in AFM and the AlD⁻/OD⁻ bursts seen in SIMS suggests that these particles were formed during the alkaline dissolution process itself. Also, there is a very good agreement between the thickness of the AlD⁻ profiles and the height of the particles seen in AFM. For instance, both the SIMS profile thickness and the heights of the largest particles at 8 min dissolution time as seen from Fig. 3.24 and Fig. 3.29 respectively are around 30-35 nm. The presence of the smaller particles seen in the AFM images at all dissolution could be an artifact of the experimental procedure. The sample just after removal from the alkaline bath has a layer of the alkaline solution on the metal surface containing aluminate ions (Al(OH)₄⁻) formed by the metal dissolution process. The deionized water that was used for washing the samples after the NaOH treatment so as to stop the dissolution reaction was almost neutral in pH (~ pH 7.5). This could have led to the precipitation of these small particles from the Al(OH)₄⁻ ions as aluminum hydroxide (Al(OH)₃). Since the sputtering rate was calculated only for the bulk metal, these comparisons cannot be made very precisely as the sputtering rate in the particles would be different from that in bulk aluminum.

As mentioned earlier, the OD⁻ secondary ions have been reported earlier.^[77] These were found to have originated from passive films on aluminum containing deuteroyl groups. AlD⁻, on the other hand has not been reported prior to this in literature. Aluminum hydride species have been detected as AlH⁺, AlH₂⁺, AlH₃⁺ by exposing high purity aluminum single crystal surfaces to hydrogen.^[55-60] Due to the striking similarity in the timing of the AlD⁻

bursts with the nucleation, duration and removal of the particles, and the correspondence between the AlD^- profile thicknesses and the particle heights at all times, these particles are more likely to be aluminum deuteride surface species and not deuteroyl species. The OD-peak seen which is only a few nanometers could be a surface overlayer on the aluminum deuteride particles, formed by the oxidation of the particles in solution or later in air after removal from the NaOD bath. The formation of Al(OD)_3 from oxidation of AlD_3 is also suggested by the fact that depth profiles of AlD^- and OD^- do not overlap appreciably as seen in Fig. 3.22 and Fig. 3.23 respectively. The stability of aluminum hydride (AlH_3) particles has, in the past, been attributed to the presence of surface oxide films, which acts as a kinetic barrier to decomposition and protects the AlH_3 from the environment.^[78] All this evidence led us to the conclusion that the particles created by the NaOH/ H_2O dissolution process are primarily composed of an aluminum hydride corrosion product with a surface layer of Al(OH)_3 (and AlD_3 covered in Al(OD)_3 in SIMS).

Further support for the assignment of these particles to AlH_3 can be found from Auger Electron Spectroscopy measurements by Martin and Hebert.^[34] Auger spectra were measured from the particles formed on a 99.99% aluminum foil treated in 1M NaOH (in H_2O) before and after sputtering up to depths of 5 and 10 nm. These spectra for the particles were compared with the AES spectra at locations where no particles were present. The O : Al atomic ratio from the spectra at the particles and places away from the particles before sputtering were found to be 1.72 and 1.76 respectively. Thus oxide or hydroxide layers of several nanometers thickness were detected on the surface (O : Al ratio should be 1.5 for an anhydrous aluminum oxide). On the other hand, after sputtering up to 10 nm, the ratio of

oxygen to aluminum was much lower and the same (~ 0.33) for particles and locations away from the particles. This suggested that the particles only had a hydroxide surface layer which was less than 10 nm thick (the oxide layer was ~ 3 nm thick on the aluminum). Thus, the interior of the particles were considered to be metallic aluminum. However, since hydrogen is not detected by AES, the particles could also be explained as AlH_3 covered with a surface oxide layer. The aluminum hydride could easily be decomposed by the electron beam into metallic aluminum.^[79]

Electrochemical experiments by Perrault give more evidence of the involvement of AlH_3 in dissolution of aluminum.^[25] He found that the pH dependence of the open-circuit potential of cathodically charged pure aluminum was quantitatively consistent with equilibria of reactions involving AlH_3 in alkaline solutions and AlH^{2+} in neutral and acidic solutions. He found that the open-circuit potential in strongly alkaline media was determined by the equilibrium of the reaction



He obtained a standard chemical potential of 25 kcal/mol for AlH_3 from his data, which was in reasonable agreement with prior thermochemical calculations done by Sinke et al who obtained a value of 11.1 kcal/mol for the chemical potential.^[80] The corresponding Nernst potentials of reaction 3.1 at pH 14.0 for the 2 chemical potential values are -1.95 and -1.85 vs. the Ag/AgCl reference electrode. Both these values are very close to the measured open circuit potential during the dissolution in the first 10 min in the current experiments (i.e. 4N electropolished foil dissolving in 1M NaOH solution) as seen in Fig. 3.30 below. On the

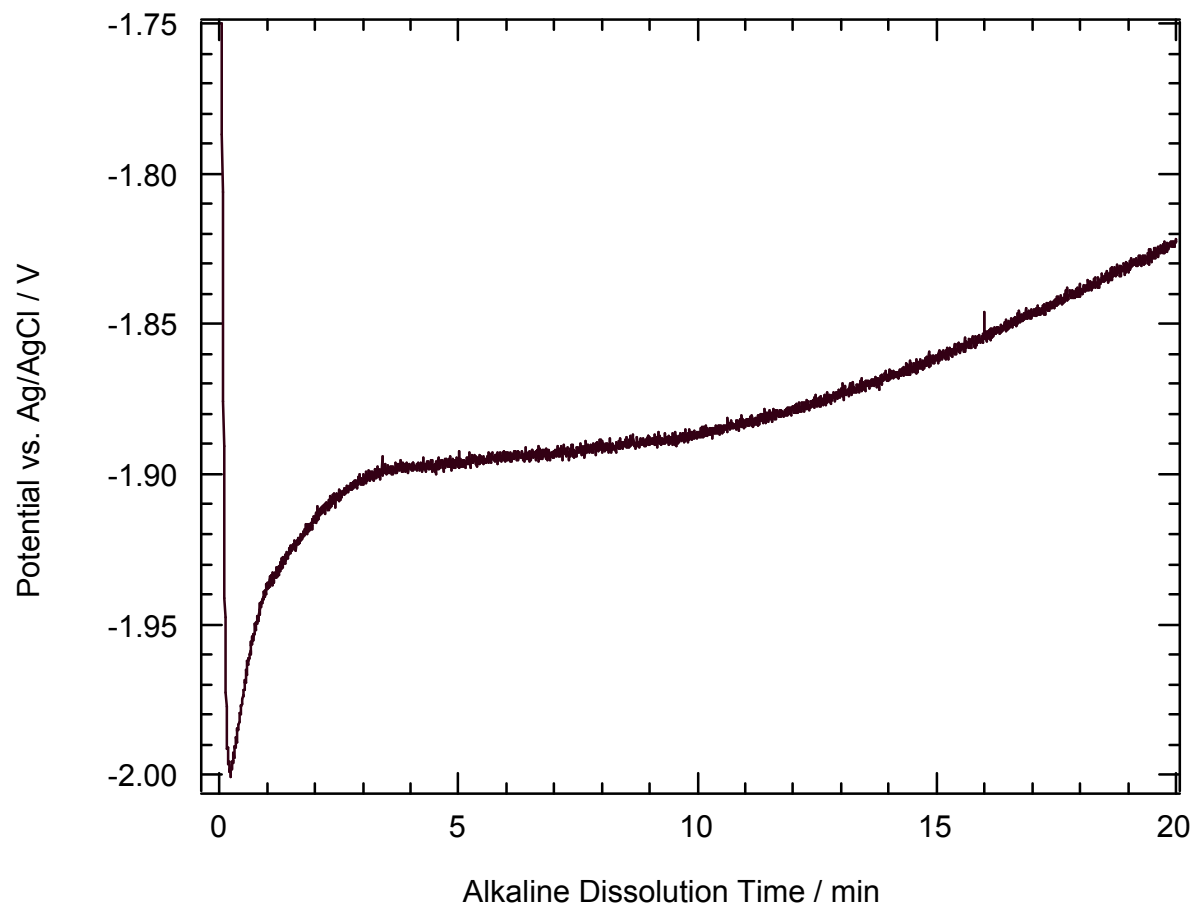


Fig. 3.30 Open circuit potential during dissolution of the 4N electropolished foil in 1 M NaOH (H₂O).

other hand, the Nernst potential for direct Al dissolution at pH 14.0 is -2.56 V vs. Ag/AgCl.^[1] Further evidence of hydride was given by Despic et. al. and Radiosevic et. al.^[5, 27] They found that aluminum hydride formation was one of the major processes apart from aluminum dissolution and hydrogen evolution, during the cathodic polarization of aluminum.

Based on the observation that aluminum hydride is present on the surface during the dissolution process, we propose a reaction mechanism for the open circuit alkaline dissolution of aluminum. The anodic reaction 3.7 is accompanied by the cathodic reduction of water to form hydrogen



and the reaction of hydrogen with aluminum to form hydride



Reaction 3.9 represents the H-induced etching of aluminum as has been extensively observed in vacuum experiments^[55-60] The overall dissolution reaction obtained by balancing the electrons in the cathodic and anodic reactions is hence



The overall reaction thus dictates that both aluminum hydride and aluminate ions are continuously formed as products of the alkaline dissolution process. The AlH_3 is also subject to chemical dissolution by reaction with water.

Let us now consider this reaction pathway involving hydride as opposed to earlier mechanisms which propose precipitation of hydroxide films during dissolution of aluminum. The rate of dissolution of the aluminum samples used in this work in 1M NaOH measured over extended periods of time (in order to obtain measurable changes in the foil thickness)

was found to be $\sim 2\text{nm/s}$. The concentration of $\text{Al}(\text{OH})_4^-$ near the aluminum surface is expected to increase with time until the solubility of $\text{Al}(\text{OH})_3$ is reached. This time required for hydroxide precipitation, t_p , can be calculated using Sand's equation as

$$t_p = \pi D \left(\frac{C_s \Omega_{Al}}{v_d} \right) \quad (3.11)$$

where D is the diffusion coefficient of $\text{Al}(\text{OH})_4^-$ ions, C_s is the concentration of $\text{Al}(\text{OH})_4^-$ ions at the metal surface when precipitation occurs, Ω_{Al} is the molar volume of aluminum ($10\text{ cm}^3/\text{mol}$), and v_d is the dissolution velocity (2 nm/s).^[81] The diffusion coefficient of $\text{Al}(\text{OH})_4^-$ was reported to be $8.4 \times 10^{-6}\text{ cm}^2/\text{s}$.² C_s was taken as 0.05 M , the solubility of gibbsite, the least soluble form of $\text{Al}(\text{OH})_3$ and normally the first precipitate from aqueous solution.^[82, 83] This value represents the minimum time at which precipitation can occur since usually supersaturation is needed for nucleation to occur. Substituting these values in Eqn. 3.11, t_p is found to be about 165s . This time is greater than the time when the particles first appear ($\sim 1\text{ min}$) but less than the time when accumulation of $\text{Al}(\text{OH})_3$ was seen ($\sim 7\text{ min}$) in the SIMS measurements as seen in Fig. 3.24 and Fig. 3.25 respectively. Although these calculations might be off slightly since the dissolution rate of aluminum during early times might be different from the average measured value of 2nm/s , this further supports the association of the particles to AlH_3 rather than $\text{Al}(\text{OH})_3$. The bursts of AID are not accompanied by similar bursts in the open-circuit potential transient (Fig. 3.30). Hence, these bursts are in most likelihood, driven by oscillations of concentrations near the metal surface.

Prior SIMS studies of alkaline treated or cathodically charged aluminum have revealed deuterium or hydrogen profiles in the metal as D^- or H^- secondary ions.^[53, 54] For

instance, Rozenak et. al. detected D^- profiles up to depths of about 1 μm in aluminum samples treated in 1M NaOD (D_2O) for 2 hrs.^[53] The absence of significant D^- profiles in our SIMS measurements can be explained by considering the D^- species as a mobile form of deuterium in aluminum which diffuses into the metal after the alkaline treatment procedure. The penetration depth of diffusing deuterium increases with time as $\delta_D \sim (D_{Dt})^{1/2}$, where D_D is the interstitial deuterium diffusivity. Since the samples in our experiments were treated in the NaOD bath for <20 min and the transfer time between the treatment and the actual measurements was in between 50-150 min, the near surface D absorbed during the dissolution process would have diffused into the bulk metal. If the transfer times were comparable to treatment times as in the case of the experiments done by Rozenak et. al., the mobile D profiles might not have been eliminated.

The SIMS and AFM observations reported here is thus the first analytical detection of aluminum hydride formed during the dissolution of aluminum. The proposed reaction mechanism based on these observations indicates the continuous formation and oxidation of hydride near the Nernst potential of the oxidation reaction. The electrochemical behavior of anodic dissolution of aluminum was hence investigated to draw support for the participation of AlH_3 as a reaction intermediate. This will be the focus of discussion in the next chapter.

3.4 Electrochemical behavior of anodic aluminum dissolution in alkaline solutions

In this chapter, cyclic voltammetry and potential step measurements during the anodic dissolution process will be discussed and a theoretical model based on the proposed mechanism will be developed. This study seeks to identify the potential at the interface of the metal and the surface film and to determine whether it corresponds to the Nernst potential for oxidation of aluminum hydride. Confirmation of this proposal would indicate that the metal is covered by an AlH_3 layer, through which dissolution proceeds.

3.4.1 Cyclic voltammetry studies of aluminum dissolution in alkaline solutions

As mentioned earlier in the experimental section, for the cyclic voltammetry experiments, the 4N electropolished foil was used after a pretreatment in 1M NaOH for 1 min. The solution used for the CV experiment was 0.1M Na_2SO_4 in nanopure water adjusted to a pH value of 11.00 or 11.75 by adding NaOH crystals. The reasons for choosing these 2 pH values for the CV experiments are several:

- (1) In this pH range, the currents due to cathodic reactions are not very large above the open circuit potential. Hence it is easier to measure and interpret the currents in terms of anodic reactions.
- (2) Within this pH range, the open-circuit potential is close to the Nernst potential of hydride oxidation as shown in Eqn. 3.7. Thus, the presence of surface hydride species is conceivable in this pH range.^[25]
- (3) This pH range represents the transition of rapid corrosive behavior of aluminum in alkaline solutions to the passive behavior in neutral solutions.^[1] Thus, these 2 pH values

enable us to determine whether the aluminum electrode dissolves through the aluminum hydride mechanism in these two regimes.

Fig. 3.31 below shows the first cycle CV scans for the aluminum foil (pretreated for 1min 1M NaOH) in aerated pH 11.75 sodium sulfate solution for scan rates of 0.5, 1, 2 and 4 mV/s. The scans constitute the forward and the reverse sweep between -1.8 and -1.4 V (vs. Ag/AgCl reference electrode). De-aeration of the sulfate solution by nitrogen bubbling did not affect the anodic scans significantly. Each of these scans in Fig 3.31 shows an anodic current density maximum between 150 and 300 $\mu\text{A}/\text{cm}^2$ which increases with increasing scan rate. The shapes of these peaks and the scan rate dependence are both qualitatively consistent with at least partial diffusion control of the anodic reaction rate.^[81] Another experiment was conducted to illustrate the effect of diffusion on the CV scans. During the anodic scan in one of the CV experiments, the solution near the aluminum surface was suddenly stirred by sparging with nitrogen gas. As seen in Fig 3.32 below, the anodic current density increased from 160 to about 320 $\mu\text{A}/\text{cm}^2$ in a span of just 3-4 s. This clearly shows that the anodic reaction rate is mass-transfer dependent. Earlier rotating-disk studies of aluminum electrodes in alkaline solution have also reported similar diffusion controlled behavior.^[17] But it also seen in Fig. 3.31 that the anodic peak currents increase at a rate slower than one-half power of the scan rate as expected in purely diffusion controlled behavior. Also the peak potentials shift in the anodic direction with increasing scan rates. These characteristics of the CV scans suggest that in addition to the diffusion controlled behavior displayed by the anodic processes, electrode kinetics and surface film conduction also cannot be ruled out.^[81] Therefore, in order to estimate the interfacial potential, quantitative characterization of the

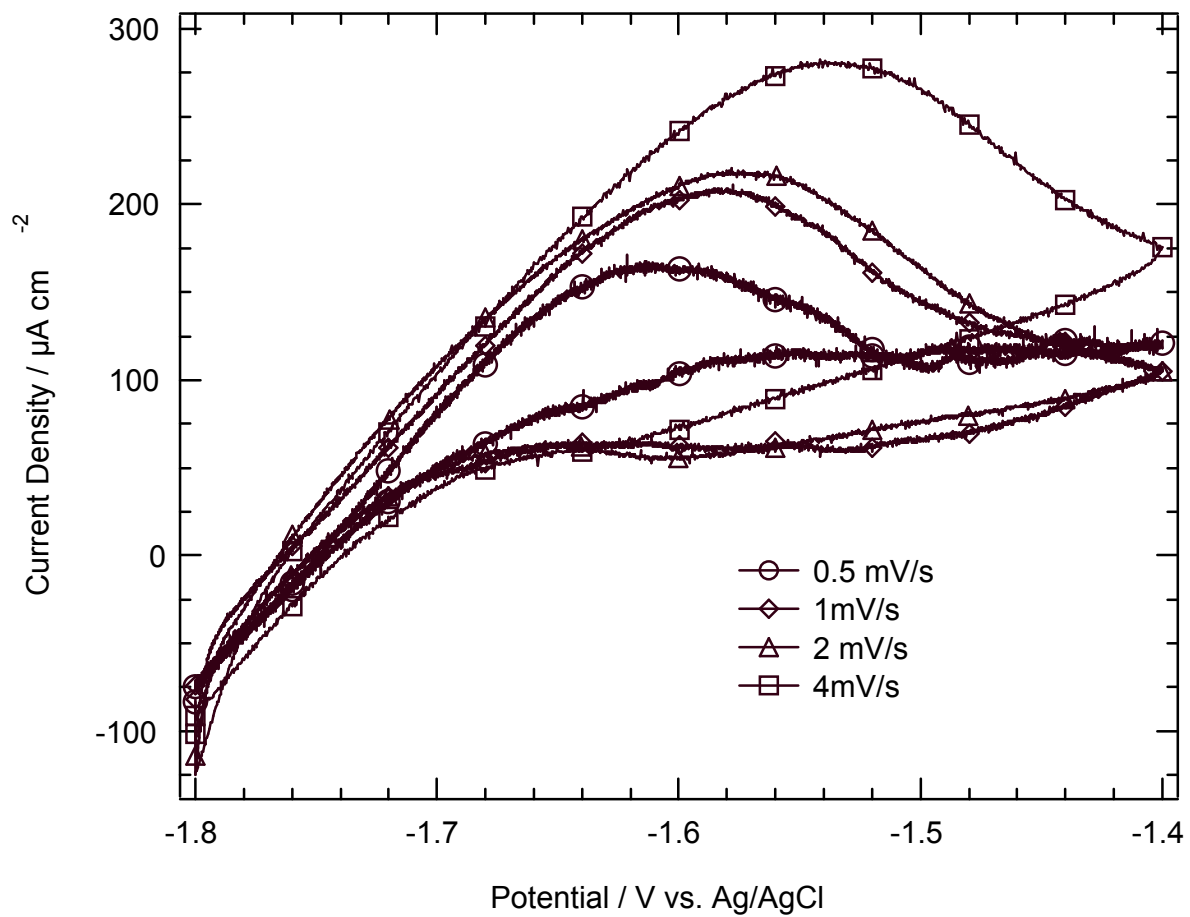


Fig. 3.31 First scan cyclic voltammetric response for 4N electropolished Al foil in 0.1 M Na₂SO₄ (pH 11.75). The foil was pretreated in 1 M NaOH for 1min prior to the CV experiment.

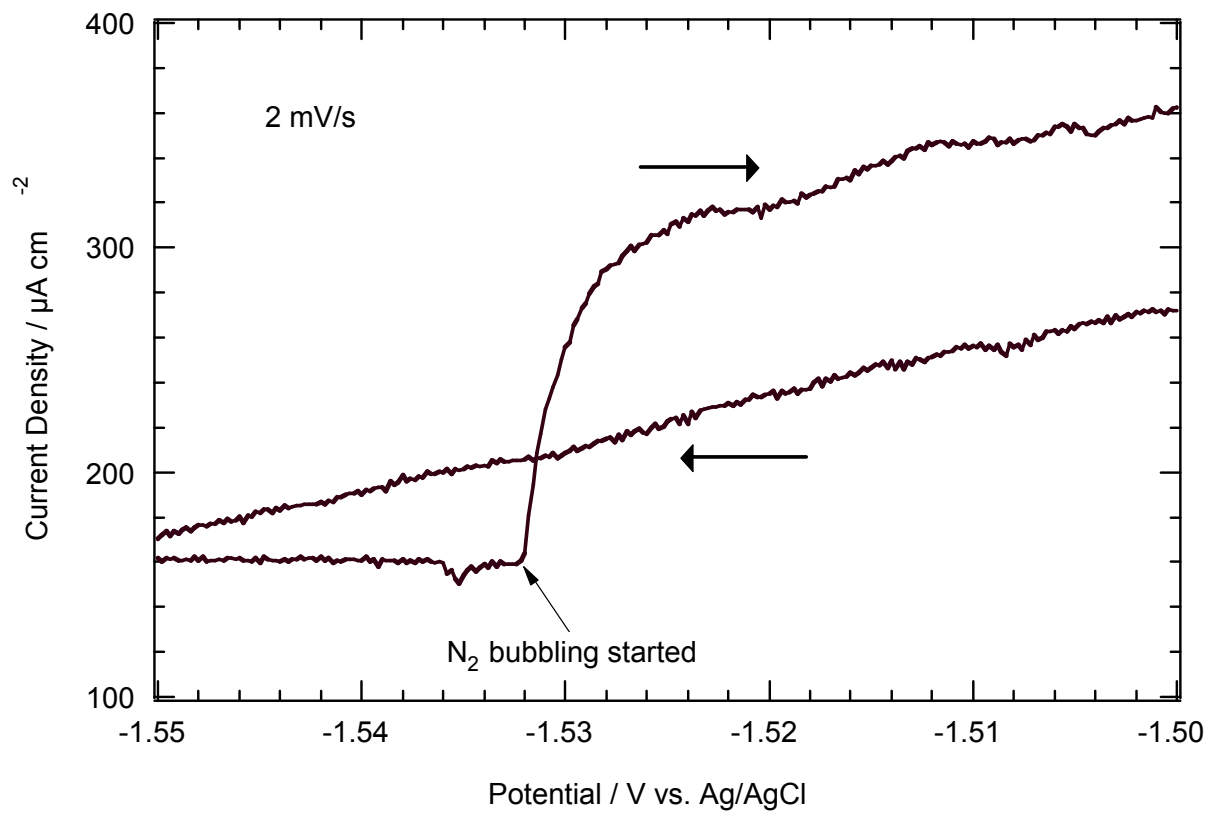


Fig. 3.32 Effect of diffusion on current measured during cyclic voltammetric scans.

kinetics and conduction was necessary. This was done with the help of potential-step experiments and will be discussed in the next section in detail.

Cyclic voltammetry results for the 4N electropolished foil in pH 11.00 Na_2SO_4 solution is shown in Fig 3.33 below. Again, as in the case of pH 11.75 solutions, the foils were pretreated for 1 min in 1M NaOH before the CV experiments. The anodic current densities in this case rise rapidly to about $90 \mu\text{A}/\text{cm}^2$ and then decay to values of 20-30 $\mu\text{A}/\text{cm}^2$. The current densities during the second (dashed lines in Fig. 3.33) and subsequent scans stay below $20 \mu\text{A}/\text{cm}^2$ in all cases. The anodic current densities in the pH 11.00 solution are much smaller than those in pH 11.75 solution. Since the open-circuit corrosion rate decreases by an order magnitude in between pH 12 and 11, this decrease in anodic currents is expected.^[1] Also, the peak current densities in the lower pH solution are independent of the scan rate. In fact, the anodic current transients and the peak current values in the pH 11.00 solution only depended on the elapsed time and were independent of the potential as shown in Fig 3.34. Thus, these transients are the result of time-dependent processes occurring after the transfer of the aluminum foil from the 1M NaOH pretreatment bath (pH 13.5) to the pH 11.00 solution. These potential-step experiments and the modeling results will help clarifying the nature of these processes.

The second and all consecutive scans did not indicate the presence of any anodic peaks. Instead, the transients just showed anodic plateaus lower than current densities of $20 \mu\text{A}/\text{cm}^2$. Similar CV behavior has been demonstrated earlier by Isaacs, White and their co-workers in the neutral pH range.^[84-87] The anodic plateaus were found to be due to currents controlled by conduction through a highly resistive surface film exhibiting high-field

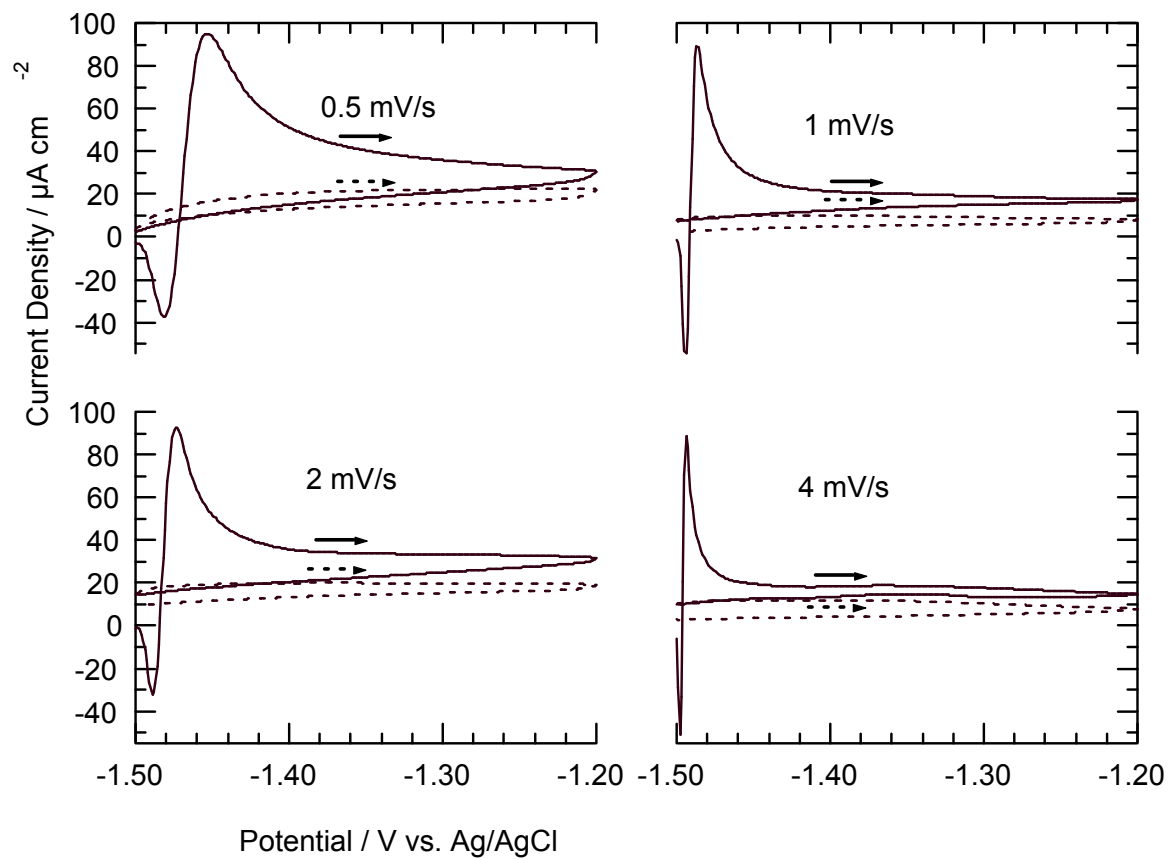


Fig. 3.33 Cyclic voltammetric response at pH 11. The solid and dashed lines represent the first and second voltage cycles, respectively.

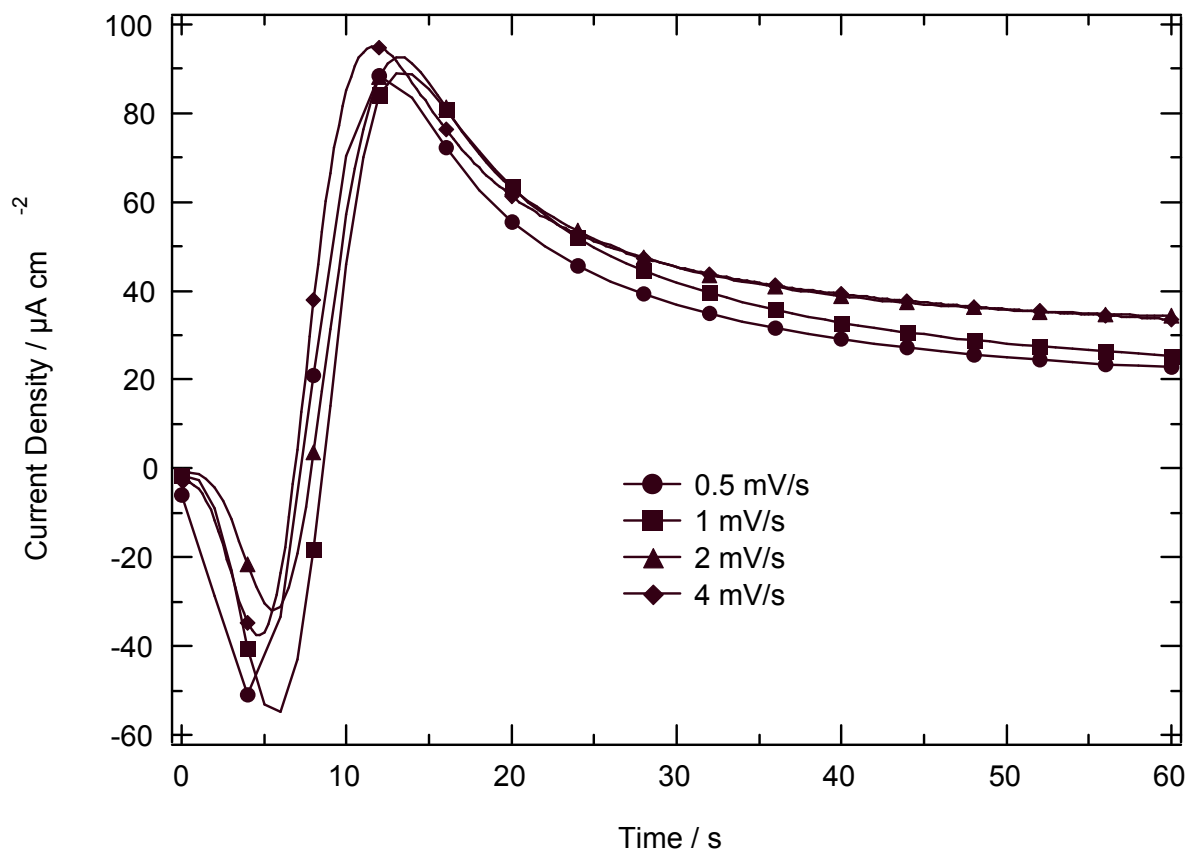


Fig. 3.34 Current density measured during initial portion of first anodic sweeps in Fig. 3.33, plotted against elapsed time during the potential scan.

conduction. Thus, there is a definite transition between a diffusion controlled anodic dissolution mechanism, typical of alkaline solutions, to a passive behavior dominated by a resistive surface film, which is characteristic of neutral solutions. The fact that this occurred over a narrow pH range between 11.75 and 11.00 was quite interesting, and hence making the potential-step experiments for comparison of the differences in the interfacial potential at the two pH values all the more necessary.

3.4.2 Potential-step experiments

The potential at the metal/film interface was determined by analysis of the potential drop through the surface film. These experiments were first devised and applied to oxide films by Hurlen and Haug.^[88] The potential at the aluminum electrode was first held at a constant potential above the open circuit potential (for a period of 5 min in the experiments in this work) in order to obtain a steady state passive current density. The surface film thickness at steady state (δ_{ss}) satisfies the equation

$$E_{init} = E_{m/f} + \frac{\delta_{ss}}{B} \ln \left(\frac{i_{ss}}{i_{ao}} \right) \quad (3.12)$$

where E_{init} is the initial applied potential, $E_{m/f}$ is the potential at the metal/film interface, and the second term on the right hand side is the potential drop through a high-field conducting surface film, in which the current increases exponentially with electric field. In this term, i_{ss} is the approximately potential-independent steady-state passive current density; i_{ao} and B are the pre-exponential current density and field coefficient in the high-field conduction rate equation. After holding the potential at E_{init} for 5 min, a series of potential steps of 0.1 V was

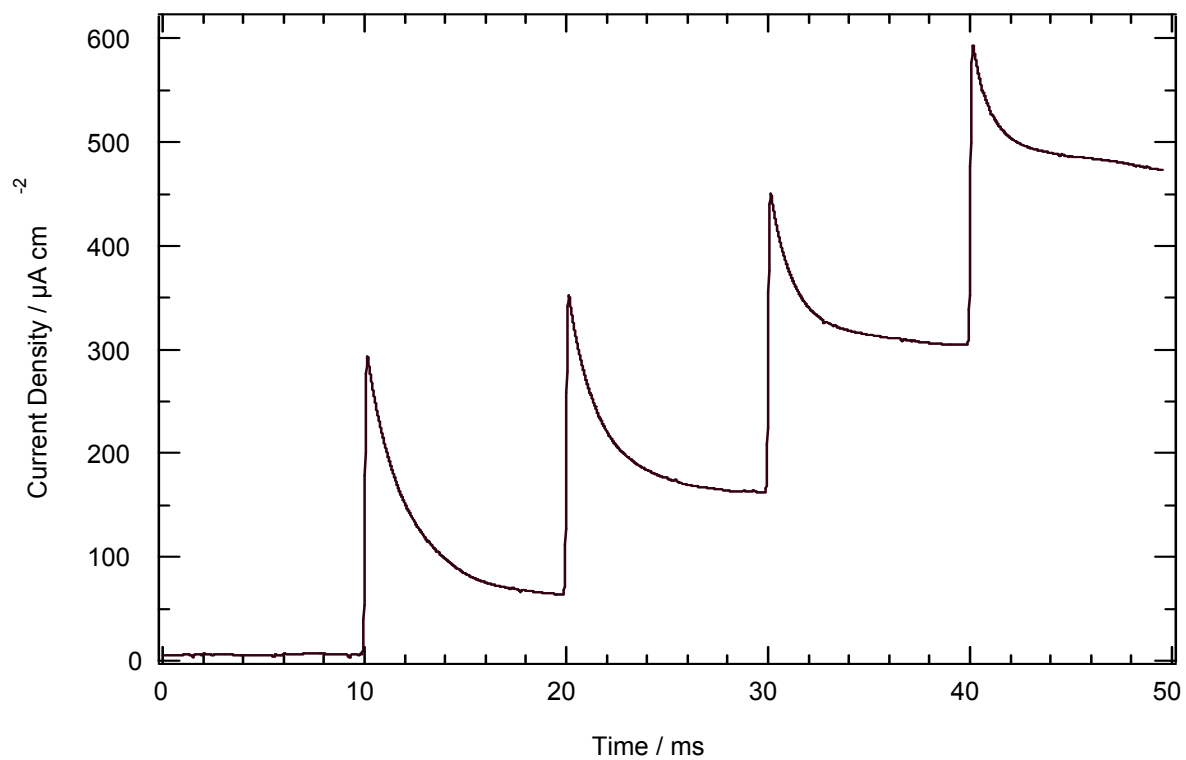


Fig. 3.35 Example of current response to sequence of applied potential steps. The applied potential was initially held at -1.55 V for 5 min, during which a steady passive current was obtained. Then, the potential was stepped by 0.1 V in the anodic direction, at 10 ms intervals. The experiments were done in the pH 11.75 Na_2SO_4 solution.

applied. Each step was of 10 ms duration, during which the potential was held constant at the new value. A typical current transient response of such a potential-step experiment is shown below in Fig. 3. 35. Here the potential was held at -1.55 V (vs. Ag/Ag/Cl) for 5 min (the last 10 ms of which are shown) and then the potential was stepped to -1.45 V, -1.35 V and so on and each potential was held for 10 ms. As can be seen in Fig. 3.35, following each potential step, there is an exponential decay of current. If we consider a typical capacitance value of 10 $\mu\text{F}/\text{cm}^2$ for aluminum and use the estimated cell resistance of 300 $\Omega\text{-cm}^2$, the capacitive time constant comes out to be 3 ms, which is consistent with the decay time of 10 ms seen in the experimental transient. Thus, this transient decay is attributed to capacitive charging.^[89] After the capacitive transient, the current continues to decrease but much more slowly. This decrease is mostly due to anodic film growth. However, calculations based on Faraday's Law showed that there would not be any significant film growth in the 40 ms span of the potential step experiments. Also, no significant changes in the solution composition close to the aluminum surface due to diffusion would be possible in this short time interval. Therefore, the current at 10 ms after each step (i_{step}) represented the conduction current density passed through the initial steady-state film thickness δ_{ss} ,

$$i_{step} = i_{ao} \exp\left[\frac{B(E_{step} - E_{m/f})}{\delta_{ss}}\right] \quad (3.13)$$

where E_{step} is the applied potential during the step, after correction for cell ohmic resistance. Fig. 3.36 and Fig. 3.37 below show the average experimental i_{step} value against the corrected potential for the electropolished aluminum foil in solutions of pH 11.75 and pH 11.00 respectively. The potential value against each line is the applied steady state potential before

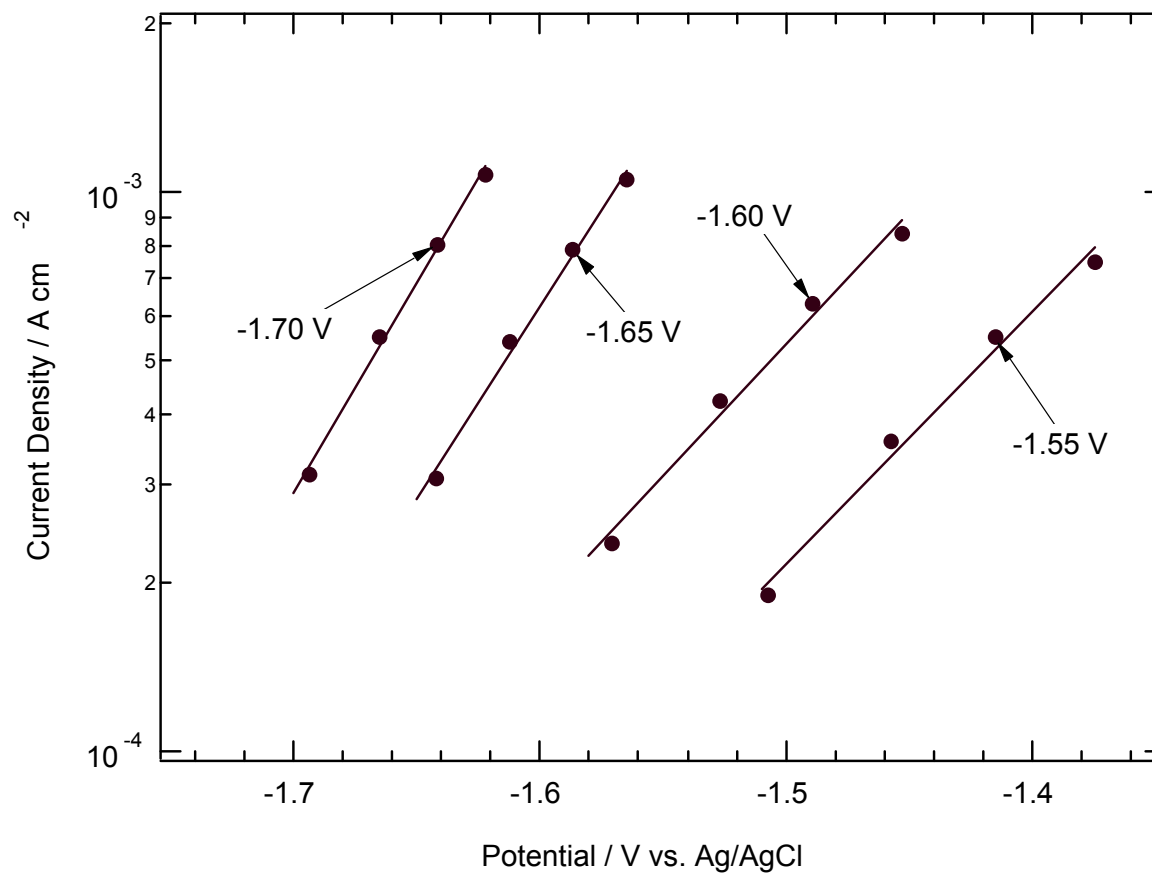


Fig. 3.36 Examples of current-potential characteristics, obtained from the sequential potential step experiments at pH 11.75. Results are shown for various applied steady-state potentials prior to the potential steps.

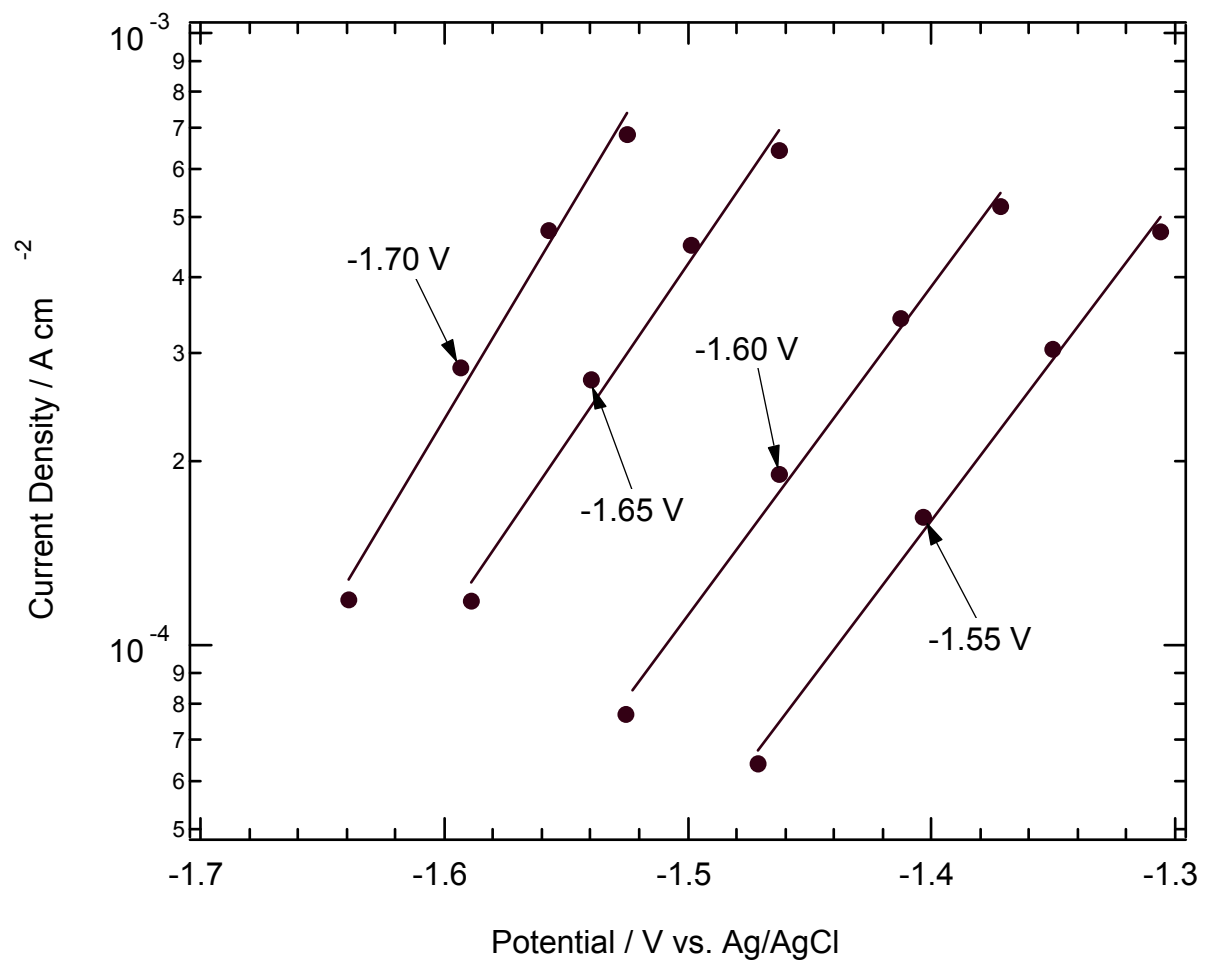


Fig. 3.37 Examples of current-potential characteristics, obtained from the sequential potential step experiments at pH 11.00. Results are shown for various applied steady-state potentials prior to the potential steps.

the potential steps, E_{init} . The linear dependence of the current (on log scale) on the potential shows that the i_{step} value varies exponentially with E_{step} for both pH values, as would be expected from Eqn. 3.13.

We can also notice in both Fig. 3.36 and Fig. 3.37 that the slope $d \ln i_{step} / dE_{step}$ decreases with increasing values of the initial potential E_{init} . From Eqn. 3.13, we can see that the slope $d \ln i_{step} / dE_{step}$ equals B/δ_{ss} . Thus, the decrease of the slope with E_{init} implies an increase in the steady-state film thickness, δ_{ss} with increasing E_{init} . This goes to show that the exponential current-potential relations in Fig. 3.36 and Fig. 3.37 are controlled by conduction rather than electrochemical kinetics. Thus, the inverse slopes in Fig 3.36 and Fig. 3.37 have a direct proportionality to the steady-state film thickness, δ_{ss} . Differentiating Eqn. 3.13 and eliminating B/δ_{ss} from Eqn. 3.12 and Eqn. 3.13 we get a relationship between the inverse slope and initial applied potential as

$$\frac{dE_{step}}{d \ln i_{step}} = \frac{E_{init} - E_{m/f}}{\ln \frac{i_{ss}}{i_{ao}}} \quad (3.14)$$

In Fig. 3.38 below, the inverse slopes ($dE_{step} / d \ln i_{step}$) are plotted against the initial applied potential (E_{init}) for all the pH 11.75 and pH 11.00 potential-step experiments. The data for both the pH values fall mostly along 2 straight lines as shown in Fig 3.38 and expected from Eqn. 3.14. The intercept of these straight lines to the potential axes should give an estimate for the interfacial potential $E_{m/f}$. For the pH 11.00 straight line, the estimated value of $E_{m/f}$ from Fig. 3.38 comes out to be -2.34 V (vs. Ag/AgCl), which is nearly identical to the Nernst potential for the oxidation of Al to Al(OH)₃ or Al₂O₃, -2.32 V.^[1] Hence the film composition

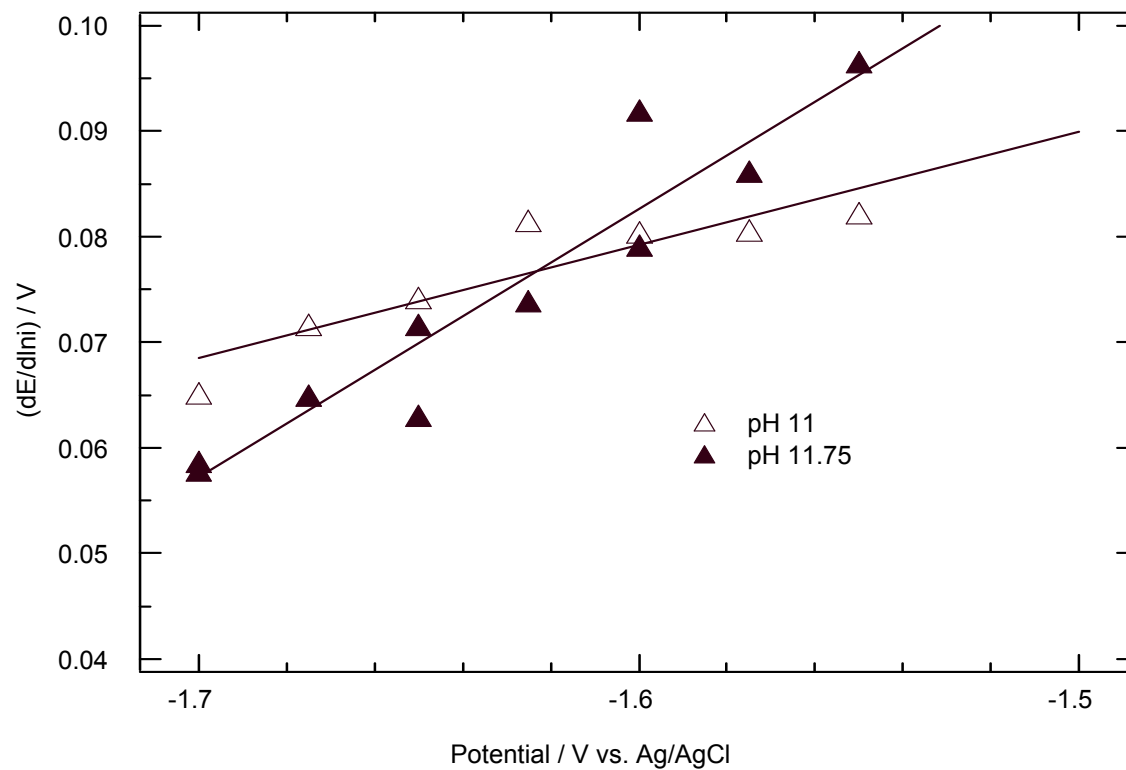


Fig 3.38 Reciprocal slopes of current-potential characteristics at pH 11 and 11.75, plotted against the applied steady-state potential prior to potential steps. Lines are linear regressions of the data. The zero-current intercepts of the regression lines are -2.32 V (pH 11) and -1.92 V (pH 11.75).

at this pH is close to aluminum oxide/hydroxide. On the other hand, the value of $E_{m/f}$ from the pH 11.75 straight line in Fig. 3.38 comes out to be -1.92 V (vs. Ag/AgCl), which is close to the Nernst potential for AlH_3 oxidation, -1.82 V.^[25] Hence a major fraction of the metal-film interface should be in direct contact with aluminum hydride (instead of aluminum oxide or hydroxide) for the interface potential to be determined by the hydride oxidation potential. Thus, these results support the proposed reaction scheme involving AlH_3 as an intermediate (Eqns. 3.7- 3.10). It is clear from these results that the metal-film interface composition is quite different for these two pH values. These interface compositions are used as a basis for modeling the CV experiments and this will be discussed in more detail in the following sections.

3.4.3 Development of the mathematical models for anodic aluminum dissolution reactions

From the discussion of the CV experiments it was inferred that the anodic currents at pH 11.75 were influenced by both solution phase diffusion and film conduction while the currents at pH 11.00 were dominated by film conduction resistance. Two different models were formulated for comparison with the experimental CV results at these two pH values. These models were developed considering only the anodic electrochemical reactions and hence would not hold below the open circuit potential.

(1) Model for dissolution at pH 11.75

Based on the results of the potential-step experiments, for this model we assume that the potential at the metal-film interface is close to the Nernst potential of anodic aluminum hydride oxidation reaction (Eqn. 3.7). The potential is given by

$$E = E_{AlH_3}^o - 2.303 \frac{RT}{F} pH_b + \frac{RT}{6F} \ln \frac{y_{As}}{y_{OHs}} + \phi + iR_s \quad (3.15)$$

where E is the measured electrode potential against the standard hydrogen electrode (NHE), and the standard potential $E_{AlH_3}^o$ represents

$$E_{AlH_3}^o = \frac{1}{6F} \left[\mu_{Al(OH)_3}^o + 3\mu_{H_2}^o - 3\mu_{H_2O}^o - \mu_{AlH_3}^o \right] \quad (3.16)$$

Using the chemical potential of AlH_3 as 25 kcal/mol as cited by Perrault, $E_{AlH_3}^o$ is found to -0.953 V (vs. NHE). The second term on the right hand side of Eqn. 3.15 is a correction for the bulk pH ($pH_b = 11.75$ in this case), the third term is the concentration over potential and the last 2 terms are the potential drop across the surface film (ϕ) and the cell ohmic resistance (iR_s). In the concentration overpotential term, y_{OHs} and y_{As} are the dimensionless concentrations of hydroxide and aluminate ions close to the aluminum electrode surface. y_{OHs} is defined as $y_{OHs} = [OH^-]_s / [OH^-]_b$ where $[OH^-]_s$ and $[OH^-]_b$ are the surface and bulk OH^- activity respectively. y_{As} is defined as $[Al(OH)_4^-]_s / [Al(OH)_4^-]_b^{sat}$ where $[Al(OH)_4^-]_s$ represents the aluminate ion activity close to the surface and $[Al(OH)_4^-]_b^{sat}$ represents the activity of aluminate ions in equilibrium with solid $Al(OH)_3$ at the bulk solution pH. $[Al(OH)_4^-]_b^{sat}$ depends on the bulk solution pH by $[Al(OH)_4^-]_b^{sat} = K_4 [OH^-]_b$ where K_4 is the equilibrium constant of $Al(OH)_3$ formation. The potential drop across the surface film was calculated from the potential-step experimental results at the applied potential of -1.70 V as

$$\phi = \frac{1}{b} \ln \left(\frac{i}{i_{ao}} \right) \quad (3.17)$$

where the parameters b and i_{ao} were taken from the slope and intercept of the regression fit in Fig. 3.36 at -1.70 V. The near surface concentrations of OH^- and $\text{Al}(\text{OH})_4^-$ in Eqn. 3.15 were obtained by solving the diffusion equation for these species,

$$\frac{\partial y_i}{\partial t} = D_i \frac{\partial^2 y_i}{\partial z^2} \quad (3.18)$$

where i could be either OH^- or $\text{Al}(\text{OH})_4^-$. The concentration of Na_2SO_4 supporting electrolyte was considered to be high enough so that the migration flux in the diffusion layer could be neglected relative to the diffusion flux. The boundary conditions at the electrode surface are

$$\left. \frac{\partial y_{\text{OH}}}{\partial z} \right|_{z=0} = \frac{4i}{3FD_{\text{OH}}[\text{OH}^-]_b} \quad (3.19)$$

$$\left. \frac{\partial y_{\text{Al}}}{\partial z} \right|_{z=0} = -\frac{D_{\text{OH}}}{4D_{\text{Al}}K_4} \left. \frac{\partial y_{\text{OH}}}{\partial z} \right|_{z=0} \quad (3.20)$$

The boundary conditions in the bulk solution i.e. when z approaches infinity are quite understandably, $y_{\text{OH}} = 1$ and $y_{\text{Al}} = 0$. Eqns. 3.15-3.19 were solved numerically. The diffusivities D_{OH} and D_{Al} were 5.3×10^{-5} and 8.4×10^{-6} cm^2/s , respectively.^[17, 90] The equilibrium constant K_4 was 0.05.^[83] The values of all model parameters were known from the potential step experiments or other sources.

(2) Model for dissolution at pH 11.00

Again, going by the results of the potential-step experiments, the model for pH 11.00 assumes that the reaction at the metal/film interface is the direct oxidation of aluminum. The current is controlled by high-field conduction in the surface film and the potential at the interface is Nernst potential for the aluminum oxidation reaction. As seen in the cyclic

voltammograms for the pH 11.00 solution, the current densities are small (less than 100 $\mu\text{A}/\text{cm}^2$ in all cases) owing to the large conduction resistance. Hence the concentration overpotential and ohmic drop are neglected in this case. The applied electrode potential can be represented as the Nernst potential of aluminum oxidation by the relation

$$E = E_{Al}^o - 2.303 \frac{RT}{F} \text{pH}_b + \phi \quad (3.21)$$

where the standard potential E_{Al}^o is

$$E_{Al}^o = \frac{1}{3F} \left[\frac{3}{2} \mu_{H_2}^o - 3 \mu_{H_2O}^o - \mu_{Al}^o + \mu_{Al_2O_3}^o \right] \quad (3.22)$$

which comes out to be -1.50 V (vs. NHE).^[1] The film was considered to be Al_2O_3 for which the conduction parameters have been estimated from studies of anodic alumina films.^[90]

Ion-transfer processes control the passage of current through the film/solution interface. O^{2-} ions from the film react to form OH^- or H_2O in solution and Al^{3+} ions in the film form $\text{Al}(\text{OH})_4^-$ in solution.^[91] O^{2-} transfer leads to film growth or dissolution affecting the conduction resistance. Since the oxygen transfer process typically shows facile kinetics^[91] and going by the low current densities during the CVs shown in Fig 3.33, the potential drop at the film/solution interface is assumed to be close to equilibrium with respect to the O^{2-} transfer process. Also, since the kinetics of Al^{3+} ion transfer are relatively slower, this constant interfacial potential drop implies that the metal ion transfer current density could be considered to be approximately fixed at a value i_{co} . The rate of change of film thickness can thus be written as

$$\frac{d\delta}{dt} = \frac{(i - i_{co}) \Omega_{ox}}{6F} \quad (3.23)$$

where δ is the film thickness and Ω_{ox} is the molar volume of the oxide. Since i_{co} is the metal ion transfer current density, the term $(i - i_{co})$ represents the part of the current density passing the film/solution interface which contributes to the formation of O^{2-} ions in the film. The conduction current i follows the high-field conduction equation, $i = i_{ao} \exp\left(\frac{B\phi}{\delta}\right)$ where ϕ is the electric field across the film. On substituting for the value for δ from the high-field equation in Eqn. 3.23, a differential equation for $i(t)$ was obtained

$$\frac{di}{dt} = \frac{iv \ln(i/i_{ao})}{\phi} \left(1 - \ln(i/i_{ao}) - \frac{\Omega_{ox}(i - i_{co})}{6FBv} \right) \quad (3.24)$$

where v is the potential scan rate (dE/dt) during the CV experiment. The parameters i_{ao} , B and Ω_{ox} were assigned values characteristic of anodic oxide films: 2.0×10^{-15} A/cm², 3.44×10^{-6} cm/V, and 32.9 cm³/mol respectively.^[90]

This differential equation for this CV model (Eqn. 3.24) is mathematically the same as previous CV models for aluminum developed for the neutral pH range by White, Isaacs et al.^[84-87] High-field conduction was considered for both models with the expression of “oxide dissolution rate” in the previous models replaced by the metal ion dissolution current density, i_{co} , in the present model. If we consider the oxide dissolution rate to be R_{dis} (as in the model of Ref. 84), then in the present model, i_{co} would be equivalent to R_{dis}/nF . The present model considers the transfer of oxygen and aluminum ions to and from the film into the aqueous solution. On the other hand, in the previously developed models, Al₂O₃ dissolution was considered as a stoichiometric entity violating the continuity of the interface and conduction current since this would imply that no current is passing at the film/solution interface. Thus,

although the resulting models in both cases are equivalent, the present model is consistent with what is known about interfacial ion-transfer processes.

On integrating Eqn. 3.24 using a constant value of i_{co} , the predicted CV models showed similar anodic current plateaus as in the case of previous CV models in the neutral pH range, but the anodic peaks present in the first scan as shown in the experimental CVs in Fig. 3.33 were absent. These anodic peaks were obtained in the simulated CVs when a transient decay of i_{co} was introduced in the model

$$i_{co} = i_{co}^f + (i_{co}^i - i_{co}^f) \exp\left(-\frac{t}{t_c}\right) \quad (3.25)$$

where i_{co}^i and i_{co}^f are the initial and final values of i_{co} and t_c is the time constant for the decay. The kinetics of metal ion transfer (i_{co}) is expected to be sensitive to the oxide composition and hence to the pH of the bulk solution. Therefore, the decay in Eqn. 3.25 could be because of the relaxation of the film surface from its initial composition in the 1 M NaOH pretreatment solution (possibly as AlH_3), to its final condition in the pH 11.00 solution used in CV experiments.

(3) Comparison of model predictions with experimental CVs

The predictions of the CV model developed for the pH 11.75 solution based on AlH_3 oxidation at the metal/film interface (Eqn. 3.15 -3.21) is shown below in Fig 3.39. The results of the experimental CVs are also plotted at each potential scan rate. Since there were no adjustable fitting parameters in this model, we can say that the shapes of the CV waveforms predicted by the model and those of the experimental CVs are in very good agreement. Since

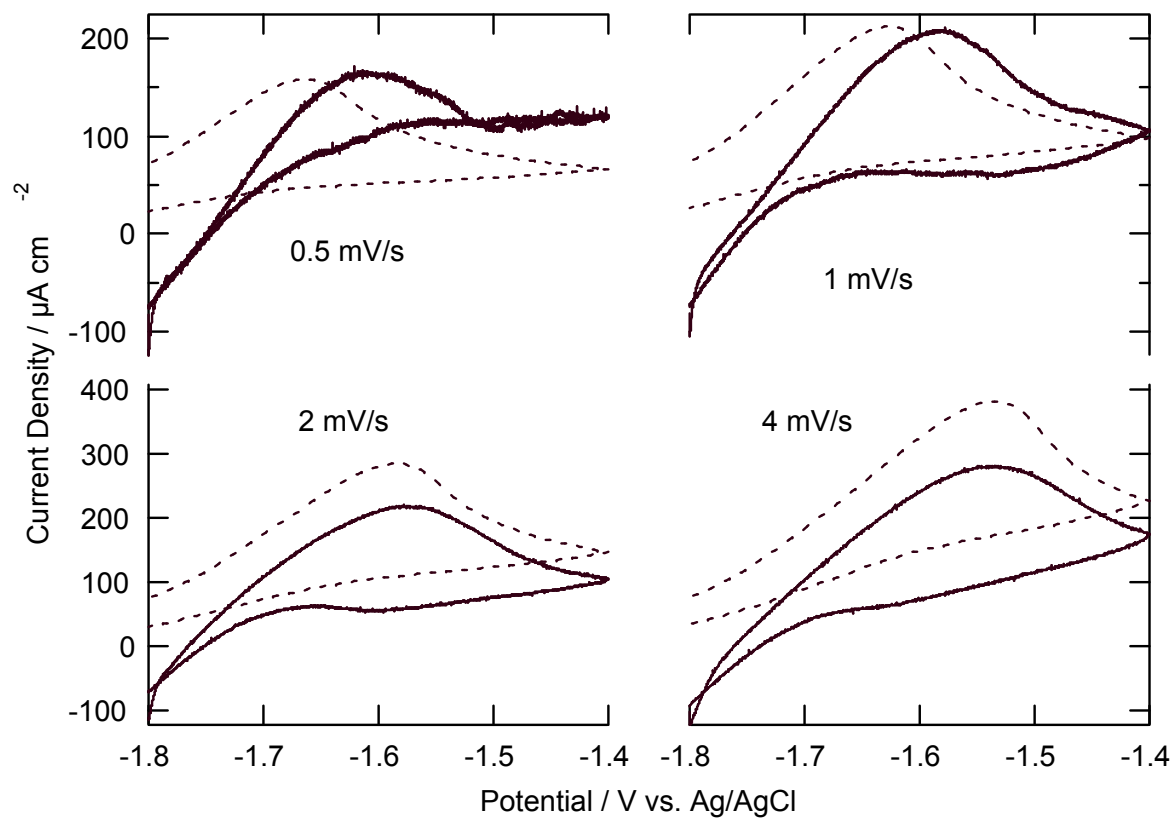


Fig. 3.39 Comparison of experimental (solid lines) and simulated (dashed lines) cyclic voltammetric responses at pH 11.75, at various scan rates.

cathodic reactions were not included in this model, deviations close to the open circuit potentials would naturally be expected. Also, film growth and dissolution was not included in this model because the film/solution interface kinetics was not known. Inherent simplifications in the model, say for example assuming a constant conduction resistance (although Fig. 3.36 does indicate that the surface film thickness depends on applied potential) would explain the discrepancies in the anodic peak currents and potentials at high scan rates. In spite of this, the good agreement shown in Fig 3.39 is an indication that the interfacial potential at this pH is controlled by the AlH_3 oxidation reaction.

The comparison of the experimental CVs for pH 11.00 (Fig. 3.33) with the predictions for the first and the second cycles of the aluminum oxidation model (Eqn. 3.24-3.25) are shown below in Fig. 3.40 and Fig. 3.41 respectively. The initial film thickness was set to 1.7 nm, and i_{co}^i , i_{co}^f , and t_c were $135 \mu\text{A}/\text{cm}^2$, $10 \mu\text{A}/\text{cm}^2$, and 20 s, respectively. When these parameters were applied to all scan rates, the model calculations agreed very well with experimental CVs. The time of the anodic current peak as well as the subsequent current were very well captured by the model for all scan rates. These results support the assumption of an exponential decay of i_{co} (Eqn. 3.25) associated with an adjustment of the surface film during transfer of the foil from pH 13.5 (1M NaOH) to pH 11.00. The value of i_{co} had decayed to the final value i_{co}^f by the time the second scan cycle starts. Thus, the model shows similar second scan anodic current plateaus as seen in the experimental CVs (and observed before for neutral pH solutions) with the plateau heights increasing with increasing scan rate. Thus the excellent agreement of the model predictions with the experimental CVs is evidence that high-field conduction in the surface film controls the anodic currents at pH 11.00.

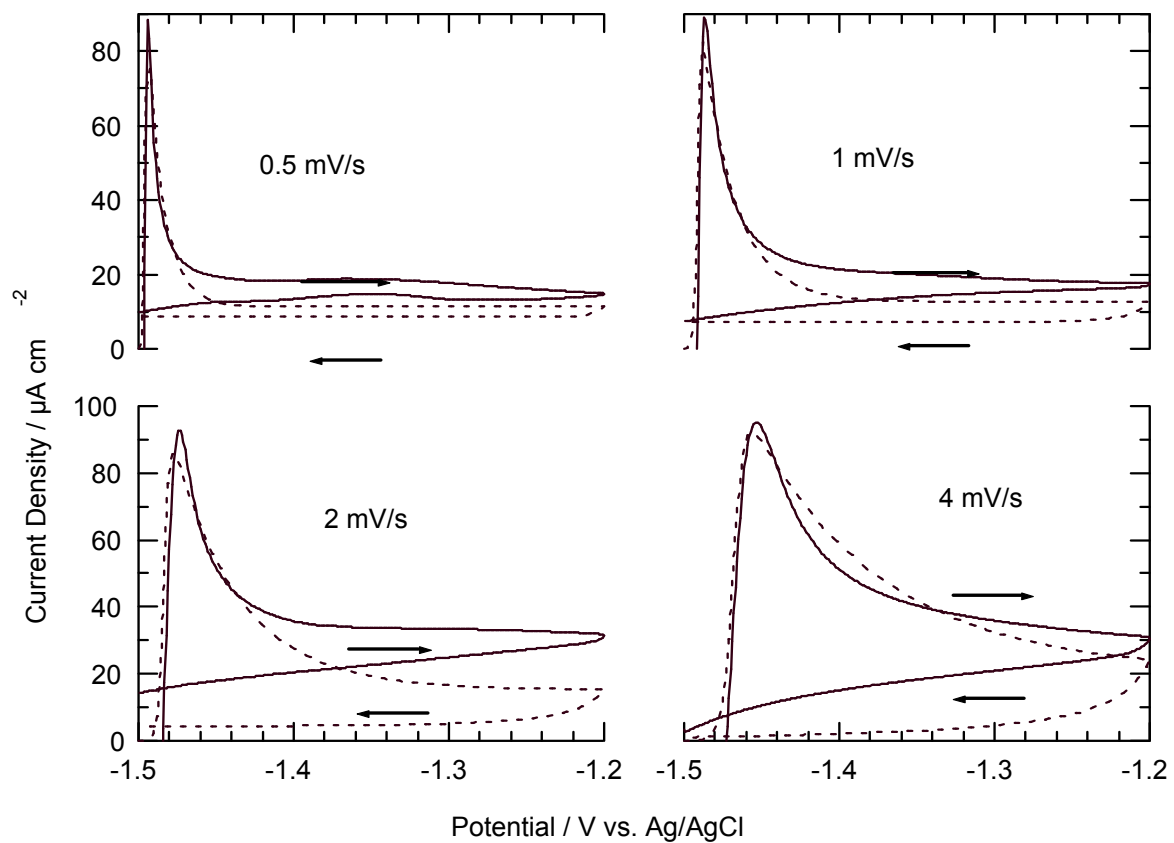


Fig. 3.40 Comparison of experimental (solid lines) and simulated (dashed lines) cyclic voltammetric responses at pH 11. First scan for various scan rates.

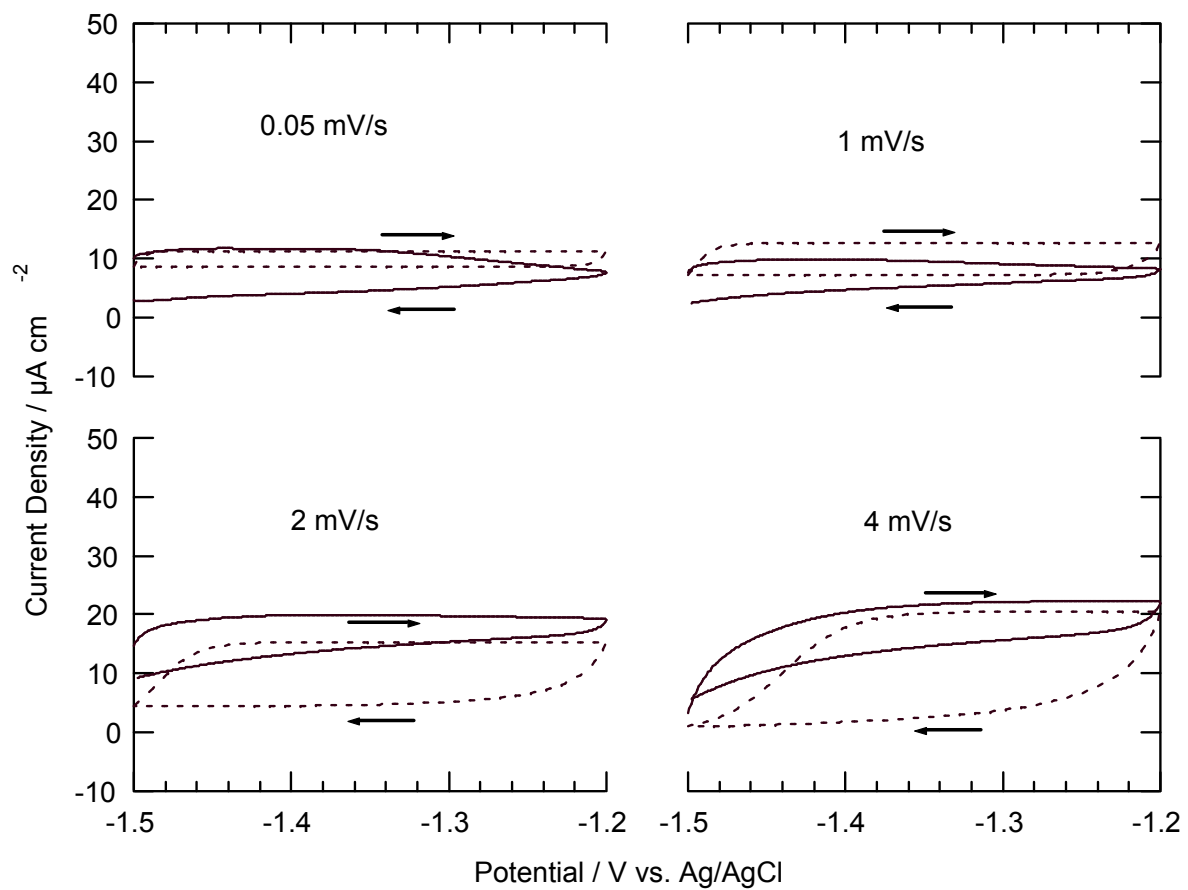


Fig. 3.41 Comparison of experimental (solid lines) and simulated (dashed lines) cyclic voltammetric responses at pH 11. Second scan for various scan rates.

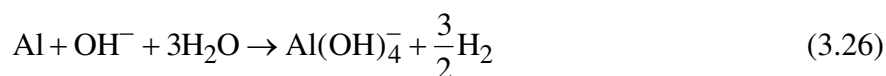
The cyclic voltammetry and potential step experiments show that there is an abrupt change in the surface film properties and dissolution mechanism in the pH range from 11.00 to 11.75. The film has a high ionic conduction resistance at pH 11.00 with the primary reaction at the metal/film interface being aluminum oxidation. At pH 11.75, the film has a relatively lower conduction resistance with the interface potential following AlH_3 oxidation potential implying that the interface is in direct contact with the hydride during the alkaline dissolution process. The study in the next section was done to identify the conditions in which the dissolution potential corresponds to the Nernst potential of hydride oxidation. We will discuss factors affecting the corrosion potential of aluminum in alkaline solutions like the pH, aluminate ion concentrations, build of surface hydride and enrichment of surface impurities and complexities involved in the seemingly simple corrosion process.

3.5 Factors affecting the corrosion potential of aluminum in alkaline solutions

This study focuses on factors controlling the time-evolution of the corrosion potential of aluminum in alkaline solutions. The effect of the solution phase and metal phase compositions during dissolution were studied using a detailed analysis of the open-circuit potential transients and cyclic voltammetric response.

3.5.1 Effect of solution composition on open circuit potential

As described in the experimental section, the open circuit potentials were measured for 4N electropolished foils in 0.1M Na₂SO₄ solutions adjusted to different pH values by addition of solid NaOH crystals. Fig. 3.42 below shows examples of open circuit potential transients for representative pH values of 13.00, 12.25, 12.01 and 11.74. In all these OCP transients, the potential decreased abruptly to a minimum value in a time less than 20s and then increased gradually. The surface oxide film is highly soluble in alkaline media and this initial decrease in open circuit potential is an effect of the dissolution of the film.^[1, 92] With increasing pH of the solution, the potential minima shift to more negative values and the rate of potential decrease is also faster owing to increased oxide dissolution rate. Fig 3.43 shows the minimum open circuit potential values for a series of bulk pH values. It is seen that with decrease of pH, the OCP minima moves almost linearly to less negative values. If AlH₃ is considered to accumulate as a corrosion product then the overall dissolution reaction is given by Eqn. 3.10 discussed earlier. Also, if AlH₃ decomposes completely by reaction with water then the overall dissolution reaction is given by



In both cases, there is depletion of OH^- ions near the metal surface. Using Sand equation^[81] we can estimate the pH change at the aluminum surface if we assume a constant dissolution rate during the open circuit treatment. If we consider a dissolution rate of 2 nm/s as is the case for dissolution in 1M NaOH (pH of 13.50, which is the highest pH considered in this study), the pH change at the metal surface up to the time of the potential minimum is found to be very small. Since the dissolution rate decreases exponentially with decreasing pH values,^[1] the change of OH^- ion concentration and hence the change in pH up to the minimum is going to be even smaller if the initial bulk solution pH is lower than 13.50. Hence the decrease of surface pH due to OH^- consumption has very little effect on the minimum potentials in Fig. 3.43.

As can be seen in Fig. 3.43, the data points for the pH dependence of the minimum potential are very close to the data for open circuit potentials from Perrault's work (although his work had a prolonged cathodic polarization pretreatment).^[25] The Nernst potential for the hydride oxidation reaction (Eqn. 3.7) is shown in Fig 3.43 by the dotted line and has a slope of $(7 * (2.303) * RT/6F)$ or 69 mV/pH unit. The present data clearly lies on a line parallel to this and is slightly displaced in the anodic direction by 10-30 mV. This small offset is probably because of some uncertainty surrounding the value of the chemical potential of AlH_3 , which affects the intercept of this line.^[25] From Fig. 3.43, we can conclude that the minimum potentials follow the AlH_3 equilibrium. Unlike Perrault's work, the samples in this study were not pretreated by cathodic charging. Hence the AlH_3 in this case must have formed during the open circuit dissolution itself i.e. by proposed reactions 3.9 and 3.10 discussed in section 3.3.

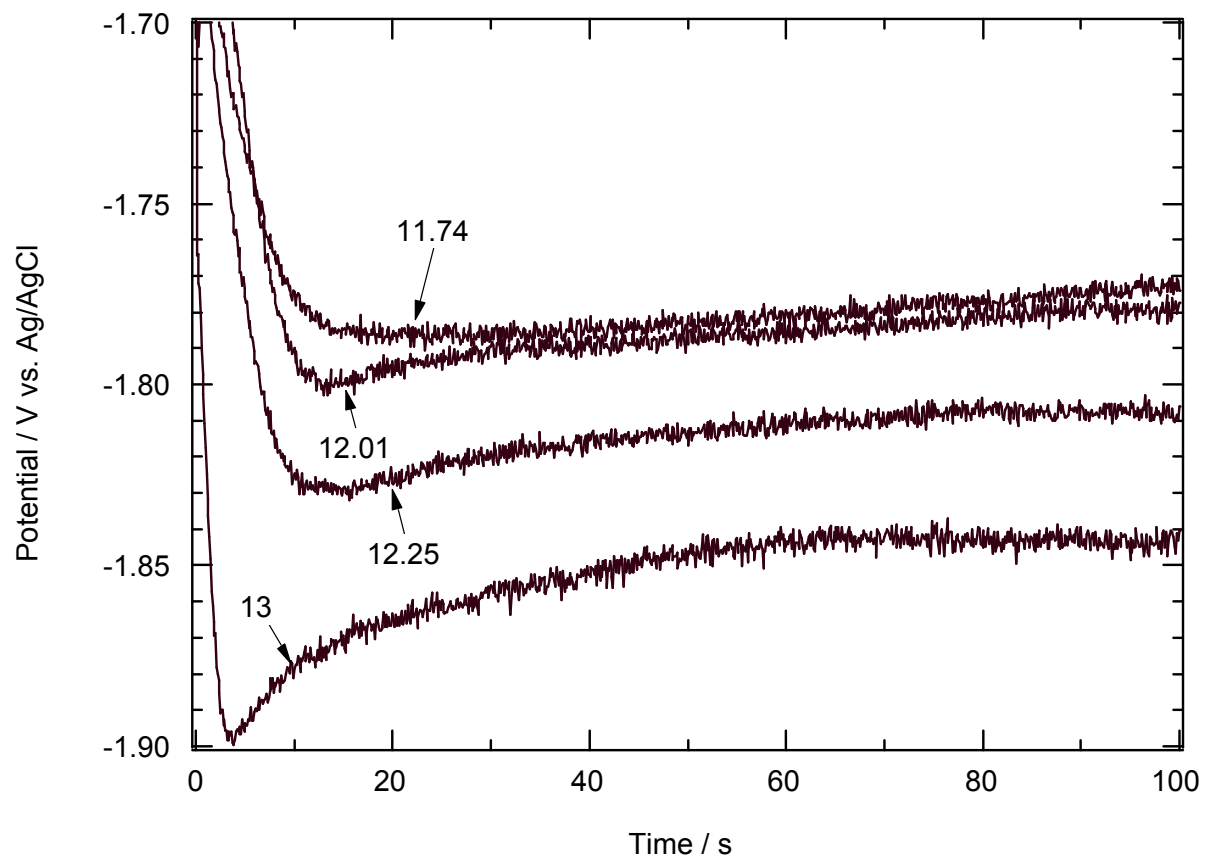


Fig. 3.42 Open circuit potentials of 4N electropolished Al foils in 0.1 M Na_2SO_4 solutions adjusted to various pH values by addition of NaOH.

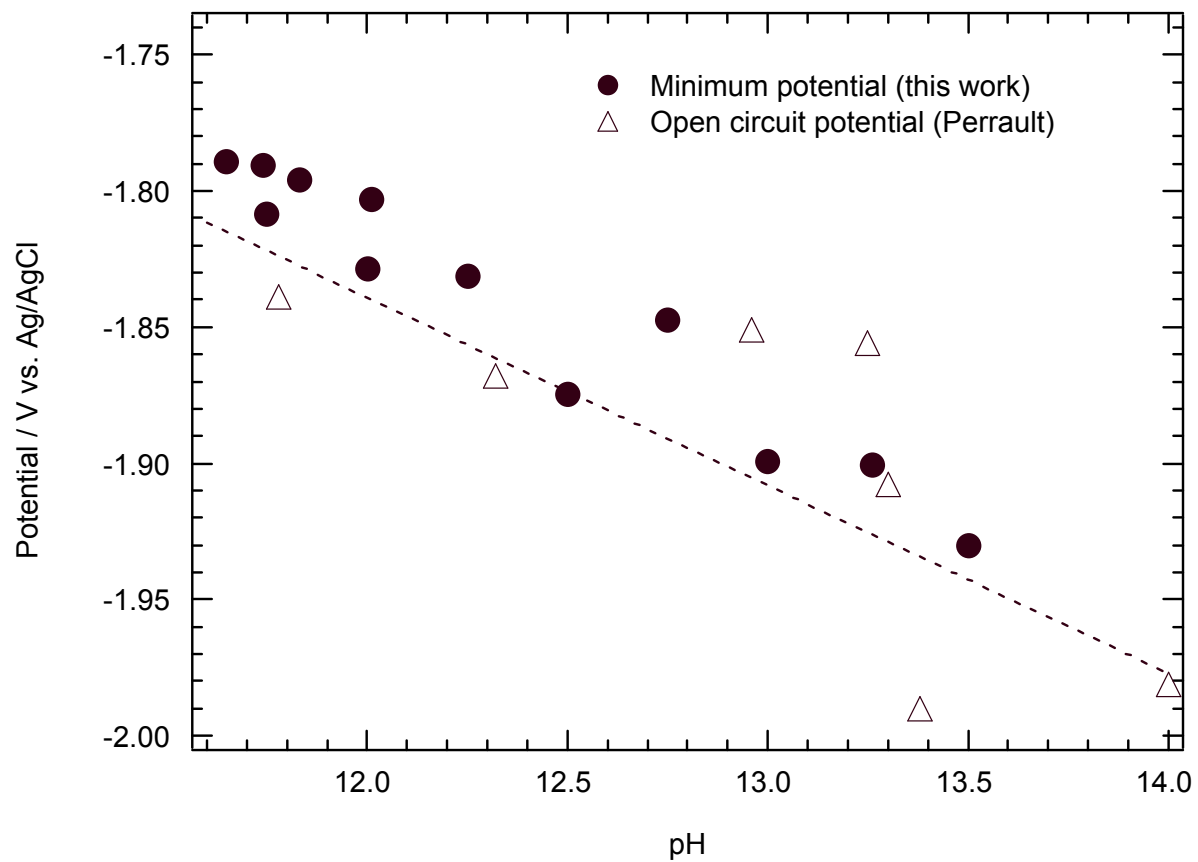


Fig. 3.43 Minimum potential of open circuit potential transients like those in Fig. 3.42, as a function of bulk pH.

The effect of Al(OH)_4^- concentration on the minimum potentials for a fixed pH value of 13.5 was studied for the electropolished 4N foils. This is shown in Fig. 3.44 below. The aluminum concentration ranged from 0 to 0.05 M. It can be seen that the minimum potentials are quite independent of the aluminate concentration but the transients separate out later with more anodic potentials for increasing aluminate concentrations. As discussed earlier, the pH near the Al surface at the time of the potential minimum (~3-4 s) should not be very different from the bulk solution pH. According to the AlH_3 oxidation reaction (Eqn. 3.7), the potential should only decrease by 10 mV per decade increase of aluminate concentration. For example, between the aluminum ion concentrations of 0.01 M and 0.05 M, the potential change is just 7 mV. Such small changes would be undetectable given the level of reproducibility of the open circuit measurements. Thus, the dependence of the minimum potential on the pH (Fig. 3.42/ Fig. 3.43) and the aluminate ion concentration (Fig. 3.44) are both consistent with the oxidation of AlH_3 being the principal anodic process. The anodic reaction kinetics are sufficiently rapid such that the corrosion potential at the minimum is determined by the Nernst potential of the oxidation reaction (Eqn. 3.7) and the corrosion rate is determined by kinetics of the cathodic reaction.

The separation of the open circuit transients in Fig. 3.44 cannot be explained on the basis of the Nernst potential for aluminum hydride dissolution. For example at 40 s, the OCP for 0.05 M aluminate concentration is 70 mV anodic as compared to that at 0.01 M while only a change of 7 mV is expected as mentioned earlier. This increased dependence of the potentials on the Al(OH)_4^- concentration will be discussed in the later sections.

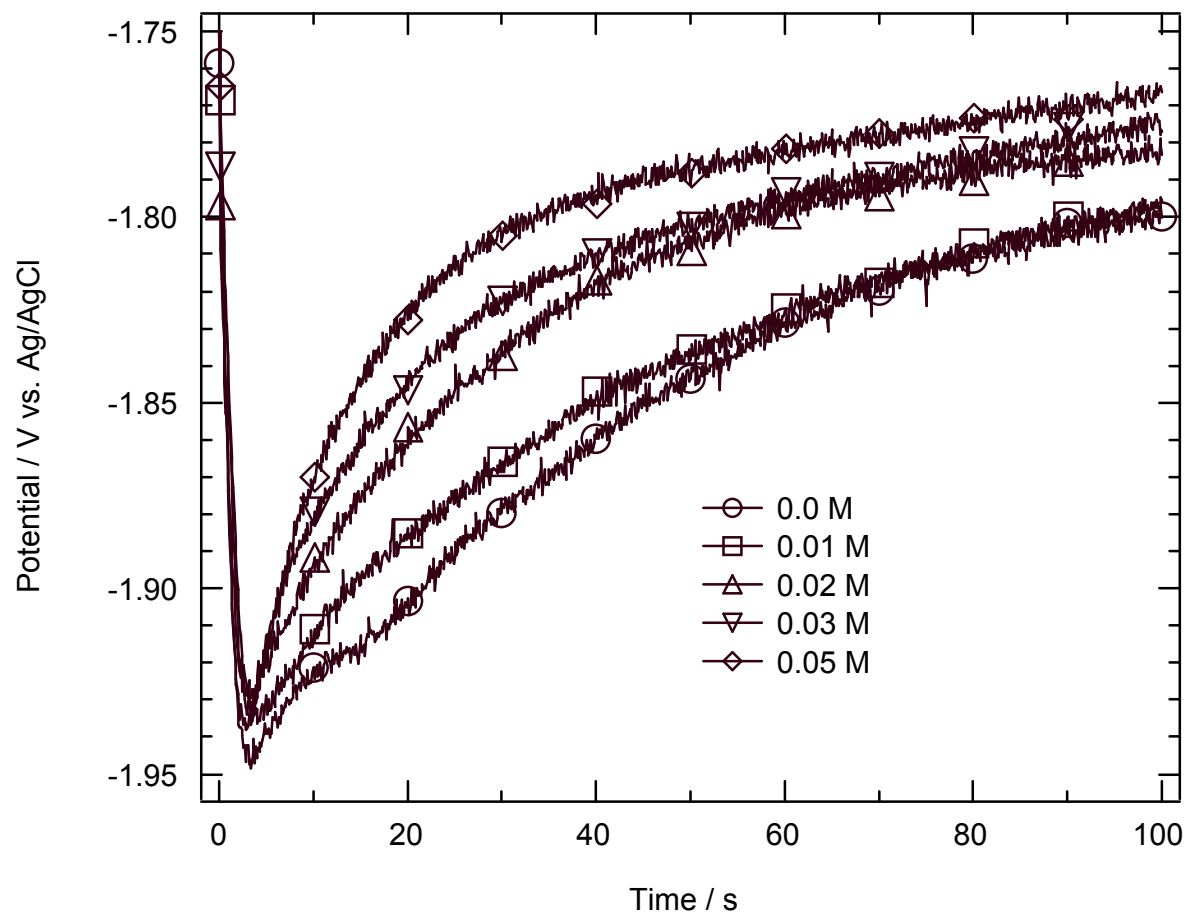


Fig. 3.44 Examples of open circuit potential transients of Al foils in Al_2SO_4 - containing 1 M NaOH baths at pH 13.5. The parameter is the Al_2SO_4 concentration.

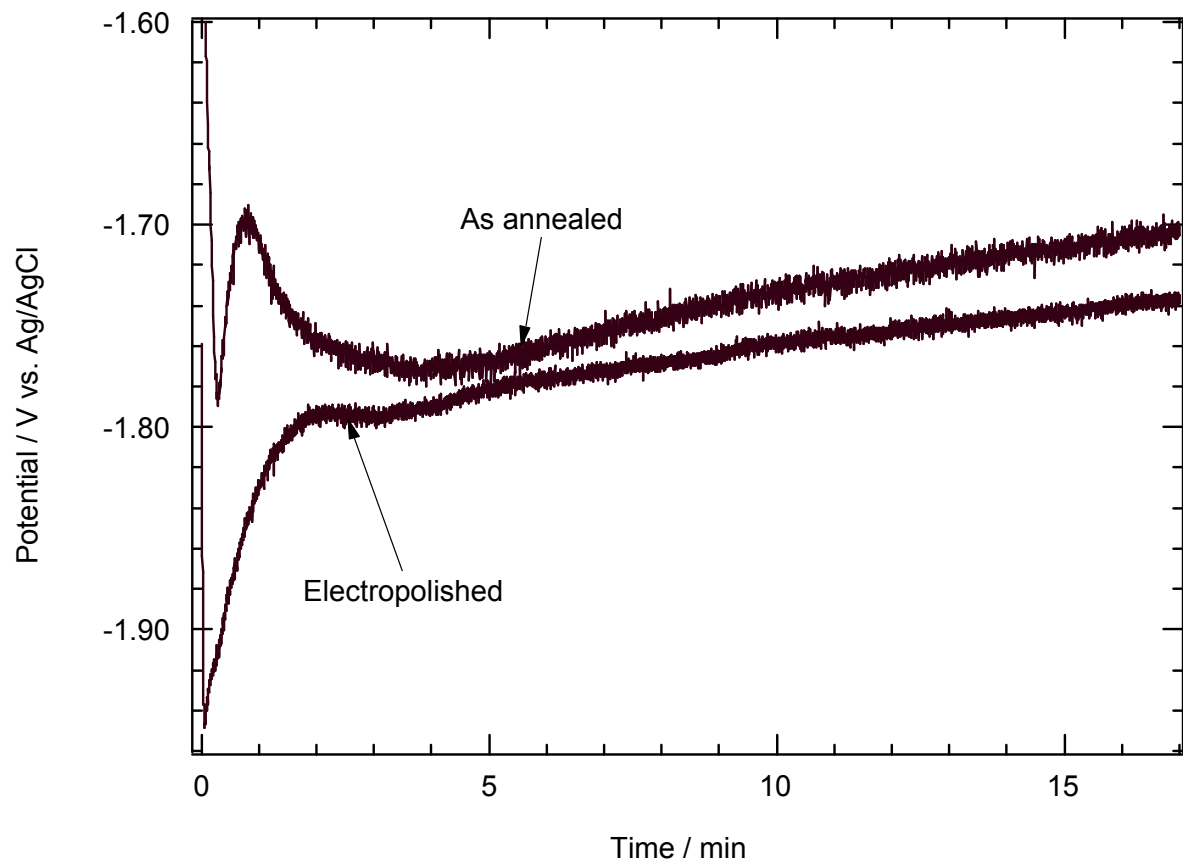


Fig. 3.45 Comparison of open circuit potential transients for electropolished and as-annealed Al in 1 M NaOH.

3.5.2 Effect of metal properties on open circuit potential

(1) Comparison of OCP transients of as-annealed and electropolished foils

Fig 3.45 below shows the open circuit transients for electropolished and as-annealed foils in 1M NaOH. Clearly, the transients are very different in the first 2-3 min of dissolution but then converge and follow almost parallel behavior after that. The minimum potential was about 160 mV more anodic in the case of the as-annealed foil. The transient for the as-annealed foil also had a potential maximum after that, which was not present in the transient for the electropolished foil. The same OCP behavior was displayed for all as-annealed foils from different manufacturers but having the same bulk composition i.e. potentials more anodic than that of the electropolished foils in the first 2-3 min.. Thus, while the electropolished foils followed the Nernst potential for AlH_3 oxidation, the as-annealed foils were anodically polarized with respect to that. From the transient of the electropolished foil in Fig. 3.45, we can also notice that its slope abruptly decreases from about 70 mV/min to 2 mV/min at a time close to 2 min. This could be an indication of different phenomena controlling the open circuit potential at early or later times.

The as-annealed 4N foils used in these experiments are the ones typically used for aluminum electrolytic capacitors. The surface composition and microstructure of these foils are supposed to be very different from the bulk foil properties. For example, there is an accumulation of metallic impurities near the surface.^[93-96] There is also a pronounced tendency for etching parallel to the surface especially along the rolling direction.^[34, 97] The latter has been argued to be because of a large concentration of subsurface voids near the

metal-film interface.^[15, 35] Thus, although it is difficult to assign a definite reason to the anodic polarization of the as-annealed foils, it is possible that the inhomogeneities in the metal close to the surface play a role in it. These inhomogeneities could be removed after about 2 min dissolution, and hence explaining behavior similar to the electropolished foil after 2 min. The dissolution rate for the 4N foils was found to be about 2 nm/s. Thus, thickness of metal dissolved in this time should be around 100-200 nm. The thicknesses of the subsurface defect layer (consisting of open volume voids) from positron annihilation experiments have been found to be around 120 nm.^[15] Thus, these two thickness values are in reasonable agreement considering the fact that the dissolution rate measurement is an average estimate from a prolonged dissolution experiment and could be slower through the initial defect layer. Fig 3.45 certainly shows that the surface condition plays a role in the evolution of the open circuit potential transient for the aluminum foil.

(2) Effect of impurity concentrations on open circuit potentials

The major impurities in the aluminum foils used in this work are Cu, Fe, Si and Pb. These impurities can accumulate near the surface and affect the open circuit potential by forming electrochemically active phases. Iron is mostly found in the aluminum matrix in the form of second phase intermetallic particles because of its low solid solubility in aluminum.^[98] Such phases could be cathodically active and lead to the observed anodic polarization. For instance, intermetallic Al₃Fe particles formed during annealing of the aluminum were found to increase the cathodic reactivity of the surface thereby shifting the corrosion potential in the anodic direction.^[99] Micro-segregation of impurities like Fe, Si has been reported in pitting studies of high purity aluminum as well.^[100, 101] Similarly,

enhancement of localized cathodic activity due to formation of intermetallic Cu based particles in Al has also been reported.^[102-104]

In this work, aluminum foils with varying bulk Cu concentrations were used for studying the effect of enrichment of surface copper on the open circuit potentials. As shown in Table 2.1 earlier, these foils had 8, 49 and 96 wt. ppm of copper respectively and will be referred to as foils A1, A2 and A3. The concentrations of Fe, Si and Pb in these foils were almost identical as seen in Table 2.1. Since copper is more noble than aluminum, accumulation of copper near the metal/film interface during alkaline dissolution is due to the faster dissolution of aluminum as opposed to copper.^[37, 94] Assuming complete impurity retention at the surface, the concentration of Cu impurities can be obtained from mole balance as^[37]

$$C_{is} = C_{is}^0 + V_d C_{ib} t \quad (3.27)$$

where C_{is} is the surface Cu concentration, C_{is}^0 is the initial copper concentration at the surface, V_d is the dissolution velocity, C_{ib} is the bulk copper concentration and t is the time of dissolution. For aluminum foils having about 50 ppm Cu (like the 4N capacitor foils), Cu enrichment near the surface was detected by Rutherford backscattering spectrometry at dissolution times of 5 min or higher.^[37]

Fig. 3.46 below shows the open circuit potentials for as- annealed foils A1, A2 and A3 (Cu 8, 49 and 96 ppm approx.) in 1M NaOH for dissolution times in up to 2 hours. As can be seen, the transients are almost the same up to about 15 min after which they separate out with higher open circuit potentials for higher copper concentrations. According to the

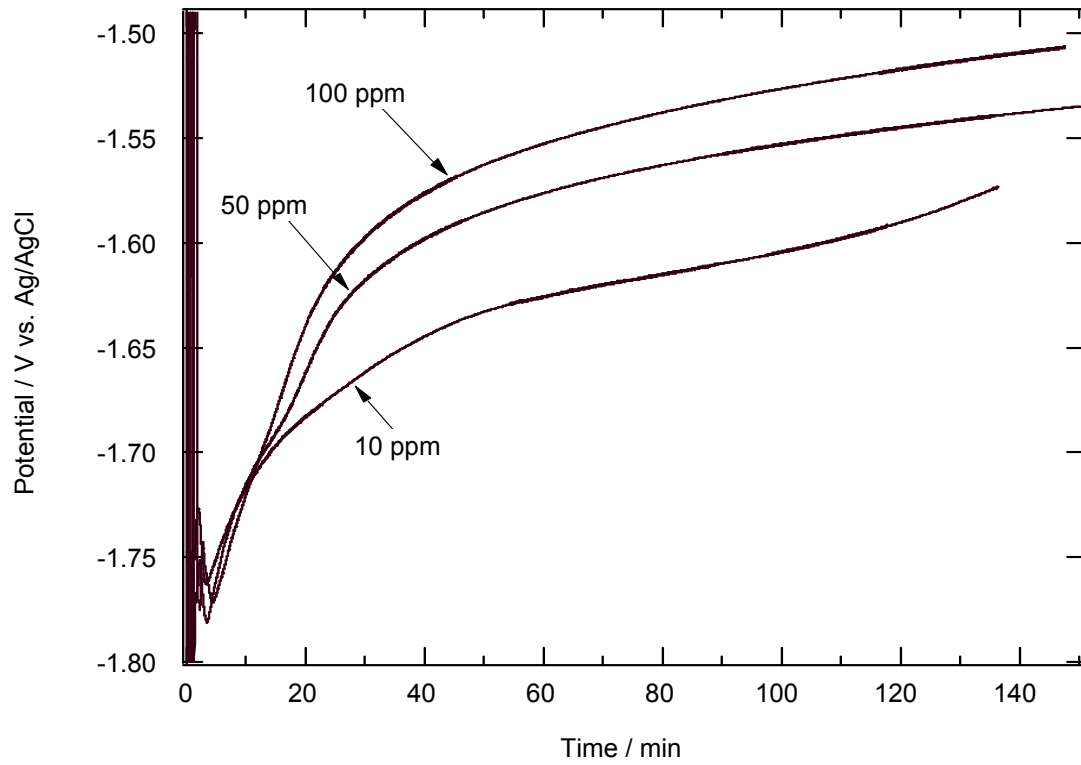


Fig. 3.46 Open circuit potential transients in 1 M NaOH for as-annealed Al foils containing variable bulk concentrations of copper impurity.

mole balance Eqn. 3.27, the Cu concentrations should increase by 0.4, 2.5 and 5×10^{-11} mol $\text{cm}^{-2} \text{min}^{-1}$ for the 8, 49 and 96 ppm Cu foils. This order of the open circuit potentials with more anodic potentials for higher Cu content follows the argument that the surface Cu impurities are cathodically active and thus anodically polarize the aluminum. Si and Fe could also affect the open circuit potentials of the aluminum since they were also present in the aluminum foils used for these experiments in reasonable concentrations (~23-24 wt. ppm). The differences in the OCP values in Fig. 3.46 though are only due to differences in Cu concentrations because Fe, Si and Pb contents were the same for the three foils considered. All in all, these results do demonstrate that surface enrichment of metallic impurities can affect the corrosion potential during alkaline aluminum dissolution.

3.5.3 Effect of interrupted dissolution on open circuit potential transients

The results in sections 3.5.1 and 3.5.2 clearly indicate that open-circuit potentials for aluminum during dissolution in alkaline solutions are affected by both solution and metal phase compositions. In order to get a better idea of how these contribute to the OCP, another set of experiments was conducted in which the dissolution was interrupted and then resumed in the same alkaline solution. 4N electropolished foils were dissolved for various times between 20 s and 10 min in 1 M NaOH while measuring the OCP. Then, the foil was removed from the solution, rinsed in DI water to stop the dissolution, dried and then re-immersed in a fresh 1 M NaOH solution to measure the OCP. OCP transients before and after the interruption are shown in Fig. 3.47 (20 s and 1min) and Fig. 3.48 (2 min, 5 min and 10 min) below. As can be seen, the minimum potentials during the second immersion was

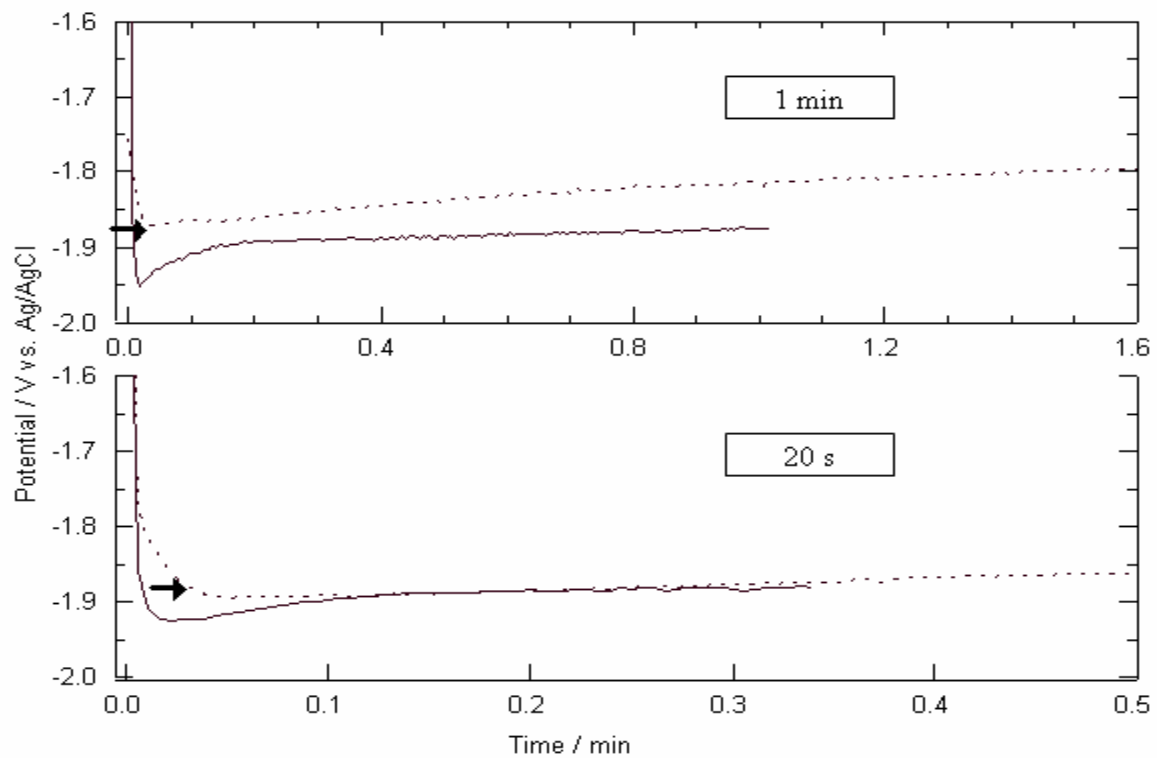


Fig. 3. 47 Potential transients of interrupted dissolution experiments. In each panel, the solid and dashed lines are the potential transients before and after the Al foil was removed from the 1 M NaOH solution, rinsed, dried, and then re-immersed. Arrows represent the potential measured at the time of the interruption. Interruption times are 20 s and 1 min.

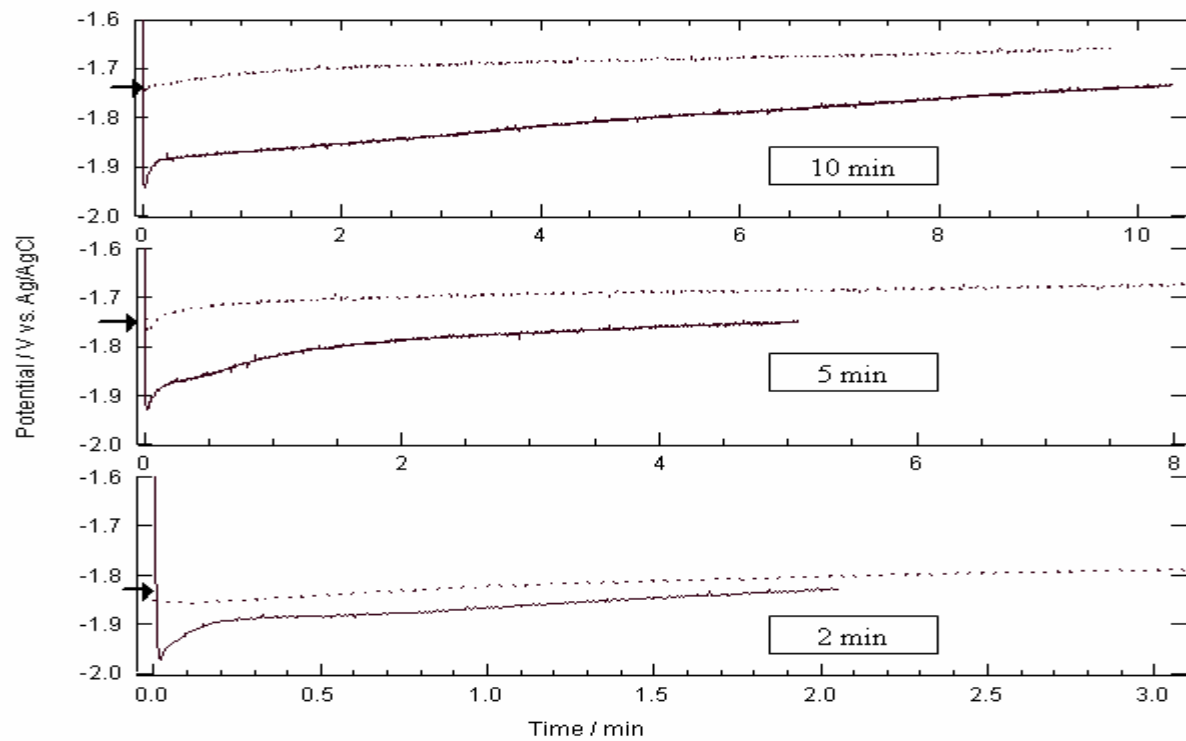


Fig. 3. 48 Potential transients of interrupted dissolution experiments. In each panel, the solid and dashed lines are the potential transients before and after the Al foil was removed from the 1 M NaOH solution, rinsed, dried, and then re-immersed. Arrows represent the potential measured at the time of the interruption. Interruption times are 2 min, 5 min and 10 min.

always much more anodic than the minimum before the interruption. The second minimum was always close to the final potential at the end of the first immersion period (final potential just before interruption is denoted by arrow marks in Fig. 3.47 and 3.48). This suggests that the potential increase in each second immersion period measurement continued from where it left off during the first immersion. If the major contributor to the OCP transient increase after the minimum was the changing solution composition near the surface then the minimum potentials in both cases would have been the same. Figs. 3.47 and 3.48 on the other hand show that the transient increase is due to a permanent change in the metal surface condition during the first dissolution process since the foil tracks the OCP from where it left off even after the interruption.

Another set of interruption experiments were conducted in which the as-annealed 4N aluminum foil was removed from a 1 M NaOH bath (pH 13.50) at various times, rinsed, dried and re-introduced in a 0.1 M Na₂SO₄ solution of pH 11.00. Fig. 3.49 below shows the minimum potentials in the lower pH solution plotted against the interruption times (indicated by hollow circular markers). The open circuit potential transient in the 1 M NaOH solution is shown for comparison. The pH 11.00 minimum potentials show quite similar time dependence with the OCP transient in the pH 13.5 solution but are just shifted in the anodic direction by approximately 0.28 V. There is a minimum at around 0.2- 0.3 min (12-18 s) and also a maximum at around 1 min in both pH solutions. According to the pH dependence of the Nernst potential of the hydride oxidation reaction (Eqn. 3.7), there should be an anodic shift of about 0.18 V from pH 13.5 to pH 11.00. This would account for some part of the potential difference of 0.28 V seen in between the two cases. Thus, in the case of both as-

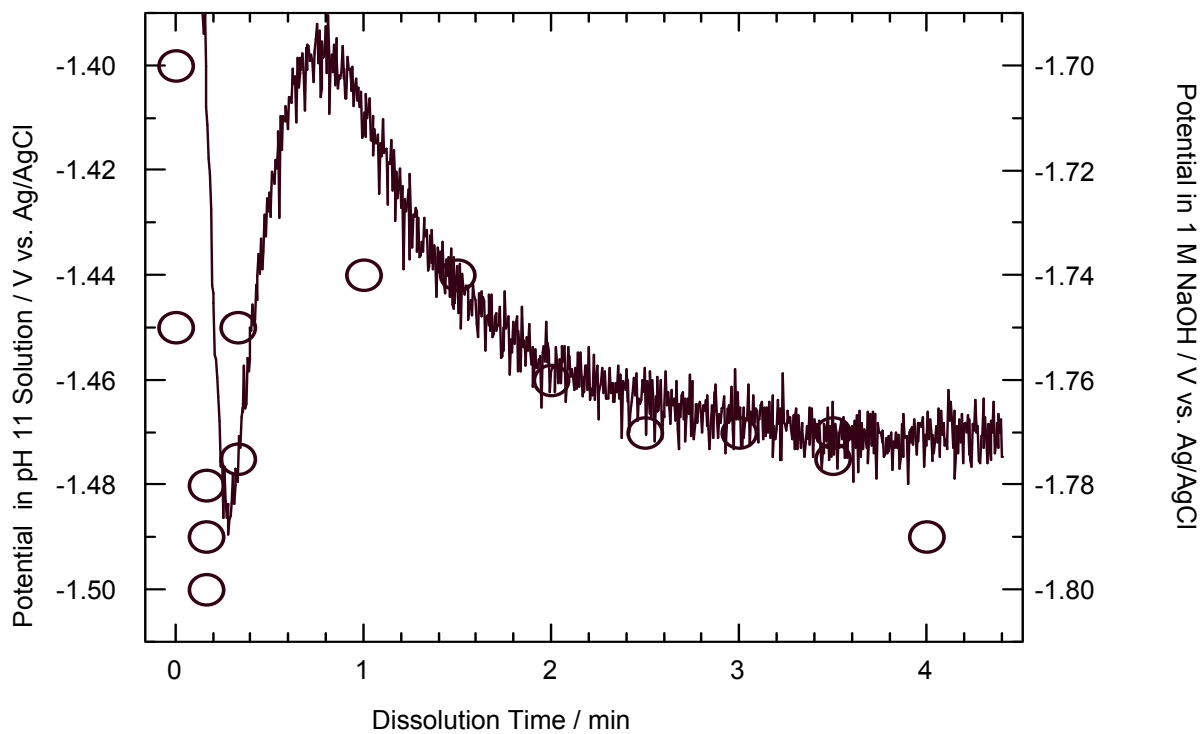


Fig. 3.49 Initial open circuit potentials of as-annealed aluminum foil in 0.1 M Na_2SO_4 solution (pH 11.00), after dissolution in 1 M NaOH solution (pH 13.50) for various times. The open circuit potential in NaOH is shown for comparison. The markers are for pH 11.00 and the curve is for pH 13.50.

annealed (Fig. 3.49) and electropolished (Fig. 3.47 and Fig. 3.48) foils, these interruption experiments indicate that there are changes in the foil surface condition during the dissolution process which affects the time evolution of the corrosion potential of aluminum in the alkaline solution.

3.5.4 Cyclic Voltammetry for interpretation of the corrosion potential transients

The increasing anodic polarization of the open circuit potential transients after the potential minimum could be because of the suppression of anodic dissolution kinetics or enhancement of cathodic kinetics. The enhancement of cathodic kinetics could occur by enrichment of impurities like Cu and Fe as discussed earlier in section 3.5.2. Cyclic voltammetry was used to distinguish between the roles of anodic and cathodic kinetics during the open circuit dissolution of the Al foils. After the 4N electropolished foils were dissolved in 1 M NaOH for various times between 0-10 min, the foil was transferred to a 0.1 M Na₂SO₄ solution of pH 11.75 for the cyclic voltammetry experiments. The lower pH solution was used because in the high pH solution cell ohmic resistance dominated the transients making the interpretation of currents due to electrode kinetics difficult. Also, as discussed in section 3.5.3, the factors leading to the anodic polarization of the OCP transients should survive the transfer of the foil from the high to low pH solution since increase of potentials are due to permanent changes in the metal surface condition. Fig. 3.50 below shows the CV results for foils treated at open-circuit for times of 0, 1, 5 and 10 min in 1 M NaOH before the transfer to the sulfate CV bath. Between the as-electropolished (0 min) and 1 min treated foils, we can see that the anodic peak potential shifts from -1.60 V to -1.55 V. There are very little differences between these two CV transients at potentials close to open-circuit or in the

cathodic range. This shift of the anodic peak indicates that the anodic kinetics are suppressed up to 1 min of dissolution. This time during which anodic kinetics are suppressed agrees with the time when we see a rapid increase in the open circuit potential (up to about 2 min in Fig. 3.45). We can also see a clear increase in the cathodic currents between 1 to 5 min and further between 5 to 10 min. These times when the cathodic kinetics are faster corresponds to the duration when the OCP drifts to more anodic values slowly (After 2 min dissolution time in Fig. 3.45). As suggested earlier, this is possibly because of the surface enrichment of cathodically active impurities like Cu and Fe. Since it would take some time for the impurities to accumulate up to significant levels hence there is some sort of a critical dissolution time before the enhancement of cathodic kinetics. The reasons for the suppression of the anodic kinetics in the initial 2 min of dissolution time is discussed in the next section with the help of Secondary ion mass spectrometry results (SIMS).

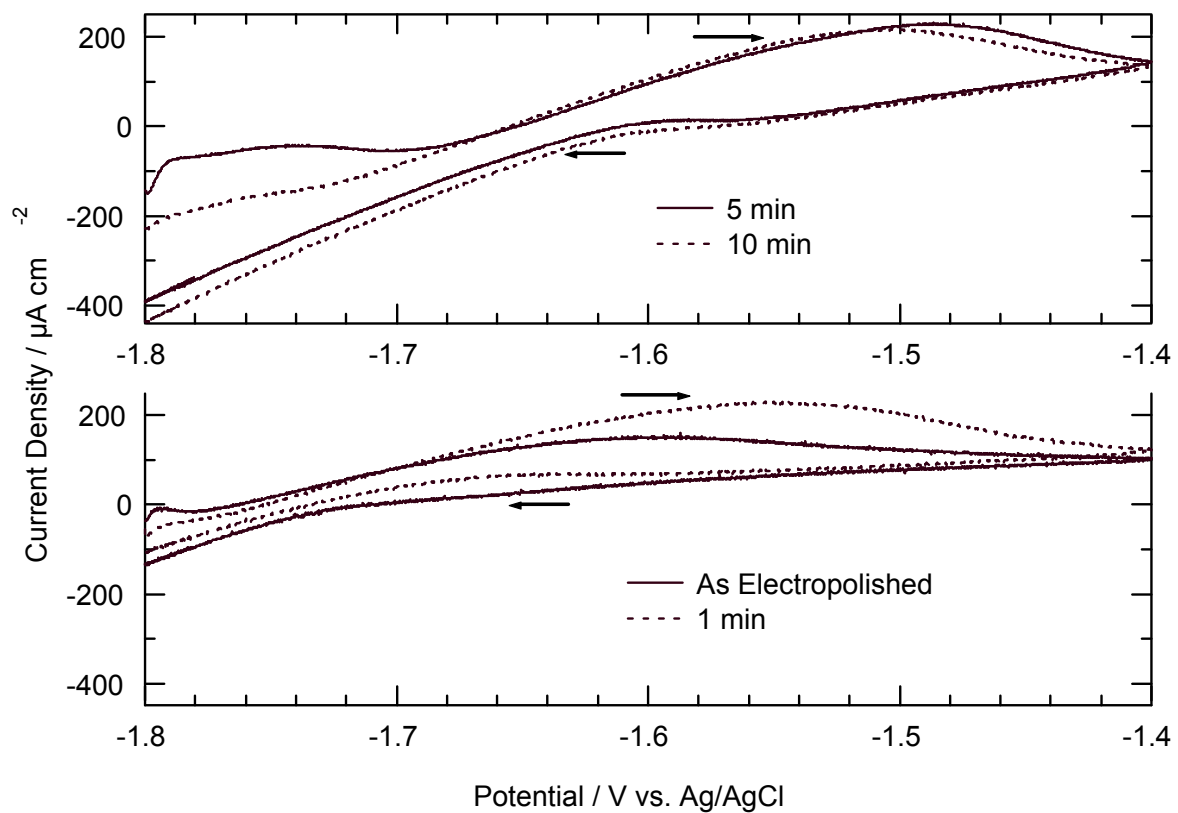


Fig 3.50 Cyclic voltammetry of electropolished foils in 0.1 M Na_2SO_4 solution (pH 11.75), after dissolution in 1 M NaOH solution for various times. The scan rate was 2 mV/s. Scans were initiated at -1.8 V.

3.5.5 SIMS analysis of alkaline treated aluminum at open circuit

As discussed earlier in section 3.4, cyclic voltammetry and potential-step experiments showed that an aluminum hydride layer is in direct contact with the aluminum during the dissolution process with the reaction shown by Eqn. 3.7 being the principal anodic process.^[105] The anodic polarization observed before 2 min dissolution in NaOH could be because of the growth of this hydride layer. In section 3.3 it was shown that AlH_3 was detected during the dissolution process in spite of its high reactivity.^[106] Deuterated baths were used for the SIMS measurements to avoid interference from adsorbed water and hydrogen. The AlD_3 produced during the dissolution process was detected as the AlD^- ion in negative SIMS.

Fig. 3.51 below shows AlD^- profiles for the 4N Al foil dissolved in 1 M NaOD (in D_2O) for 10s, 20s and 1 min. The AlD^- counts were normalized against bulk Al_2^- counts in each sample since this was highest peak in the bulk SIMS spectra. This was necessary for comparison of profiles of samples treated for different times. Absolute concentration of the AlD^- ions were not calculated since the sensitivity factor for AlD^- was not known. As mentioned earlier in section 3.3, the sputtering rate was found to be 0.23 nm/s from measurement of the crater depth in a 4N electropolished foil sputtered for an extended period of time. The depth scale was then estimated from the sputtering times by using the measured sputtering rate. Fig. 3.51 shows that there was significant AlD_3 in the metal up to depths of about 30-50 nm. The amount of AlD_3 is seen to increase with time up to 1 min of dissolution in the NaOD. AFM results have also indicated that there is a nucleation event of AlD_3

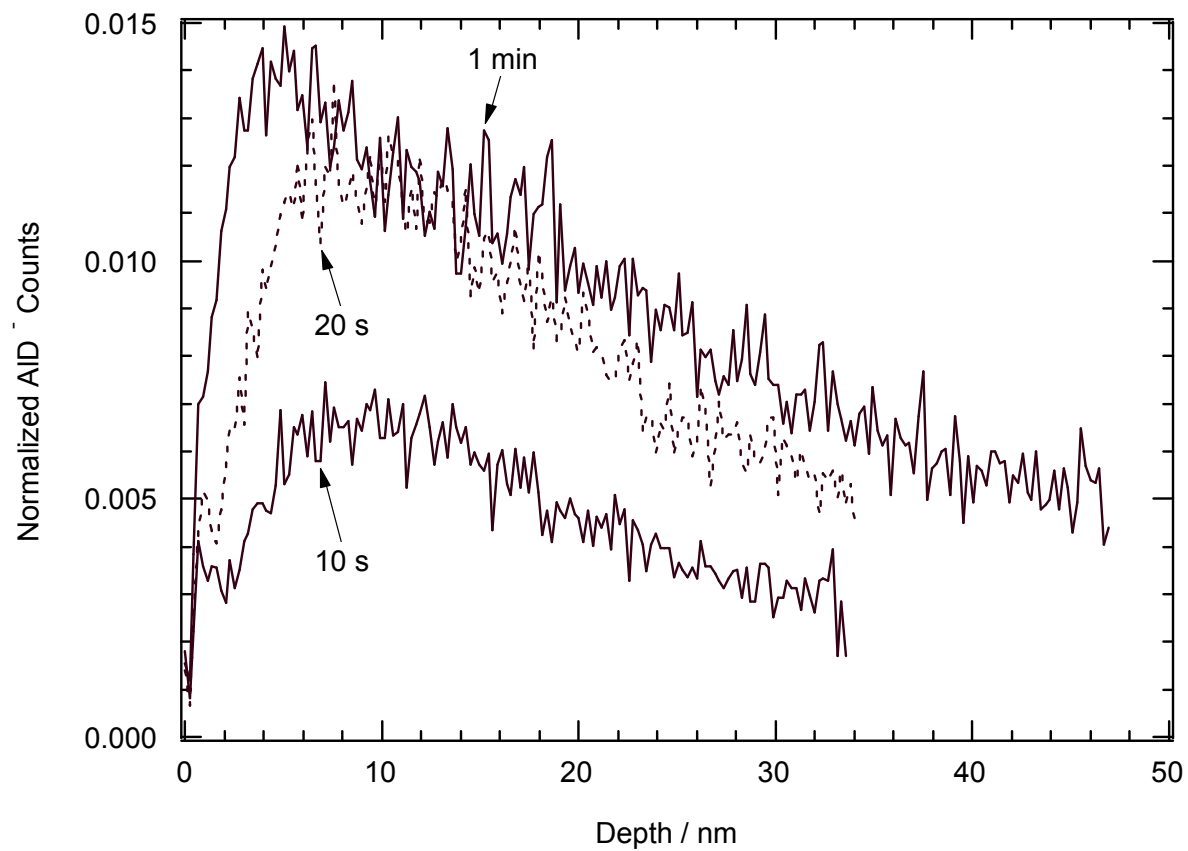
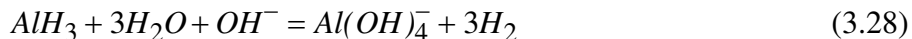


Fig. 3.51 AlD⁻ depth profiles measured by SIMS after dissolution of 4N electropolished aluminum foils for the indicated times in 1 M NaOD (D₂O). Normalization is with respect to the counts of Al₂⁻ in the bulk of the sample.

particles at about 1 min of dissolution time.^[106] These particles were not seen at 10 s or 20 s dissolution times. Thus, the presence of AlD_3 and its increase with time in Fig. 3.51 is indicative of a growing surface AlD_3 film during this time. The AlD_3 seen at 1 min is partly due to the AlD_3 particles nucleating and partly due to the existing film which was accumulating prior to this time. Since the growth of this film occurs parallel to the increasing anodic polarization in the first 2 min, they could be related to each other although the exact nature of this relationship is not known at this point. The growth of this hydride layer is consistent with the effect of $Al(OH)_4^-$ ion concentrations on the open circuit potential transients (Fig. 3.44). The hydride layer is decomposed by water in alkaline solutions to form aluminate ions



Thus, increased $Al(OH)_4^-$ would inhibit the dissolution of AlH_3 and hence increase the growth rate of the hydride layer. If the anodic polarization is associated with the growth of this hydride layer, then the potential would increase more rapidly at higher $Al(OH)_4^-$ concentrations, as seen the OCP transients in Fig. 3.44.

Thus the effect of the solution pH and $Al(OH)_4^-$ ion concentrations on the minimum corrosion potentials are both consistent with the Nernst potential for aluminum hydride oxidation. The anodic polarization after that is due to formation of a surface hydride film in the first 2 min and then due to accumulation of impurity elements like Cu and Fe.

4. CONCLUSIONS

The formation of interfacial voids in aluminum during alkaline dissolution was studied by Doppler broadening positron annihilation spectroscopy (PAS). Simulations of the measurements were conducted to reveal global characteristics of these voids. Direct imaging of voids formed during dissolution was attempted using TEM and STEM. Additional microscopic observations using FE-SEM were reported following removal of controlled depths of metal to expose subsurface voids. Information obtained from the PAS and microscopy results about depths, geometry and number densities of voids in the metal was analyzed with respect to logistics of a void formation mechanism involving vacancy diffusion at room temperature. The following conclusions were drawn from this work:

- (1) The completely non-destructive PAS revealed the presence of a void-containing defect-layer found beneath the oxide-metal interface which was ~ 60 nm thick. The voids were bigger than vacancies and the inner surface of the constituting voids was found to be free of oxide indicating that the voids are formed internally by solid state diffusion of vacancy-type defects and not by dissolution of the metal surface.
- (2) FE-SEM images indicated the presence of 10-20 nm voids after anodic oxidation of the metal up to depths of 5 nm but the void population diminished significantly in samples where 23 or 50 nm of the metal was oxidized. Thus, the voids were present in a metal layer less than 20 nm from the metal-oxide interface.
- (3) TEM and STEM images provided direct evidence of the presence of such voids. The voids were circular in cross-section and around 20 nm in diameter. The number density of the voids was found to be about 10^8 cm^{-2} and it increased by at least ten times as a result of

alkaline treatment. The alkaline dissolution generates a surface topography consisting of ridges surrounding scalloped depressions. Voids were preferentially located near the ridges, an indication that their formation is coupled to the dissolution mechanism.

(4) Vacancy diffusivities estimated from voids size and void layer thickness was $\sim 10^{-14}$ to 10^{-12} cm²/s which is in agreement with the diffusivities of uncomplexed Al vacancies extrapolated to room temperatures reported in literature. While, monovacancy diffusion could account for void growth, it is more difficult to explain vacancy formation at room-temperature because of large vacancy formation energies.

Complexation of vacancies with hydrogen has been proposed to explain the thermodynamic feasibility of vacancy injection at room-temperature since the large vacancy-hydrogen binding energy compensates for the vacancy-formation energy. Formation of these H-vacancy defects could be better understood by characterizing the thermodynamic conditions of hydrogen in aluminum, which motivated the measurement of chemical potential of H in Al during the alkaline dissolution process. Studies on hydrogen interactions with aluminum during alkaline dissolution processes were conducted using the DS cell and Al/Pd bilayer films. The change in the electrochemical potential on hydrogen entry and exit side was monitored and used to calculate the chemical potential of hydrogen in aluminum. The calculated H-chemical potential will be used to quantitatively characterize the thermodynamic conditions of H in aluminum and its implications for H-absorption and H-vacancy defect formation. Permeation studies and diffusivity measurements of H in Al will also be conducted in order to gain information about hydrogen transport behavior in aluminum. The following conclusions were drawn from this work:

(1) Calculated values of hydrogen chemical potential in aluminum gave extremely high fugacities of 10^{17} to 10^{20} atm indicating that very high concentrations of hydrogen is introduced into the metal. The fugacities were even higher than literature values obtained from analytical measurements of H in Al. The measured H chemical potentials were comparatively lower than the equilibrium values (Table 3.1) and may be attributed to a absorption of H as Vac-H defects.

(2) The trend with pH of the calculated equilibrium μ_H values (Table 3.1) and that of the E_{Pd} response time are not the same. Since both E_{Pd} and E_{Al} transients have been shown to be reproducible, there is a considerable complexity involved in the process of hydrogen absorption in the metal.

(3) Diffusivity of H in Al from permeation experiments was found to be $\sim 10^{-9}$ cm²/s for highly alkaline solutions (pH 13.5). The measured diffusivities vary slightly with the pH of the solution making the unusual order of E_{Pd} response time with pH difficult to understand in terms of diffusion alone. Given the high concentrations of hydrogen and vacancies injected by the same alkaline dissolution process, it is possible that the diffusivity is influenced by the rate of injection of vacancies at the Al surface, which could depend on the pH of the solution.

In order to explain the large values of μ_H observed and the formation of room temperature voids requires a better understanding of the surface chemistry of involved processes, especially the presence of hydrogen containing species during alkaline dissolution of aluminum. An extensive study of surface species during the dissolution process was conducted using ToF- SIMS. The focus was on alkaline dissolution times of a few minutes, which results in activation of the metal surface, and formation of large quantities of voids

along with hydrogen absorption. SIMS was supplemented by AFM in order to identify surface features correlating with observed transient changes in the SIMS measurements. The following conclusions were drawn from this work:

(1) The SIMS experiments indicated the presence of large number densities of sub-micrometer size particles formed during open-circuit dissolution of aluminum. These particles nucleated and then dissolved at roughly periodic intervals of ~3 min. These particles were composed of aluminum hydride covered with a hydroxide film as indicated by the SIMS and prior Auger microprobe experiments. This is the first analytical detection of aluminum hydride surface species formed by dissolution.

(2) Alkaline dissolution occurs by continuous anodic oxidation of hydride formed by the accompanying cathodic reaction as indicated by the close proximity of the dissolution potential to the Nernst potential for oxidation of aluminum hydride to hydroxide.

(3) Continuous hydride formation and oxidation indicates near the Nernst potential for the hydride oxidation reaction suggests that the dissolving metal surface is covered by a hydride layer rather than a resistive oxide film as considered previously.

In order to examine whether the electrochemical behavior of anodic alkaline dissolution supports the participation of AlH_3 as a reaction intermediate, identification the potential at the interface of the metal and the surface film was necessary. Cyclic voltammetry and potential step measurements during the anodic dissolution process were used to determine whether the dissolution potential corresponds to the Nernst potential for oxidation of aluminum hydride. A theoretical model based on the proposed mechanism was developed for predicting the experimentally observed CV scans. An abrupt transition of the surface film

properties and dissolution mechanism was demonstrated, in the pH range from 11 to 11.75.

The following conclusions were drawn from this work:

(1) At pH 11, the behavior of the Al electrode is similar to that in neutral pH solutions, controlled by the anodic formation of a surface film with a high ionic conduction resistance. The potential at the metal/film interface indicates that the primary anodic reaction is Al oxidation.

(2) At pH 11.75, the surface film resistance is significantly reduced, and the consequently much larger dissolution current is strongly influenced by mass transport and ohmic resistance. Anodic metal dissolution is mediated by the formation and oxidation of interfacial aluminum hydride. The presence of interfacial AlH_3 during anodic polarization at pH 11.75 suggests that water transport to the metal/film interface is fast enough so that hydride can form before Al^{+3} ions can be transported away from the interface.

The film structure is apparently quite different between the two pH values of 11 and 11.75. The study in the next section was conducted to assess the factors affecting the corrosion potential of aluminum in alkaline solutions like the pH, aluminate ion concentrations, build of surface hydride and enrichment of surface impurities. The effect of the solution phase and metal phase compositions during dissolution were studied using a detailed analysis of the open-circuit potential transients and cyclic voltammetric response. The following conclusions were drawn from this work:

(1) The dependences of the minimum potential of electropolished samples on pH and $\text{Al}(\text{OH})_4^-$ ion concentration were consistent with those expected for the Nernst potential of aluminum hydride oxidation. This finding supports the proposed reaction scheme of alkaline

dissolution, in which surface AlH_3 is formed by reaction of cathodically generated hydrogen with Al metal, and is then anodically oxidized to $\text{Al}(\text{OH})_4^-$ ions.

(2) The minimum potentials of as-annealed foils were displaced in the anodic direction relative to those of electropolished samples, but after about 2 min the transients of both foil types converged. The anodic polarization of as-annealed foils was due to metallic surface layers which contained electrochemically active inhomogeneities, such as segregated metallic impurities.

(3) The increasing corrosion potential with time after the minimum consisted of two stages: a rapid increase up to 2 min, followed by a slower drift continuing for several hours. The second stage was due to the accumulation of surface-enriched Cu and Fe impurities, which anodically polarized the Al by accelerating the cathodic process. This explanation was supported by the increasingly enhanced cathodic kinetics measured by voltammetric scans, and by the separation of potential transients of foils with different bulk Cu concentrations. The abrupt potential increase in the first stage occurred during the accumulation of surface hydride, as measured by SIMS. The surface hydride may have inhibited anodic kinetics, through a mechanism yet to be determined. Interruption experiments indicated that transient solution composition changes did not contribute significantly to the time-dependence of the corrosion potential.

In the alkaline pH range in which AlH_3 mediates dissolution, corrosion is accompanied by the formation of large subsurface metallic voids and rapid absorption of H into the metal as already presented earlier in sections 3.1 and 3.2. The hydride layer in direct contact with the metal could facilitate the formation of associated hydrogen-vacancy defects

during dissolution since the dissolution potential is much more anodic to the Nernst potential for aluminum oxidation, providing the necessary driving force for hydrogen absorption in the metal. These defects in turn could be responsible for the observed high rates of void formation and hydrogen injections. These processes are of potential importance for the fundamental understanding of surface chemical processes leading to hydrogen embrittlement and stress corrosion cracking.

5. REFERENCES

- [1] M. Pourbaix, *Atlas of Electrochemical Equilibria in Aqueous Solutions*, p. 638 pp, Pergamon, New York (1966).
- [2] Y. Tak, N. Sinha and K. R. Hebert, *J. Electrochem. Soc.*, **147** (11), 4103 (2000).
- [3] M. G. Fontana and N. D. Greene, *Corrosion Engineering*, p. 48, McGraw-Hill series, (1978).
- [4] Q. F. Li and N. J. Bjerrum, *J. Power Sources*, **110**, 1 (2002).
- [5] A.R. Despic, D.M. Drazic, M.M. Purenovic, N. Cikovic, *J. Appl. Electrochem.*, **6**, 527 (1976).
- [6] Y. W. Keung, J. H. Nordlien, S. Ono and K. Nisancioglu, *J. Electrochem. Soc.*, **150** (11) B547 (2003).
- [7] C. F. Lin and K. R. Hebert, *J. Electrochem. Soc.*, **137**, 3723 (1990).
- [8] C. K. Dyer and R. S. Alwitt, *J. Electrochem. Soc.*, **128**, 300 (1981).
- [9] A. I. Onuchukwu and S. Trasatti, *Electrochim. Acta*, **33**, 1425 (1988).
- [10] A. I. Onuchukwu, S. P. Trasatti, and S. Trasatti, *Corros. Sci.*, **36**, 1815 (1994).
- [11] H. K. Birnbaum, C. Buckley, F. Zeides, E. Sirois, P. Rozenak, S. Spooner, and J. S. Lin, *J. Alloys Compd.*, **253**, 260 (1997).
- [12] C. E. Buckley and H. K. Birnbaum, *J. Alloys Compd.*, **330**, 649 (2002).
- [13] M. J. Danielson, *Corros. Sci.*, **44**, 829 (2002).
- [14] E. Lunarska and O. Chernyayeva, *Int. J. Hydrogen Energy*, **31**, 285 (2006).
- [15] K. R. Hebert, H. Q. Wu, T. Gessmann, and K. Lynn, *J. Electrochem. Soc.*, **148**, B92 (2001).

- [16] C. E. Buckley, H. K. Birnbaum, J. S. Lin, S. Spooner, D. Bellmann, P. Staron, T. J. Udovic, and E. Hollar, *J. Appl. Crystallogr.*, **34**, 119 (2001).
- [17] K. E. Heusler and W. Allgaier, *Werkst. Korros.*, **22**, 297 (1971).
- [18] R. Greef and C. F. W. Norman, *J. Electrochem. Soc.*, **132**, 2362 (1985).
- [19] O. R. Brown and J. S. Whitley, *Electrochim. Acta*, **32**, 545 (1987).
- [20] D. D. Macdonald, S. Real, S. I. Smedley, and M. Urquidi-Macdonald, *J. Electrochem. Soc.*, **135**, 2410 (1988).
- [21] D. Chu and R. F. Savinell, *Electrochim. Acta*, **36**, 1631 (1991).
- [22] M. L. Doche, J. J. Rameau, R. Durand, and F. Novel-Cattin, *Corros. Sci.*, **41**, 805 (1999).
- [23] S. I. Pyun and S. M. Moon, *J. Solid State Electrochem.*, **4** (2000) 267
- [24] H. B. Shao, J. M. Wang, Z. Zhang, J. Q. Zhang, and C. N. Cao, *J. Electroanal. Chem.*, **549**, 145 (2003).
- [25] G. G. Perrault, *J. Electrochem. Soc.*, **126**, 199 (1979).
- [26] A. R. Despić, D. M. Drazic, J. Balaksina, L. Gajickrstajic, and R. M. Stevanovic, *Electrochim. Acta*, **35**, 1747 (1990).
- [27] J. Radosevic, M. Kliskic, P. Dabic, R. Stevanovic, and A. Despic, *J. Electroanal. Chem.*, **277**, 105 (1990).
- [28] S. Tanaka, M. Aonuma, N. Hirose and T. Tanaki, *J. Electrochem. Soc.*, **149**, D167 (2002).
- [29] S. Tanaka, T. Iwatani, N. Hirose and T. Tanaki, *J. Electrochem. Soc.*, **149**, F186 (2002).
- [30] S. Tanaka, N. Hirose and T. Tanaki, *J. Electrochem. Soc.*, **152**, C789 (2002).

- [31] R. Huang, K. R. Hebert, T. Gessmann and K. G. Lynn, *J. Electrochem. Soc.*, **151**, B227 (2004).
- [32] K. R. Hebert, T. Gessmann, K. G. Lynn, and P. Asoka-Kumar, *J. Electrochem. Soc.*, **151**, B22 (2004).
- [33] K. G. Lynn and R. J. Schultz, *Appl. Phys. A.*, **37**, 31 (1985).
- [34] T. Martin and K.R. Hebert, *J. Electrochem. Soc.*, **148**, B101 (2001).
- [35] R. Huang, K. R. Hebert, and L. S. Chumbley, *J. Electrochem. Soc.*, **151**, B379 (2004).
- [36] J. Langer, *Rev. Mod. Phys.*, **52**, 1 (1980).
- [37] X. Wu and K. R. Hebert, *J. Electrochem. Soc.*, **143**, 83 (1996).
- [38] R. H. Howell, M. Tuomisaari and Y. C. Jean, *Phys. Rev. B* **42**, 6921 (1990).
- [39] K. Muthukrishnan, K. R. Hebert, and T. Makino, *J. Electrochem. Soc.*, **151**, B340 (2004).
- [40] H. K. Birnbaum, C. E. Buckley, F. Zeides, E. Sirois, P. Rozenak, S. Spooner, J. S. Lin, *J. Alloys and Compounds*, **253-254**, 260 (1997).
- [41] C. E. Buckley and H. K. Birnbaum, *Physica B: Condensed Matter (Amsterdam)* **241** (1998).
- [42] C. E. Buckley, H. K. Birnbaum, J. S. Lin, S. Spooner, D. Bellmann, P. Staron, T. J. Udovic and E. Hollar, *J. Appl. Crystallography*, **34**, 119 (2001).
- [43] C. E. Buckley and H. K. Birnbaum, *J. Alloys and Compounds*, **330-332**, 649 (2002).
- [44] H. P. Van Leeuwen, *Corrosion*, **29(5)**, 197 (1973).
- [45] P. Rozenak, *International Journal of Hydrogen Energy*, **32(14)**, 2816 (2007).
- [46] Y. Fukai, *J. Alloys and Compounds*, **356-357**, 263 (2003).

- [47] Y. Fukai, M. Mizutani, S. Yokota, M. Kanazawa, Y. Miura, and T. Watanabe, *J. Alloys and Compounds*, **356-357**, 270 (2003).
- [48] G. Lu and E. Kaxiras, *Phys. Rev. Lett.*, **94**, 155501 (2005).
- [49] M. A. V. Devanathan and Z. Stachurski, *Proc. R. Soc. London, Ser. A*, **270**, 90 (1962).
- [50] R. Driver, *J. Electrochem. Soc.*, **128**, 2367 (1981).
- [51] A. I. Onuchukwu and S. Trasatti, *Electrochim. Acta*, **33**, 1425 (1988).
- [52] M. J. Danielson, *Corrosion Science*, **44**, 829 (2002).
- [53] P. Rozenak, E. Sirois, B. Ladna, H. K. Birnbaum, and S. Spooner, *J. Alloys and Compounds.*, **387**, 201 (2005).
- [54] P. Rozenak, B. Ladna and H. K. Birnbaum, *J. Alloys and Compounds.*, **415**, 134 (2006).
- [55] M. Hara, K. Domen, T. Onishi and H. Nozoye, *Appl. Phys. Lett.*, **59**, 1793 (1991).
- [56] M. Hara, K. Domen, T. Onishi and H. Nozoye, *J. Phys. Chem.*, **95**, 6 (1991).
- [57] M. Hara, K. Domen, T. Onishi, H. Nozoye, C. Nishihara, Y. Kaise and H. Shindo, *Surf. Sci.*, **242**, 459 (1991).
- [58] A. Winkler, C. Resch and K. D. Rendulic, *J. Chem. Phys.*, **95**, 7682 (1991).
- [59] E. L. Crane and R. G. Nuzzo, *J. Phys. Chem. B*, **105**, 3052 (2001).
- [60] E. P. Go, K. Thuermer and J. E. Reutt-Robey, *Surf. Sci.*, **437**, 377 (1999).
- [61] M. Shao, X. Xing and C. Liu, *Electroanalysis*, **6**, 245 (1994).
- [62] A. Seeger, *J. Phys. F Met. Phys.* **3**, 248 (1973).
- [63] J. Burke and T. R. Ramachandran, *Metallurgical and Materials Transactions B*, **3 (1)**, 147 (1972).

- [64] H. Wu, K. R. Hebert, T. Gessmann, and K. G. Lynn, *J. Electrochem. Soc.*, **149**, B108 (2002).
- [65] J. Wiersma, Y. Tak and K. R. Hebert, *J. Electrochem. Soc.*, **138**, 371 (1991).
- [66] P. J. Schultz and K. G. Lynn, *Rev. Mod. Phys.*, **60**, 701 (1988).
- [67] X. Wu, K. R. Hebert, P. Asoka-Kumar, and K. G. Lynn, *J. Electrochem. Soc.*, **141** (1994) 3361.
- [68] P. Hautojarvi and C. Corbel, *Positron Spectroscopy of Solids*, p. 491, IOS Press, Amsterdam (1995).
- [69] J. W. Eddington, *Practical Electron Microscopy in Material Science*, p. 174, Van Nostrand Reinhold, New York (1976).
- [70] E. Lunarska, O. Chernyayeva and L. Spivak, *J. Alloys and Compounds.*, **404**, 269 (2005).
- [71] E. Lunarska and O. Chernyayeva, *Int. J. Hydrogen Energy*, **31**, 237 (2006).
- [72] E. Lunarska and O. Chernyayeva, *Int. J. Hydrogen Energy*, **31**, 285 (2006).
- [73] A. Turnbull, M. S. Maria and N. D. Thomas, *Corrosion Science*, **29**, 89 (1989).
- [74] J. R. Scully, G. A. Young and S. W. Smith, *Acta mater.*, **46 (18)**, 6337 (1998).
- [75] J. D. Fowler, D. Chandra, T. S. Elleman, A. W. Payne and K. Verghese, *J. Am. Ceram. Soc.*, **6**, 155 (1977).
- [76] J. I. Eldridge, R. J. Hussey, D. F. Mitchell and M. J. Graham, *Oxid. Met.*, **30**, 301 (1988).
- [77] B. C. Bunker, G. C. Nelson, K. R. Zavadil, J. C. Barbour, F. D. Wall, J. P. Sullivan, C. F. Windisch, M. H. Engelhardt and D. R. Baer, *J. Phys. Chem. B*, **106**, 4705 (2002).

- [78] J. Graetz and J. J. Reilly, *Journal of Physical Chemistry B*, **109**, 22181 (2005).
- [79] P. J. Herley, W. Jones and G. R. Millward, *Mater. Lett.*, **7**, 441 (1989).
- [80] G. C. Sinke, L. C. Walker, F. L. Oetting and D. R. Stull, *J. Chem. Phys.*, **47**, 2759 (1967).
- [81] A. J. Bard and L. R. Faulkner, *Electrochemical Methods: Fundamentals and Applications*, Wiley, New York (2001).
- [82] W. Feitknecht and P. Schindler, *Pure Appl. Chem.*, **6**, 130 (1963).
- [83] R. S. Alwitt, in *Oxides Oxide Films*, J. W. a. V. Diggle, A. K. Editor, p. 169, New York (1976).
- [84] H. C. Lee, F. Xu, C. S. Jeffcoate and H. S. Isaacs, *Electrochemical and Solid State Letters*, **4**, B31 (2001).
- [85] C. J. Boxley, J. J. Watkins and H. S. White, *Electrochemical and Solid State Letters*, **6**, B38 (2003).
- [86] C. J. Boxley and H. S. White, *J. Electrochem. Soc.*, **151**, B265 (2004).
- [87] C. J. Boxley and H. S. White, *J. Electrochem. Soc.*, **151**, B265 (2004).
- [88] T. Hurlen and A. T. Haug, *Electrochim. Acta*, **29**, 1133 (1984).
- [89] W. Wilhelmsen and T. Hurlen, *Electrochim. Acta*, **32**, 95 (1987).
- [90] J. Newman and K. E. Thomas-Alyea, *Electrochemical Systems*, Wiley, Hoboken, N. J. (2004).
- [90] A. C. Harkness and L. Young, *Can. J. Chem.*, **44**, 2409 (1966).
- [91] T. Valand and K. E. Heusler, *J. Electroanal. Chem.*, **149**, 71 (1983).
- [92] H.Q. Wu, K.R. Hebert, *Electrochim. Acta*, **47**, 1373 (2002).

- [93] K. Arai, T. Suzuki, T. Atsumi, *J. Electrochem. Soc.*, **132**, 1667 (1985).
- [94] Z. Ashitaka, G.E. Thompson, P. Skeldon, G.C. Wood, K. Shimizu, *J. Electrochem. Soc.*, **146**, 1380 (1999).
- [95] Z. Ashitaka, G.E. Thompson, P. Skeldon, G.C. Wood, H. Habazaki, K. Shimizu, *J. Electrochem. Soc.*, **147**, 132 (2000).
- [96] H. Tsubakino, A. Nogami, Y. Yamamoto, A. Yamamoto, M. Terasawa, T. Mitamura, A. Kinomura, Y. Horino, *Appl. Surf. Sci.*, **238**, 464 (2004).
- [97] J. Scherer, O.M. Magnussen, T. Ebel, R.J. Behm, *Corros. Sci.*, **41**, 35 (1999).
- [98] L.F. Mondolfo, *Aluminum Alloys: Structure and Properties*, Butterworths, London, 1976.
- [99] R. Ambat, A.J. Davenport, G.M. Scamans, A. Afseth, *Corros. Sci.*, **48**, 3455 (2006).
- [100] P.M. Aziz, H.P. Godard, *Corrosion*, **10**, 269 (1954).
- [101] A.P. Bond, G.F. Bolling, H.A. Domian, H. Biloni, *J. Electrochem. Soc.*, **113** 773 (1966).
- [102] R.G. Buchheit, *J. Electrochem. Soc.*, **142**, 1994 (1995).
- [103] T. Suter, R.C. Alkire, *J. Electrochem. Soc.*, **148**, B36 (2001).
- [104] P. Leblanc, G.S. Frankel, *J. Electrochem. Soc.*, **149**, B239 (2002).
- [105] S. Adhikari, J. Lee, K.R. Hebert, *J. Electrochem. Soc.*, **155**, C189 (2008).
- [106] S. Adhikari, J. Lee, K.R. Hebert, *J. Electrochem. Soc.*, **155**, C16 (2008).
- [107] F. Brown and W. D. Mackintosh, *J. Electrochem. Soc.*, **120**, 1096 (1973).
- [108] J. W. Diggle, T. C. Downie, and C. W. Goulding, *Chem. Rev. (Washington, D.C.)*, **69**, 365 (1969).

[109] S.M. Myers, P. Norlander, F. Besenbacher and J.K. Nørskov, *Phys. Rev. B*, **33**, 854 (1986).

[110] N.L. Peterson and S.J. Rothman, *Phys. Rev. B*, **1**, 3264 (1970).

[111] T. E. Volin and R. W. Balluffi, *Phys. Status Solidi.*, **25**, 163 (1968).

[112] H. W. Pickering and C. Wagner, *J. Electrochem. Soc.*, **114**, 698 (1967).

[113] R. Ramstetter, G. Lampert, A. Seeger, and W. Schüle, *Phys. Status Solidi.*, **8**, 863 (1965).

[114] R. F. Egerton, F. Wang and P. A. Crozier, *Microscopy and Microanalysis*, **12 (1)**, 65 (2006).

[115] R.F. Egerton, P. Li and M. Malac, *Micron*, **35**, 399 (2004).